UNIVERSITY OF OKLAHOMA

GRADUATE COLLEGE

Natural Anomaly Mediation and its Role in Supersymmetry

A DISSERTATION

SUBMITTED TO THE GRADUATE FACULTY

in partial fulfillment of the requirements for the

Degree of

DOCTOR OF PHILOSOPHY

By

JESSICA BOLICH
Norman, Oklahoma
2026

Downloaded from SHAREOK. Persistent Handle URL: https://hdl.handle.net/11244/342759

Natural Anomaly Mediation and its Role in Supersymmetry

A DISSERTATION APPROVED FOR THE
HOMER L. DODGE DEPARTMENT OF PHYSICS AND
ASTRONOMY

BY THE COMMITTEE CONSISTING OF

Dr. Howard Baer, Chair

Dr. Chung Kao

Dr. Braden Abbot

Dr. Joseph Tischler

Dr. Jessica Ruyle

© Copyright by JESSICA BOLICH 2026
All Rights Reserved.

I dedicate this work to my parents Christopher and Karen Bolich, my brother Tyler Bolich and his partner Sophia Fortner, our dogs Maddie and Teddy, and my friends Diana Spencer, Jessica Cronin, Ben Barnett, and Clara Gatewood. Thank you for standing by me throughout everything.

Acknowledgements

I would like to express my gratitude to my advisor, Howard Baer, for guiding me through the fascinating world of high energy physics and for all that he has taught me during my time conducting research. I would also like to extend my thanks to the physics faculty of the University of Oklahoma and to my fellow graduate students for their help and guidance. Finally, I would like to thank the faculty of Stockton University for introducing me to and teaching me about the wonderfully fascinating world of physics.

Table of Contents

List of Tables viii

List of Figures xi

Abstract xii

1 Motivations and Formulation of Supersymmetry 1
- 1.1 The Standard Model . . . 1
  - 1.1.1 The Higgs Mechanism . . . 1
  - 1.1.2 Problems with the Standard Model . . . 2
- 1.2 Formulation of Supersymmetry . . . 3
  - 1.2.1 Motivation for Supersymmetry . . . 3
  - 1.2.2 The Superfield . . . 4
  - 1.2.3 Supersymmetry Transformations . . . 5
  - 1.2.4 The Left-Chiral Superfield . . . 6
  - 1.2.5 The Kähler Potential and the Superpotential . . . 6
  - 1.2.6 The Curl Superfield . . . 8
  - 1.2.7 Supersymmetry Breaking . . . 9
  - 1.2.8 The MSSM . . . 11
- 1.3 Formulation of Supergravity . . . 13
  - 1.3.1 General Relativity Overview . . . 13
  - 1.3.2 Local Supersymmetry Transformations . . . 14
  - 1.3.3 Supersymmetry Breaking for Supergravity . . . 16
- 1.4 Models of SUSY and SUGRA . . . 17
  - 1.4.1 Constrained MSSM/Minimal Supergravity (CMSSM/mSUGRA) 17
  - 1.4.2 Non-Universal Higgs Model (NUHM) . . . 17
  - 1.4.3 Anomaly Mediated SUSY Breaking (AMSB) . . . 18
  - 1.4.4 Gauge Mediated SUSY Breaking (GMSB) . . . 21
  - 1.4.5 Gaugino Mediated SUSY Breaking (inoMSB) . . . 21
- 1.5 Overview of Research . . . 22

2 Supersymmetry and the Higgs Mass 24
- 2.1 The Higgs Mass and Measures of Naturalness . . . 24
  - 2.1.1 Log-Derivative Measure Δ_{p_i} . . . 26
  - 2.1.2 High Scale Higgs Mass Measure Δ_{HS} . . . 29
  - 2.1.3 Practical Naturalness and the Electroweak Finetuning Measure Δ_{EW} . . . 30
- 2.2 Analysis of the Likelihood of Specific SUSY Models . . . 32
  - 2.2.1 Gauge Mediated SUSY Breaking (GMSB) . . . 33
  - 2.2.2 Gaugino Mediated SUSY Breaking (inoMSB) . . . 33
  - 2.2.3 Gravity Mediated SUSY Breaking . . . 33
- 2.3 Singlet SUSY Breaking Fields . . . 37
- 2.4 Charged SUSY Breaking Fields . . . 39

3 Analysis of Natural Anomaly Mediated Supersymmetry Breaking 44
3.1 Natural anomaly-mediated SUSY breaking (nAMSB) 44
3.2 nAMSB from the Landscape 46
3.3 Sparticle and Higgs masses in $nAMSB$ from the landscape 48
3.4 $AMSB$ benchmark points and model lines 53
3.4.1 $mAMSB$ benchmark 53
3.4.2 $nAMSB0$ benchmark 55
3.4.3 $nAMSB$ benchmark 57
3.4.4 Corresponding AMSB model lines 58
3.4.5 Exploring nAMSB Parameter Space 61
3.4.6 An Alternative $nAMSB$ Model Line 67

4 Detection Channels for Natural Anomaly Mediated SUSY Breaking at the LHC 73
4.1 LHC production cross sections 73
4.2 Sparticle decay modes 77
4.3 LHC excluded regions 80
4.3.1 LHC constraint from gluino pair searches 80
4.3.2 LHC constraint from EWino pair production followed by decay to boosted dijets 81
4.3.3 LHC constraints from SModelS/CheckMATE2 analysis 82
4.3.4 LHC-allowed nAMSB parameter space 84
4.4 nAMSB discovery channels for HL-LHC 85
4.4.1 Same-sign dileptons from wino pair production 87
4.4.2 Hard isolated trileptons from wino pair production 90
4.4.3 Soft OS dileptons from higgsino pair production 93
4.4.4 Top-squark pair production 97

5 Conclusions 99

References 104

List of Tables

3.1 Input parameters and masses in GeV units for the mAMSB, nAMSB0 and nAMSB natural generalized anomaly mediation SUSY benchmark points with $m_t = 173.2$ GeV using Isajet 7.91. 56

4.1 The SM background cross-sections after cut **C2** for the same-sign dilepton $+\not{E}_T$ signal at $\sqrt{s} = 14$ TeV. 89
4.2 Cross section after cuts in ab for the dominant SM backgrounds to the hard 3ℓ signal at LHC14. 93

List of Figures

2.1 Value of m_h vs. $A_t(weak)$ from FeynHiggs for the NUHM2 model with $m_0 = 5$ TeV, $m_{1/2} = 1.2$ TeV, $A_0 = -8$ TeV $\tan\beta = 10$, $\mu = 200$ GeV and $m_A = 2$ TeV. 25

2.2 In *a*), we show the value of m_h vs. A_0 from FeynHiggs and Isasugra for the NUHM2 model with $m_0 = 5$ TeV, $m_{1/2} = 1.2$ TeV, $\tan\beta = 10$, $\mu = 200$ GeV and $m_A = 2$ TeV. Frame *b*) shows the difference in m_h between FeynHiggs and Isasugra. 27

2.3 Plot of *a*) m_h (left vertical axis, blue curve) and Δ_{EW} (right vertical axis, red curve) vs. $m_{1/2}$ in the inoMSB model for $\tan\beta = 10$ and $\mu > 0$. In frame *b*), we plot several sparticle masses vs. $m_{1/2}$. 34

2.4 Parameter space of the singlet sector gravity-mediation model NUHM2 in the m_0 vs. $m_{1/2}$ plane for $A_0 = -1.6m_0$, $\tan\beta = 10$, $\mu = 200$ GeV and $m_A = 2$ TeV. 40

2.5 Parameter space of charged SUSY breaking (CSB) model with *a*) $\tan\beta = 10$ in the m_0 vs. $m_{3/2}$ plane. In *b*), we show CSB parameter space with non-universal bulk terms such that $\mu = 200$ GeV and $m_A = 2$ TeV but still with A_0 as given by its loop-suppressed AMSB value. 43

3.1 Plot of dP/dm_h from an $n = 1$ landscape scan in the nAMSB0 model where $A_0 = 0$. 49

3.2 Plot of *a*) dP/dm_h and *b*) dP/dm_A, from an $n = 1$ landscape scan in the nAMSB model. The red histogram shows the full probability distribution while the blue-dashed histogram shows the remaining distribution after LHC sparticle mass limits are imposed. 51

3.3 Plot of *a*) $dP/dm_{3/2}$, *b*) $dP/dm_0(1,2)$, *c*) $dP/dm_0(3)$ and *d*) $dP/d(A_0/m_0(3))$ from an $n = 1$ landscape scan in the nAMSB model. The red histogram shows the full probability distribution while the blue-dashed histogram shows the remaining distribution after LHC sparticle mass limits are imposed. 52

3.4 Plot of *a*) $dP/dm_{\tilde{g}}$, *b*) $dP/dm_{\tilde{t}_1}$, *c*) $dP/dm_{\tilde{\chi}_2^\pm}$ and *d*) $dP/d(m_{\tilde{\chi}_2^0} - m_{\tilde{\chi}_1^0})$ from an $n = 1$ landscape scan in the nAMSB model. The red histogram shows the full probability distribution while the blue-dashed histogram shows the remaining distribution after LHC sparticle mass limits are imposed. 54

3.5 Plot of Δ_{EW} vs. $m_{3/2}$ along the AMSB model lines. The horizontal dashed line represents $\Delta_{EW} = 30$ and the region below the dashed line is regarded as natural. The vertical dashed line represents the cutoff to the LHC excluded region for $m_{3/2}$. 59

3.6 Plot of m_h vs. $m_{3/2}$ along the AMSB model lines. The light Higgs mass is constrained by LHC measurements to lie between the dashed lines, given some theory error on the calculation of m_h. 60

3.7 Plot of sparticle masses vs. $m_{3/2}$ along the nAMSB model lines. The vertical dashed line represents the upper limit on $m_{3/2}$ imposed by $\Delta_{EW} = 30$ and the horizontal dashed line represents the lower limit of the gluino mass. 62

3.8 Plot of A_0 vs. $m_{3/2}$ parameter space in the nAMSB model for $m_0(3) = 5$ TeV with $m_0(1,2) = 2m_0(3)$ and $\tan\beta = 10$, with $m_A = 2$ TeV and *a*) $\mu = 150$ GeV and *b*) $\mu = 250$ GeV. 64
3.9 Allowed/excluded regions of $m(wino)$ vs. $m(higgsino)$ plane from ATLAS analysis of EWino pair production followed by decay to W, Z, h with decay to boosted dijets. The region below the red contour is excluded by ATLAS searches for boosted, hadronically-decaying winos. 65
3.10 Plot of $m_0(3)$ vs. $m_{3/2}$ parameter space in the nAMSB model for $m_0(1,2) = 2m_0(3)$, $A_0 = 1.2m_0(3)$ and $\tan\beta = 10$, with $m_A = 2$ TeV and *a*) $\mu = 150$ GeV and *b*) $\mu = 250$ GeV. 68
3.11 Plot of m_h vs. $m_{3/2}$ along the nAMSB model-line for $m_{3/2} = 35m_0(3)$ with $m_0(1,2) = 2m_0(3)$, $A_0 = 1.2m_0(3)$ and $\tan\beta = 10$, with $\mu = 250$ GeV and $m_A = 2$ TeV. The horizontal dashed lines show the upper and lower bounds on m_h. The leftmost vertical line represents where sleptons become the LSP, the middle line shows the value for $m_{3/2}$ where $m_{wino} = 600$ GeV and the rightmost vertical line shows the value of $_{3/2}$ where $\Delta_{EW} = 30$. 69
3.12 Plot of Δ_{EW} vs. $m_{3/2}$ along the nAMSB model-line for $m_{3/2} = 35m_0(3)$, $m_0(1,2) = 2m_0(3)$, $A_0 = 1.2m_0(3)$ and $\tan\beta = 10$, with $\mu = 250$ GeV and $m_A = 2$ TeV. The left vertical line represents where sleptons become the LSP and the right line shows the value for $m_{3/2}$ where $m_{wino} = 600$ GeV. The horizontal dashed line represents $\Delta_{EW} = 30$. 70
3.13 Plot of various sparticle masses vs. $m_{3/2}$ along the nAMSB model-line for $m_{3/2} = 35m_0(3)$ with $m_0(1,2) = 2m_0(3)$, $A_0 = 1.2m_0(3)$ and $\tan\beta = 10$, with $\mu = 250$ GeV and $m_A = 2$ TeV. 71

4.1 Plot of $\sigma(pp \to \tilde{g}\tilde{g},\ \tilde{t}_1\tilde{t}_1^*)$ and EWino pair production vs. $m_{3/2}$ along the nAMSB model line. 74
4.2 Plot of various EWino pair production cross sections vs. $m_{3/2}$ along the nAMSB model line: *a*) chargino pair production, *b*) neutralino pair production, *c*) chargino-$\tilde{\chi}_{12}^0$ pair production and *d*) chargino-$\tilde{\chi}_{3,4}^0$ pair production. 76
4.3 Plot of charged and neutral wino branching fractions *a*) BF($\tilde{\chi}_2^+$) and *b*) BF($\tilde{\chi}_3^0$) versus $m_{3/2}$ along the nAMSB model line. 79
4.4 Plot of top squark branching fractions BF($\tilde{t}_1$) versus $m_{3/2}$ along the nAMSB model line. 81
4.5 Variation of $\Delta m_{31} = m_{\tilde{\chi}_3^0} - m_{\tilde{\chi}_1^0}$ vs. $m_{3/2}$. The region left of the black-dashed curve is excluded by LHC13 gluino pair searches and the region to the right of the blue-dashed line is unnatural with $\Delta_{EW} \gtrsim 30$. . . . 84
4.6 Plot of r from `SModelS` and `CheckMate2` vs. $m_{3/2}$ along the nAMSB model line. 85
4.7 Allowed/excluded regions of our nAMSB model-line along with various sparticle masses. The vertical dashed line represents the upper limit on $m_{3/2}$ imposed by $\Delta_{EW} = 30$ and the horizontal dashed line represents the lower limit of the gluino mass. 86
4.8 The production cross section from wino pair production $\widetilde{\chi}_2^{\pm}\widetilde{\chi}_3^0$ along the nAMSB model line with $\mu = 150$ and 250 GeV. 88

4.9 Cross section after cuts for the SSdB signature from wino pair production along the nAMSB model line for *a*) $\mu = 150$ GeV and *b*) $\mu = 250$ GeV. We also show the remaining total background rate. 91
4.10 Cross section after cuts for the hard 3ℓ signature from wino pair production along the nAMSB model line with *a*) $\mu = 150$ GeV and *b*) $\mu = 250$ GeV. We also show the remaining total background rate. The central vertical dotted line corresponds to the LHC-allowed upper limit on p-space. 94
4.11 Cross section after cuts for the soft opposite-sign dilepton plus jet plus $\not{E}_T$ events from higgsino pair production along the nAMSB model line with *a*) $\mu = 150$ GeV and *b*) $\mu = 250$ GeV. We also show the 5σ and 95%CL lines for HL-LHC with 3 ab^{-1} of integrated luminosity. 96
4.12 Cross section after cuts for the soft opposite-sign dilepton plus jet plus $\not{E}_T$ events from higgsino pair production along the nAMSB model line vs. μ but with with $m_{3/2} = 150$ TeV, $m_0(3) = m_{3/2}/35$, $m_0(1,2) = 2m_0(3)$, $A_0 = 1.2m_0(3)$, $m_A = 2$ TeV and $\tan\beta = 10$. In *a*), we show remaining signal cross section after cuts **C3** of Ref. [1] but with $m(\ell\bar{\ell}) < m_{\tilde{\chi}_2^0} - m_{\tilde{\chi}_1^0}$, and in frame *b*), we show the n-σ value after cuts at LHC14 with 3 ab^{-1} of integrated luminosity. 98

Abstract

We discuss here the motivations for supersymmetry, in that it acts as an elegant solution to the big hierarchy problem, provides a mechanism for neutrino masses, and offers up new particles as candidates for dark matter. We review the formulation of supersymmetry and then review different models of supersymmetry breaking. We then use practical naturalness and known experimental data such as the Higgs mass to inform us of the likelihood of each model. We find that models with large A_0 are able to obtain a large enough Higgs mass without large amounts of fine tuning, whereas models with low or no A_0 were unable to do so. In particular, we choose to explore natural anomaly mediated supersymmetry breaking, wherein the loop suppressed anomalies in gravity mediated theories are able to become the dominant contributors to SUSY breaking since the tree level soft terms are suppressed by sequestering. Natural anomaly mediation does not assume universality however, and allows for large A_0 which makes it a more viable candidate than minimal anomaly mediation. Thus, we utilize Isajet, PROSPINO, Madgraph, Pythia8, Delphes, and Root to analyze the SUSY cross sections and determine the most viable discovery channels at the high luminosity LHC.

Chapter 1

Motivations and Formulation of Supersymmetry

1.1 The Standard Model

One of the greatest successes of particle physics has been the completion of the standard model [2], an $SU_C(3) \times SU_L(2) \times U_Y(1)$ gauge theory, with the discovery of the Higgs boson in 2012 [3, 4]. This quantum field theory provides an elegant description of the fundamental particles which are currently known. The model has three sets of gauge bosons: photons γ, which mediate the electromagnetic force, Z and W bosons, which mediate the weak force, and gluons g, which mediate the strong force. The fermions can be summarized as 3 generations of quarks, which form 3 left-handed weak isospin doublets and 6 corresponding right-handed weak isospin singlets, and the leptons, which form 3 left-handed weak isospin doublets of negatively charged leptons paired with a corresponding neutrino and 3 right-handed weak isospin singlets. Right-handed neutrinos are easily added. Finally, there is a scalar Higgs boson which is part of a weak isospin doublet with the Goldstone bosons.

1.1.1 The Higgs Mechanism

Since the weak interaction results in different gauge transformations for the left- and right-handed fermions, their mass terms are not invariant under gauge transformations and therefore are forbidden in the standard model Lagrangian. It is here where the Higgs boson plays a crucial role. It interacts with the fermions

through Yukawa interactions and the Z and W bosons through gauge interactions. Because this boson is scalar, it is able to develop a vacuum expectation value(VEV). By expanding the boson's field about its VEV, the electroweak symmetry of the standard model is spontaneously broken. The presence of this VEV allows for otherwise gauge symmetry breaking mass terms for the quarks and leptons, with the exception of the neutrinos. This also leads to mass terms for the Z and W bosons since the weak symmetry is now spontaneously broken.

1.1.2 Problems with the Standard Model

Despite it tremendous success, the Standard Model has several issues that suggest that physicists do not yet have the complete picture.

- As previously stated, the neutrinos, which are known to have small masses due to neutrino flavor oscillation, do not receive masses from the Higgs mechanism. This results from the fact that only left-handed neutrinos are known to exist [5]. By adding singlet right-handed neutrinos, both Dirac and Majorana mass terms arise, and neutrinos get mass from the see-saw mechanism.

- The standard model does not have a mechanism to incorporate gravity, which is one of the four fundamental interactions in physics.

- Crucially, when renormalizing the Higgs mass, corrections from gauge boson loops, fermion loops, and scalar loops lead to quadratic terms dependent on the SM energy cutoff scale. For example, the four-point Higgs self-interaction

yields the correction

$$\delta m^2_{H_{SM}} = \frac{12g^2 m^2_{H_{SM}}}{32M^2_W}\frac{1}{16\pi^2}\left(\Lambda^2 - m^2_{H_{SM}}\ln\frac{\Lambda^2}{m^2_{H_{SM}}} + \mathcal{O}(\frac{1}{\Lambda^2})\right) \tag{1.1}$$

with similar terms also coming from the gauge boson loops and fermion loops. The quadratic Λ term becomes problematic at higher energies since extremely large cancellations would be required to reach the measured Higgs mass of 125 GeV. These cancellations are unnatural, leading to what is known as the big hierarchy problem.

1.2 Formulation of Supersymmetry

1.2.1 Motivation for Supersymmetry

For the big hierarchy problem, there is an elegant solution: when renormalizing, fermionic loops have an extra negative sign that is not included for bosonic loops. Thus, if there were to be a new symmetry pairing bosons to fermions and vice versa, the quadratic contribution to the Higgs mass would simply cancel out, removing the issue of large corrections at high energies entirely. We call this theory Supersymmetry [6].

In addition to solving the big hierarchy problem, supersymmetry has several other desireable qualities. Local supersymmetric transformations under supersymmetry are able to merge both general relativity and quantum field theory, as well as presenting viable candidates for dark matter [6].

1.2.2 The Superfield

The first challenge one is presented with when formulating such a theory is the manner in which bosons and fermions are paired together. Scalar bosons, gauge bosons, and fermions all transform differently under Lorentz transformations, and must be combined together in such a way that they are treated as equal [6]. In order to do this, one must first introduce the concept of superspace coordinates organized into a Majorana spinor, which we will call θ. A Majorana spinor is a spinor which is equal to its own charge conjugate [6]. Our new spinor θ is not an operator, but instead is made of anticommuting numbers θ_1, θ_2, θ_3, and θ_4 which obey the Grassman algebra relation

$$\{\theta_a, \theta_b\} = 0. \tag{1.2}$$

This new spinor represents coordinates in superspace, and along with the space-time four-vector x^μ, are the coordinates of the new superfields, $\hat{\Phi}(x, \theta)$. Most importantly, θ allows us to combine together the different particle fields equally. The superfield is expanded in terms of θ, with the coefficients of the expansion being normal fields which are functions of x. Thus, the most general expansion of the superfield is

$$\begin{aligned}\hat{\Phi}(x,\theta) = \mathcal{S} - i\sqrt{2}\overline{\theta}\gamma_5\psi - \frac{i}{2}(\overline{\theta}\gamma_5\theta)\mathcal{M} + \frac{1}{2}(\overline{\theta}\theta)\mathcal{N} + \frac{1}{2}(\overline{\theta}\gamma_5\gamma_\mu\theta)V^\mu \\ + i(\overline{\theta}\gamma_5\theta)[\overline{\theta}(\lambda + \frac{i}{\sqrt{2}}\not{\partial}\psi)] - \frac{1}{4}(\overline{\theta}\gamma_5\theta)^2[\mathcal{D} - \frac{1}{2}\Box\mathcal{S}]\end{aligned} \tag{1.3}$$

where $\mathcal{S}$, $\mathcal{M}$, $\mathcal{N}$, and $\mathcal{D}$ are scalar fields, ψ and λ are Majorana spinor fields, and V^μ is a vector field [6].

1.2.3 Supersymmetry Transformations

While we now have a superfield combining both bosonic and fermionic fields together, it is also crucial that we formulate symmetry relations between them. In particular, it is necessary for bosonic fields to transform to fermionic fields and vice versa [6]. Fortunately, such symmetry transformations can be derived. They are as follows:

$$\begin{aligned}
\delta\mathcal{S} &= i\sqrt{2}\overline{\alpha}\gamma_5\psi \\
\delta\psi &= -\frac{\alpha\mathcal{M}}{\sqrt{2}} - i\frac{\gamma_5\alpha\mathcal{N}}{\sqrt{2}} - i\frac{\gamma_\mu\alpha V^\mu}{\sqrt{2}} - \frac{\gamma_5\not{\partial}\mathcal{S}\alpha}{\sqrt{2}} \\
\delta\mathcal{M} &= \overline{\alpha}\left(\lambda + i\sqrt{2}\not{\partial}\psi\right) \\
\delta\mathcal{N} &= i\overline{\alpha}\gamma_5\left(\lambda + i\sqrt{2}\not{\partial}\psi\right) \\
\delta V^\mu &= -i\alpha\gamma^\mu\lambda + \sqrt{2}\overline{\alpha}\partial^\mu\psi \\
\delta\lambda &= -i\gamma_5\alpha\mathcal{D} - \frac{1}{2}[\not{\partial}, \gamma_\mu]V^\mu\alpha \\
\delta\mathcal{D} &= \overline{\alpha}\not{\partial}\gamma_5\lambda
\end{aligned} \tag{1.4}$$

where α is the supersymmetry transformation parameter organized into a Majorana spinor, and γ_μ and γ_5 are the Dirac matrices [6].

1.2.4 The Left-Chiral Superfield

Our current definition for the superfield is a general one; in practice, not all of the component fields need be present [6]. With careful choices of field definitions, the superfield can be reduced. Let $V^\mu = \partial\zeta$ and $\delta\lambda = 0$, thus implying that $\mathcal{D} = 0$ as well from the SUSY transformations in 1.4. To satisfy this, we can choose λ to be 0, which gives us the fields

$$\frac{(\partial^\mu \mathcal{S} - iV^\mu)}{\sqrt{2}}, \psi_L, \frac{\mathcal{M} - i\mathcal{N}}{\sqrt{2}} \tag{1.5}$$

where $\psi_L = \frac{1-\gamma_5}{\sqrt{2}}\psi$ and is a left-handed spinor field. Setting $\psi_R = \frac{1+\gamma_5}{\sqrt{2}}\psi = 0$, $\zeta = \mathcal{S}$, and $\mathcal{N} = i\mathcal{M} \equiv i\mathcal{F}$, the superfield reduces to

$$\begin{aligned}\hat{\mathcal{S}}_L = \mathcal{S} + i\sqrt{2}\overline{\theta}\psi_L + i\overline{\theta}\theta_L\mathcal{F} + \frac{i}{2}(\overline{\theta}\gamma_5\gamma_\mu\theta)\partial^\mu\mathcal{S} \\ - \frac{1}{\sqrt{2}}\overline{\theta}\gamma_5\theta\cdot\overline{\theta}\not{\partial}\psi_L + \frac{1}{8}(\overline{\theta}\gamma_5\theta)^2\Box\mathcal{S}.\end{aligned} \tag{1.6}$$

Our newly defined superfield $\hat{\mathcal{S}}_L$ is called the left-chiral superfield. $\mathcal{S}$ is the complex scalar field, ψ_L is the left handed spinor field, and $\mathcal{F}$ is an auxiliary field which can be rewritten in terms of the other fields using their equations of motion [6]. The Hermitian conjugate of $\hat{S}_L$ has the structure of a right-chiral superfield, which is a different irreducible SUSY representation [6].

1.2.5 The Kähler Potential and the Superpotential

The next step is to find an action which is invariant under SUSY transformations and therefore a Lagrangian which describes the interactions, kinetic terms, and

mass terms of all the particles in the theory. Beginning with a theory containing just left-chiral superfields, two functions can be constructed: the Kähler potential and the superpotential. We define the minimal Kähler potential as

$$K(\hat{\mathcal{S}}^\dagger, \hat{\mathcal{S}}) = \sum_{i=1}^{N} \hat{\mathcal{S}}^{i\dagger} \hat{\mathcal{S}}_i \tag{1.7}$$

where the superfields have been normalized, the basis is diagonalized, and there are N chiral superfields [6]. From the Kähler potential, we take the coefficient of the $(\overline{\theta}\gamma_5\theta)^2$, called the D-term. This yields

$$\mathcal{L}_D = \sum_{i=1}^{N} \partial_\mu \mathcal{S}^{i\dagger} \partial^\mu \mathcal{S}_i + \frac{i}{2} \overline{\psi}^i \not{\partial} \psi_i + \mathcal{F}^{i\dagger} \mathcal{F}_i. \tag{1.8}$$

This is the D-term Lagrangian [6].

From renormalizability, the superpotential is dictated to be at most a cubic of $\hat{\mathcal{S}}$. This can be expanded in a power series as

$$\begin{aligned} \hat{f}(\hat{\mathcal{S}}) = \hat{f}(\hat{\mathcal{S}} = \mathcal{S}) &+ \sum_i \left. \frac{\partial \hat{f}}{\partial \hat{\mathcal{S}}_i} \right|_{\hat{\mathcal{S}}=\mathcal{S}} (\hat{\mathcal{S}} - \mathcal{S})_i \\ &+ \frac{1}{2} \sum_{i,j} \left. \frac{\partial^2 \hat{f}}{\partial \hat{\mathcal{S}}_i \partial \hat{\mathcal{S}}_j} \right|_{\hat{\mathcal{S}}=\mathcal{S}} (\hat{\mathcal{S}} - \mathcal{S})_i (\hat{\mathcal{S}} - \mathcal{S})_j \\ &+ \frac{1}{3!} \sum_{i,j,k} \left. \frac{\partial^3 \hat{f}}{\partial \hat{\mathcal{S}}_i \partial \hat{\mathcal{S}}_j \partial \hat{\mathcal{S}}_k} \right|_{\hat{\mathcal{S}}=\mathcal{S}} (\hat{\mathcal{S}} - \mathcal{S})_i (\hat{\mathcal{S}} - \mathcal{S})_j (\hat{\mathcal{S}} - \mathcal{S})_k + ... \end{aligned} \tag{1.9}$$

From this, we extract the coefficient of the $\theta\theta_L$ term, yielding the Lagrangian

$$\begin{aligned}\mathcal{L}_F = &-i\sum_i \left.\frac{\partial \hat{f}}{\partial \hat{\mathcal{S}}_i}\right|_{\hat{\mathcal{S}}=\mathcal{S}} \mathcal{F}_i - \frac{1}{2}\sum_{i,j} \left.\frac{\partial^2 \hat{f}}{\partial \hat{\mathcal{S}}_i \partial \hat{\mathcal{S}}_j}\right|_{\hat{\mathcal{S}}=\mathcal{S}} \overline{\psi}_i P_L \psi_j \\ &+ i\sum_i \left.\left(\frac{\partial \hat{f}}{\partial \hat{\mathcal{S}}_i}\right)^\dagger\right|_{\hat{\mathcal{S}}=\mathcal{S}} \mathcal{F}_i^\dagger - \frac{1}{2}\sum_{i,j} \left.\left(\frac{\partial^2 \hat{f}}{\partial \hat{\mathcal{S}}_i \partial \hat{\mathcal{S}}_j}\right)^\dagger\right|_{\hat{\mathcal{S}}=\mathcal{S}} \overline{\psi}_i P_R \psi_j.\end{aligned} \tag{1.10}$$

The total Lagrangian for this theory is $\mathcal{L} = \mathcal{L}_D + \mathcal{L}_F$ [6].

1.2.6 The Curl Superfield

Next, we must construct a superfield and Lagrangian which accounts for gauge fields and their interactions. Since we will need the gauge field V^μ to be present, the left-chiral superfield representation no longer works. Instead, V_A^μ, where A is a gauge index, is paired up with a corresponding Majorana spinor λ_A, which represents the fermion superpartner of V_A^μ. Additionally, as with the left-chiral superfield, an auxiliary field $\mathcal{D}_A$ is paired with the fields. These three fields are used to create the curl superfield,

$$\hat{W}_A(\hat{x},\theta) = \lambda_{LA}(\hat{x}) + \frac{1}{2}\gamma^\mu\gamma^\nu F_{\mu\nu A}(\hat{x})\theta_L - i\overline{\theta}\theta_L(\not{\partial}\lambda_R)_A - i\mathcal{D}_A(\hat{x})\theta_L, \tag{1.11}$$

where, as before, λ_{LA} and θ_L are the left-handed projections of λ_A and θ, $\not{\partial}_{AC} = \not{\partial}\delta_{AC} + ig(t_B^{\text{adj.}})_{AC}\not{V}_B$, $\hat{x}_\mu = x_\mu + \frac{i}{2}\overline{\theta}\gamma_5\gamma_\mu\theta$, and

$$F_{\mu\nu A} = \partial_\mu V_{\nu A} - \partial_\nu V_{\mu A} - gF^{ABC}V_{\mu B}V_{\nu C}, \tag{1.12}$$

which is the gauge field tensor [6].

The curl superfield ultimately leads to two additional Lagrangian terms which are combined with $\mathcal{L}_D$ and $\mathcal{L}_F$. First, the gauge kinetic term,

$$\mathcal{L}_{GK} = \frac{i}{2}\overline{\lambda}_A \not{D}_{AC}\lambda_C - \frac{1}{4}F_{\mu\nu A}F_A^{\mu\nu} + \frac{1}{2}\mathcal{D}_A\mathcal{D}_A, \tag{1.13}$$

as well as the gauge interaction term

$$\begin{aligned}\mathcal{L}_{\text{Gauge}} &= i(\partial_\mu \mathcal{S})^\dagger g(t\cdot V^\mu)\mathcal{S} - i\mathcal{S}^\dagger g(t\cdot V^\mu)\partial_\mu\mathcal{S} - \mathcal{S}^\dagger[gt\cdot D - g^2(t\cdot V)^2]\mathcal{S} \\ &+ \frac{1}{2}[-g\overline{\psi}(t\cdot \not{V})\psi_L + g\overline{\psi}(t^*\cdot \not{V})\psi_R] \\ &- \left(\sqrt{2}g\mathcal{S}^\dagger t_A \overline{\lambda}_A \frac{1-\gamma_5}{2}\psi + \text{h.c.}\right)\end{aligned} \tag{1.14}$$

where $D_\mu\mathcal{S} = \partial_\mu\mathcal{S} + igt\cdot V_\mu\mathcal{S}$ is the covariant derivative [6].

1.2.7 Supersymmetry Breaking

There is another critical part of supersymmetry: it is not an exact symmetry. If it were, the particles and their superpartners would have the same mass. Since a boson with an identical mass to the electron has not been discovered, we know then that supersymmetry must be broken.

Recall electroweak symmetry breaking-this is possible because the scalar Higgs field obtains a VEV, which when expanding the Higgs field around this, leads to terms that would otherwise be forbidden by the electroweak symmetry. We can extend this spontaneous symmetry breaking to supersymmetry as well. There are two types: F-type and D-type. These each occur when one of the $\mathcal{F}$ or

$\mathcal{D}$ auxiliary fields gains a VEV; that is $\langle 0|\mathcal{F}_i|0\rangle \neq 0$ or $\langle 0|\mathcal{D}_A|0\rangle \neq 0$ [6]. The conditions for each are as follows: for F-type, that there is no solution to

$$\left(\frac{\partial \hat{f}}{\partial \mathcal{S}}\right)_{\hat{\mathcal{S}}=\mathcal{S}} = 0, \tag{1.15}$$

and for D-type, that there is no solution to

$$g\sum_i \mathcal{S}^{i\dagger} t_A \mathcal{S}_i + \xi_A = 0, \tag{1.16}$$

where ξ_A is a dimensionful coupling for the Fayet-Iliopoulos term, which only applies to $U(1)$ gauge couplings. Therefore, it stands that the scalar potential for supersymmetry theories can be written as

$$V = \frac{1}{2}\sum_A \mathcal{D}_A\mathcal{D}_A + \sum_i |\mathcal{F}_i|^2. \tag{1.17}$$

Despite the many new scalar fields that would couple to the fermions in the standard model, it is far more typical for supersymmetry breaking to occur in a separate sector from the standard model and its superpartners [6]. New, unknown superfields are located in this *hidden sector*, and these are the fields that are responsible for the supersymmetry breaking. The effects of this are felt in the known sector through mediator particles which interact with both the standard model and its superpartners as well as the fields in the hidden sector. Unfortunately, we do not know the exact nature of supersymmetry breaking, so in practice, all supersymmetry breaking terms that remain invariant under unbroken

symmetries at the supersymmetry breaking scale and which do not reintroduce the quadratic divergences which supersymmetry was formulated to remove, are added into the Lagrangian [6]. These terms are what are known as soft SUSY breaking terms. They can be classified into one of four types:

- terms linear in $\mathcal{S}_i$ which are only relevant for singlets of all symmetries,
- scalar masses,
- bilinear terms of the form $\mathcal{S}_i\mathcal{S}_j$ or trilinear terms of the form $\mathcal{S}_i\mathcal{S}_j\mathcal{S}_k$,
- and gaugino masses.

Taking these into consideration, a generalized soft SUSY breaking Lagrangian [6] can be written as

$$\begin{aligned}\mathcal{L}_{\text{soft}} = &\sum_i C_i\mathcal{S}_i + \sum_{i,j} B_{ij}\mathcal{S}_i\mathcal{S}_j + \sum_{i,j,k} A_{ijk}\mathcal{S}_i\mathcal{S}_j\mathcal{S}_k + \text{h.c.} \\ &- \sum_{i,j} \mathcal{S}^{i\dagger} m_{ij}^2 \mathcal{S}_j - \frac{1}{2}\sum_{A\alpha} M_{A\alpha}\overline{\lambda}_{A\alpha}\lambda_{A\alpha} - \frac{i}{2}\sum_{A\alpha} M'_{A\alpha}\overline{\lambda}_{A\alpha}\gamma_5\lambda_{A\alpha}.\end{aligned} \tag{1.18}$$

1.2.8 The MSSM

The Minimal Supersymmetric Model, or MSSM, is a SUSY theory which is derived directly from the Standard Model. First, the gauge bosons are embedded in the corresponding curl superfields, one for each gauge group

$$\hat{B} \ni (\lambda_0, B_\mu, \mathcal{D}_B),$$

$$\hat{W}_A \ni (\lambda_A, W_{A\mu}, \mathcal{D}_{WA}), A = 1, 2, 3, \text{and}$$

$$\hat{g}_A \ni (\tilde{g}_A, G_{A\mu}, \mathcal{D}_{gA}), A = 1, ..., 8.$$

Next, we have the fermions and their corresponding sfermions and auxiliary fields, given by the chiral superfields

$$\hat{L}_i \equiv \begin{pmatrix} \hat{\nu}_i \\ \\ \hat{e}_i \end{pmatrix},$$
$$\hat{Q}_i \equiv \begin{pmatrix} \hat{u}_i \\ \\ \hat{d}_i \end{pmatrix}$$

for the left handed isospin doublets, and $\hat{E}_i^C$, $\hat{U}_i^C$, and $\hat{D}_i^C$ for the right handed isospin singlets [6]. Each left-chiral superfield is then expanded into its corresponding component fields. Finally, in the MSSM there are two Higgs superfields instead of just one. This is necessary to cancel anomalies introduced by the new field content. The fields

$$\hat{H}_u = \begin{pmatrix} \hat{h}_u^+ \\ \\ \hat{h}_u^0 \end{pmatrix},$$
$$\hat{H}_d = \begin{pmatrix} \hat{h}_d^- \\ \\ \hat{h}_d^0 \end{pmatrix}$$

are the two Higgs superfields. The up-type superfield $\hat{H}_u$ can only give mass to particles with isospin $T_3 = +1/2$ while the down-type superfield $\hat{H}_d$ grants mass to particles with $T_3 = -1/2$. SUSY is broken by adding explicit mass terms for the scalars and gauginos and bilinear and trilinear terms that are allowed by the gauge symmetries. [6]

Without simplification, the MSSM has up to 178 parameters that define it. This includes masses, gauge couplings, and soft SUSY breaking parameters [6]. This can be simplified by requiring that the parameters be within the range of the weak scale, as well as setting the first two generations of quark and lepton masses equal to zero and setting any CP or flavor violating terms equal to zero. [6]

1.3 Formulation of Supergravity

One may note that SUSY has been formulated without accounting for the gravitational interaction. We will expand upon SUSY to craft a theory that does address it.

1.3.1 General Relativity Overview

As with any theory that utilizes gravity, general relativity is necessary. The basis of general relativity is that one can change between different reference frames by way of general coordinate transformations (GCT's), defined as

$$x^\mu \to x'^\mu = \frac{\partial x'^\mu}{\partial x^\nu}. \tag{1.19}$$

Tensors transform under GCT's by multiplying a factor of $\frac{\partial x'^\mu}{\partial x^\nu}$ for every contravariant index and a factor of $\frac{\partial x^\nu}{\partial x'^\mu}$ for every covariant index [6]. Spinors are transformed by first shifting to a flat tangent space with coordinates ξ^a by the transformation $x^\mu = e^\mu_a \xi^a$ where $e^\mu_a = \frac{\partial x^\mu}{\partial \xi^a}$ and $g_{\mu\nu} = e^a_\mu e^b_\nu \eta_{ab}$ where $g_{\mu\nu}$ is the metric of the curved space, η_{ab} is the Minkowski metric, and e^μ_a is the vierbein.

Finally, in order to account for the general coordinate transformations in the Lagrangian, the covariant derivatives are defined as

$$D_\nu V^\mu \equiv \partial_\nu V^\mu + \Gamma^\mu_{\rho\nu} V^\rho, \tag{1.20}$$

$$D_\nu V_\mu \equiv \partial_\nu V_\mu + \Gamma^\rho_{\nu\mu} V_\rho, \tag{1.21}$$

and

$$D_\mu \psi \equiv \partial_\mu \psi - \frac{i}{4}\omega^{rs}_\mu \sigma_{rs}\psi \tag{1.22}$$

where the Γ's are connection fields defined by $g_{\mu\nu}$ and ω is a spin connection field defined by e^μ_a [6].

1.3.2 Local Supersymmetry Transformations

As we have seen so far, supersymmetry transformations have been global ones. However, if we require the transformation parameter α to be position dependent, the kinetic terms of the Lagrangian will no longer be invariant under SUSY transformations due to picking up additional terms [6]. To amend this, we introduce the Rarita-Schwinger field ψ_μ which transforms as $\psi_\mu \to \psi_\mu + \frac{1}{\kappa}\partial_\mu \alpha$ and is spin-$\frac{3}{2}$. Additionally, we introduce the spin-2 field $g_{\mu\nu}$ which transforms as $g_{\mu\nu} \to g_{\mu\nu} - i\kappa\overline{\alpha}(\gamma_\nu\psi_\mu + \gamma_\mu\psi_\nu)$ as the superpartner to ψ_μ. These new fields are called the gravitino and graviton, where the graviton is now the mediator particle for the gravitational field and the gravitino is its fermion superpartner [6]. Thus, this new theory is known as supergravity. The presence of these new

fields in the SUGRA Lagrangian leads to non-renormalizable terms. This is merely an indication that SUGRA is not a complete theory, but rather an effective field theory hinting at one more complex [6]. Allowing for the presence of these nonrenormalizable terms allows one to generalize the Kähler potential and the superpotential. We may also combine them into a singe function

$$G(\hat{\mathcal{S}}^\dagger, \hat{\mathcal{S}}) = K(\hat{\mathcal{S}}^\dagger, \hat{\mathcal{S}}) + \log|\hat{f}(\hat{\mathcal{S}})|^2, \tag{1.23}$$

known as the Kähler function. As the SUGRA Lagrangian is extensive, it will not be replicated here, but may be referenced in chapter 10 of Baer and Tata [6]. While we do permit non-renormalizable terms, they must still be invariant under the following local SUSY transformations [6]:

$$\begin{aligned}
\delta\mathcal{S}_i &= -i\sqrt{2}\overline{\alpha}\psi_{iL} \\
\delta\psi_{iL} &= \sqrt{2}\not{D}\mathcal{S}_i\alpha_R + i\sqrt{2}e^{G/2}(G^{-1})^j_i G_j\alpha_L - \frac{i}{2\sqrt{2}}\alpha_L\overline{\lambda}_A\lambda_{B,R}(G^{-1})^j_i\frac{\partial f^*_{AB}}{\partial\mathcal{S}^{*j}} + ... \\
\delta e^a_\mu &= -i\overline{\alpha}\gamma^a\psi_\mu \\
\delta\psi_\mu &= 2D_\mu\alpha + ie^{G/2}\gamma_\mu\alpha + ... \\
\delta V^\mu_A &= -i\overline{\alpha}\gamma^\mu\lambda_A \\
\delta\lambda_{AR} &= \frac{i}{2}\sigma^{\mu\nu}F_{A\mu\nu}\alpha_R - ig\mathrm{Re}(f^{-1}_{AB})G^i(t_B)_{ij}\mathcal{S}_j\alpha_R + ...
\end{aligned} \tag{1.24}$$

The terms of the Lagrangian must also be covariant under general coordinate transformations [6].

1.3.3 Supersymmetry Breaking for Supergravity

Spontaneous supersymmetry breaking for supergravity adheres to the same mechanisms seen in supersymmetry; however, as the supergravity Lagrangian can be rewritten to omit the auxiliary fields, the F and D type SUSY breaking conditions become

$$\langle 0|e^{G/2}(G^{-1})^{j}_{i}G_{j}|0\rangle \neq 0 \tag{1.25}$$

and

$$\langle 0|\mathrm{Re}(f_{AB})^{-1}G^{i}t_{Bij}\mathcal{S}_{j}|0\rangle \neq 0 \tag{1.26}$$

respectively [6].

In order to proceed with calculating the SUSY breaking terms, one may follow the subsequent process: Begin by separating the scalar fields in the theory into observable sector fields C_i and hidden sector fields h_i. The hidden sector fields will be able to develop the large VEVs which are greater than the weak scale and necessary to produce the needed masses. These VEVs will lead to F-type SUSY breaking [7], which allows the gravitino to develop a mass through the superHiggs effect. This is similar to how the Z and W bosons gain their masses in electroweak symmetry breaking in that the gravitino absorbs a goldstino fermion produced by the SUGRA breaking [6, 7].

1.4 Models of SUSY and SUGRA

Supersymmetry and supergravity are general theories of which many specific theories can fall under due to the varying ways in which SUSY may be broken. For clarity, we will review several relevant models here.

1.4.1 Constrained MSSM/Minimal Supergravity (CMSSM/mSUGRA)

Minimal supergravity is the simplest model to consider. It adopts the universality principle, where the scalar bosons and gauginos share the masses m_0 and $m_{1/2}$ respectively, the trilinear coefficients become A_0, the gauge couplings are unified at $g_{\rm GUT}$, and off-diagonal A and m terms are zero. Universality takes place close to the Planck scale in this model, though the gauginos may share a mass at the GUT scale from the unification of the gauge couplings [6]. With universality, the parameter space of mSUGRA is

$$m_0,\ m_{1/2},\ A_0,\ \tan\beta,\ \text{sign}(\mu). \quad (mSUGRA) \tag{1.27}$$

This simplified parameter space makes it a convenient theory to study.

1.4.2 Non-Universal Higgs Model (NUHM)

Though mSUGRA adopts universality, this assumption is not necessarily physical. The sfermions may have universal masses in families since SO(10) Grand Unification theories combine the families of matter superfields into single 16 component spinors [6, 8]. This guarantees the universal masses for the sfermions if the

SUSY breaking masses are above the SO(10) breaking scale [8]. Since the Higgs bosons are not a part of the superfield multiplet in SO(10) theories, universality of the scalar bosons including the Higgs bosons is not supported by the symmetry. Non-universal Higgs mass models allow for the Higgs fields to have masses varying from m_0. NUHM adds masses for the two Higgs bosons, m_{H_u} and m_{H_d} which, along with sign(μ) are convenient to exchange with the CP odd Higgs mass m_A and the value of μ. Additionally, the scalar mass m_0 may be split into different masses for each generation $m_0(i)$. This leaves us with the total parameter space

$$m_0(i),\ m_{1/2},\ A_0,\ \tan\beta,\ m_A,\ \mu. \quad (NUHMi) \tag{1.28}$$

1.4.3 Anomaly Mediated SUSY Breaking (AMSB)

AMSB can be formulated in two different ways. The first, AMSB0, allows matter and Higgs scalars to gain large masses, but gauginos gain loop-suppressed masses proportional to the gauge group beta functions[9]. Unlike the extra-dimensional sequestering mechanism of Ref. [10], the $4-d$ DSB-inspired version of AMSB has no problem with tachyonic slepton masses and no need for ad-hoc bulk contributions to soft breaking terms since large scalar masses are expected to be generically present.

Alternatively, in the Randall-Sundrum AMSB model[10] ($AMSB$), it was posited that SUSY breaking arose in a hidden sector sequestered from the visible sector in extra-dimensional spacetime. In such a set-up, the leading contribution to *all* soft SUSY breaking terms was from the superconformal anomaly, and

suppressed by a loop factor from the gravitino mass $m_{3/2}$. In this form of AMSB, a common value of scalar masses was expected thus avoiding the SUSY flavor problem which seems endemic to models of gravity-mediation. Also, since $m_{soft} \ll m_{3/2}$, the cosmological gravitino problem could be avoided since in the early universe thermally-produced gravitinos could decay before the onset of BBN[11]. In both cases of $AMSB$ and $AMSB0$, the thermally underproduced wino-like WIMPs could have their relic abundance non-thermally enhanced by either gravitino[12] or moduli-field decays[13, 14, 15].

At the one loop level, the gaugino masses for AMSB [6] are

$$\begin{aligned} M_1 &= \frac{33}{5}\frac{g_1^2}{16\pi^2}m_{3/2}, \\ M_2 &= \frac{g_2^2}{16\pi^2}m_{3/2}, \text{ and} \\ M_3 &= -3\frac{g_3^2}{16\pi^2}m_{3/2}, \end{aligned} \tag{1.29}$$

the scalar masses [6] are

$$
\begin{aligned}
m_{U_3}^2 &= \left(-\frac{88}{25}g_1^4 + 8g_3^4 + 2f_t\hat{\beta}_{f_t}\right)\frac{m_{3/2}^2}{(16\pi^2)^2} + m_0^2, \\
m_{D_3}^2 &= \left(-\frac{22}{25}g_1^4 + 8g_3^4 + 2f_b\hat{\beta}_{f_b}\right)\frac{m_{3/2}^2}{(16\pi^2)^2} + m_0^2, \\
m_{Q_3}^2 &= \left(-\frac{11}{50}g_1^4 - \frac{3}{2}g_2^4 + 8g_3^4 + f_t\hat{\beta}_{f_t} + f_b\hat{\beta}_{f_b}\right)\frac{m_{3/2}^2}{(16\pi^2)^2} + m_0^2, \\
m_{L_3}^2 &= \left(-\frac{99}{50}g_1^4 - \frac{3}{2}g_2^4 + f_\tau\hat{\beta}_{f_\tau}\right)\frac{m_{3/2}^2}{(16\pi^2)^2} + m_0^2, \\
m_{E_3}^2 &= \left(-\frac{198}{25}g_1^4 + 2f_\tau\hat{\beta}_{f_\tau}\right)\frac{m_{3/2}^2}{(16\pi^2)^2} + m_0^2, \\
m_{H_u}^2 &= \left(-\frac{99}{50}g_1^4 - \frac{3}{2}g_2^4 + 3f_t\hat{\beta}_{f_t}\right)\frac{m_{3/2}^2}{(16\pi^2)^2} + m_0^2, \\
m_{H_d}^2 &= \left(-\frac{99}{50}g_1^4 - \frac{3}{2}g_2^4 + 3f_b\hat{\beta}_{f_b} + f_\tau\hat{\beta}_{f_\tau}\right)\frac{m_{3/2}^2}{(16\pi^2)^2} + m_0^2,
\end{aligned}
\tag{1.30}
$$

and the A-parameters [6] are given by

$$
\begin{aligned}
A_t &= \frac{\hat{\beta}_{f_t}}{f_t}\frac{m_{3/2}}{16\pi^2}, \\
A_b &= \frac{\hat{\beta}_{f_b}}{f_b}\frac{m_{3/2}}{16\pi^2}, \text{ and} \\
A_\tau &= \frac{\hat{\beta}_{f_\tau}}{f_\tau}\frac{m_{3/2}}{16\pi^2},
\end{aligned}
\tag{1.31}
$$

where $m_{3/2}$ is the mass of the gravitino. The $\hat{\beta}_{f_i}$ [6] are defined as

$$
\begin{aligned}
\hat{\beta}_{f_t} &= f_t\left(-\frac{13}{15}g_1^2 - 3g_2^2 - \frac{16}{3}g_3^2 + 6f_t^2 + f_b^2\right), \\
\hat{\beta}_{f_b} &= f_b\left(-\frac{7}{15}g_1^2 - 3g_2^2 - \frac{16}{3}g_3^2 + f_t^2 + 6f_b^2 + f_\tau^2\right), \\
\hat{\beta}_{f_\tau} &= f_\tau\left(-\frac{9}{5}g_1^2 - 3g_2^2 + 3f_b^2 + 4f_\tau^2\right).
\end{aligned}
\tag{1.32}
$$

For minimal AMSB, the parameter space is given by

$$m_0,\ m_{3/2},\ \tan\beta,\ \text{sign}(\mu) \quad (mAMSB) \tag{1.33}$$

where $m_{3/2}$ is the gravitino mass [6].

1.4.4 Gauge Mediated SUSY Breaking (GMSB)

In models characterized as GMSB, SUSY is broken in a hidden sector that communicates with the visible sector via a messenger sector at energy scale Λ [16]. Scalars gain squared masses at 2-loops $m_i^2 \sim \left(\frac{\alpha_i}{4\pi}\Lambda\right)^2$ whilst gauginos gain mass at 1-loop at $m_\lambda \sim c\lambda\frac{\alpha_i}{4\pi}\Lambda$, so they are comparable. Trilinear soft terms are further loop suppressed so that one takes $A_i \simeq 0$ at the messenger scale $Q = \Lambda$. The parameter space of the minimal GMSB is

$$\Lambda,\ M,\ n_5,\ \tan\beta,\ \text{sign}(\mu),\ C_{grav} \quad (GMSB) \tag{1.34}$$

where n_5 is a given number of messenger fields, M is the mass scale associated with the messenger fields, $\Lambda = \frac{\langle F_S\rangle}{\langle\mathcal{S}\rangle}$ where $\mathcal{S}$ and F_S are the scalar and auxiliary components of a gauge singlet field $\hat{\mathcal{S}}$, and $C_{grav} \equiv \frac{\langle F_S\rangle}{\lambda\langle F_S\rangle}$ where λ is the messenger sector Yukawa coupling [6].

1.4.5 Gaugino Mediated SUSY Breaking (inoMSB)

In the inoMSB setup [17, 18, 19], matter superfields live on one brane whilst SUSY breaking fields live on a different brane separated from the first in an

extra-dimensional geometry. Gravity and gauge fields live in the bulk. Since gauge superfields interact directly with the SUSY breaking sector, they gain weak scale masses $m_{1/2}$ at the compactification scale M_c whilst scalar masses and A_i terms are ~ 0. The matter scalars gain mass from RG evolution from $Q = M_c$ to $Q = m_{weak}$. The parameter space for inoMSB is

$$m_{1/2},\ M_c,\ \tan\beta,\ \mathrm{sign}(\mu) \quad (inoMSB) \tag{1.35}$$

where M_c is the compactification scale [6].

1.5 Overview of Research

SUSY models offer promising solutions to a number of known problems in modern day physics; however, they must be tested experimentally in order to confirm or reject their validity. The goal of the subsequent research is to firstly demonstrate how older models that were once favored are now likely to be ruled out due to constraints originating from the mass of the Higgs boson, as well as to explore newer models that can take their place. We will then specifically explore a specific model, natural anomaly mediated SUSY breaking, in both the string landscape and in parameter space in order to deduce the regions in parameter space that are allowed by experimental constraints. After making this determination, we will simulate particle collisions and detections for analysis to determine what the strongest signals are at the upcoming high luminosity LHC and the recently completed Run 3 that can be used to confirm whether or not the nAMSB model

is viable.

Chapter 2

Supersymmetry and the Higgs Mass

2.1 The Higgs Mass and Measures of Naturalness

One of the many challenges of SUSY narrowing down the exact model and method of SUSY breaking. As of LHC Run 2, no distinctly SUSY signals have been discovered. Despite this, we did obtain data useful in constraining the possible SUSY models. We find such a useful piece of information in the Higgs mass, measured at $m_h \simeq 125$ GeV. In SUSY theories, the light Higgs mass with one-loop corrections is given by

$$m_h^2 = m_Z^2 \cos^2 2\beta + \frac{3g^2 m_t^4}{8\pi^2 m_W^2}\left(\log(\frac{m_{SUSY}^2}{m_t^2}) + \frac{x_t^2}{m_{SUSY}^2}\left(1 - \frac{x_t^2}{12m_{SUSY}^2}\right)\right) \quad (2.1)$$

where $m_{SUSY}^2 \simeq m_{\tilde{t}_1} m_{\tilde{t}_2}$ optimizes the scale choice and $x_t = A_t - \mu \cot\beta$.

Given the paramount importance of m_h in this work, we use Isajet 7.91 to evaluate sparticle mass spectra[20, 21], but interface with FeynHiggs[22] for the most up-to-date derived values of m_h. The value of m_h is plotted in Fig. 2.1 vs. $A_t(weak)$ for a natural SUSY benchmark point in the NUHM2 model[23] with $m_0 = 5$ TeV, $m_{1/2} = 1.2$ TeV, $A_0 = -8$ TeV, $\tan\beta = 10$, $\mu = 200$ GeV and $m_A = 2$ TeV. The results are plotted versus $A_t(weak)$. From Fig. 2.1, we see that m_h is minimized around $A_t \simeq 0$ (minimal mixing scenario) where $m_h \sim 116$ GeV, well below its measured value. As $|A_t|$ increases in either direction, we see m_h reaching ~ 125 GeV for $A_t \sim m_0 \sim 5$ TeV, *i.e.* substantial weak-scale trilinear terms are

needed. For somewhat larger values of $|A_t|$, the value of m_h drops precipitously before the model enters the "no EWSB" region, where large values of A_0 cause top-squark soft terms to run tachyonic leading to charge-and-color-breaking (CCB) minima in the scalar potential.

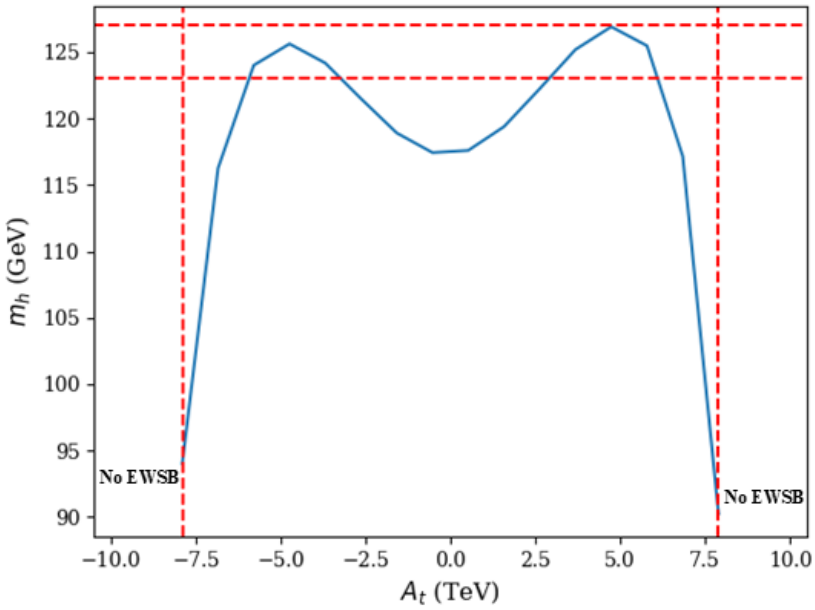


Figure 2.1: Value of m_h vs. $A_t(weak)$ from FeynHiggs for the NUHM2 model with $m_0 = 5$ TeV, $m_{1/2} = 1.2$ TeV, $A_0 = -8$ TeV $\tan\beta = 10$, $\mu = 200$ GeV and $m_A = 2$ TeV.

For reference, in Fig. 2.2*a*) we plot the value of m_h for the same NUHM2 benchmark point as in Fig. 2.1, but this time vs. A_0 using both Isajet and FeynHiggs. The value of m_h^2 in Isajet is computed using the RG-improved one-loop effective potential keeping just third generation fermion/sfermion contributions[24], but where the Yukawa couplings are evaluated including weak scale threshold corrections[25] which provide the leading two-loop effects[26]. Frame *b*) shows the difference between Isajet and FeynHiggs which in this case at least is always within

± 2 GeV. From frame *a*), we see the value of m_h maximizing for large *negative* A_0 values with $A_0 \sim -1.6 m_0$. Using all GUT scale parameters, the spectra hits the region of tachyonic stop masses for large positive A_0 before m_h reaches its maximal mixing value.

Because m_h^2 is maximized when $x_t = \pm\sqrt{6} m_{SUSY}$ in the maximal mixing scenario [26], rather large weak scale trilinear soft terms are required. Furthermore, though SUSY models were crafted to solve the Big Hierarchy Problem, a Little Hierarchy Problem (LHP) may arise as a result of the LHC data limits on sparticle masses indicating that the soft SUSY breaking scale m_{soft} be much greater than the weak scale m_{weak}. While it is known that $m_{weak} \sim 0.1$ TeV, the recent constraints from the LHC indicate that $m_{soft} \sim 1 - 10$ TeV. Depending on how models resolve the LHP, they may have evidence of finetuning and be considered *unnatural* as a result. This leads us to the idea of *naturalness* as a measure of how probable a SUSY model is to occur without heavy amounts of finetuning required to achieve observed values of data. Disagreement arises, however, when determining how exactly to quantify naturalness.

2.1.1 Log-Derivative Measure Δ_{p_i}

First we consider the log-derivative naturalness measure

$$\Delta_{p_i} \equiv max_i \left| \frac{\partial \log m_Z^2}{\partial \log p_i} \right| = max_i \left| \frac{p_i}{m_Z^2} \frac{\partial m_Z^2}{\partial p_i} \right| \tag{2.2}$$

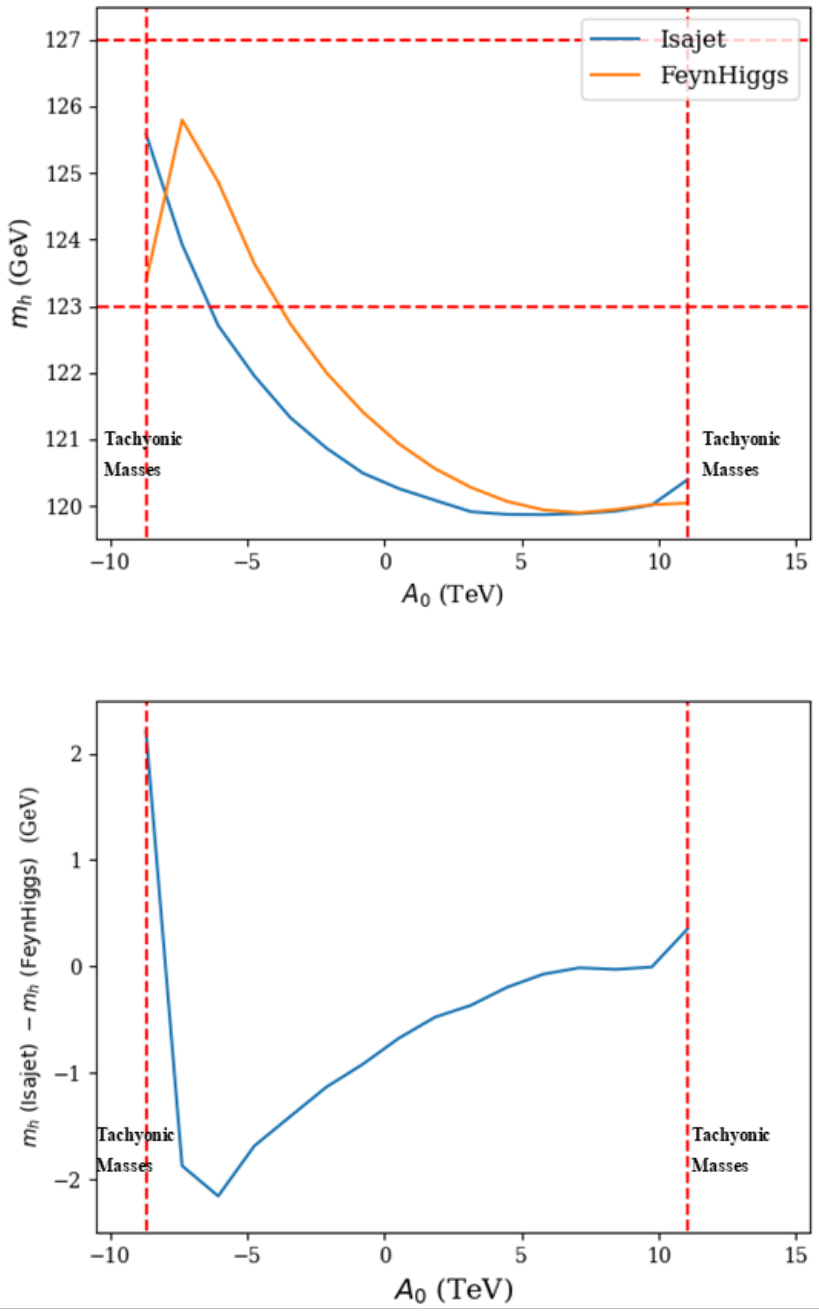


Figure 2.2: In *a*), we show the value of m_h vs. A_0 from FeynHiggs and Isasugra for the NUHM2 model with $m_0 = 5$ TeV, $m_{1/2} = 1.2$ TeV, $\tan\beta = 10$, $\mu = 200$ GeV and $m_A = 2$ TeV. Frame *b*) shows the difference in m_h between FeynHiggs and Isasugra.

where the p_i are the $i = 1 - N$ fundamental parameters of the theory in question [33]. Papers that used this measure typically started with

$$m_z^2/2 = \frac{m_{H_u}^2 - m_{H_d}^2 \tan^2\beta}{\tan^2\beta - 1} - \mu^2 \tag{2.3}$$

where $m_{H_{u,d}}^2$ are the weak scale Higgs soft terms, μ is the (SUSY conserving) superpotential Higgs mass term, and $\tan\beta \equiv v_u/v_d$ is the ratio of Higgs field vevs. For $\tan\beta = 10$, evaluating the weak scale parameters at the GUT scale [36] yields

$$\begin{aligned}
-2\mu^2(m_{SUSY}) &= -2.18\mu^2 \\
-2m_{H_u}^2(m_{SUSY}) &= 3.84M_3^2 + 0.32M_3M_2 + 0.047M_1M_3 - 0.42M_2^2 \\
&\quad + 0.011M_2M_1 - 0.012M_1^2 - 0.65M_2A_t - 0.15M_2A_t \\
&\quad - 0.025M_1A_t + 0.22A_t^2 + 0.004M_3A_b \\
&\quad - 1.27m_{H_u}^2 - 0.053m_{H_d}^2 \\
&\quad + 0.73m_{Q_3}^2 + 0.57m_{U_3}^2 + 0.049m_{D_3}^2 - 0.052m_{L_3}^2 + 0.053m_{E_3}^2 \\
&\quad + 051.m_{Q_2}^2 - 0.11m_{U_2}^2 + 0.051m_{D_2}^2 - 0.052m_{L_2}^2 + 0.053m_{E_2}^2 \\
&\quad + 051.m_{Q_1}^2 - 0.11m_{U_1}^2 + 0.051m_{D_1}^2 - 0.052m_{L_1}^2 + 0.053m_{E_1}^2 .
\end{aligned} \tag{2.4}$$

The requirement for a model to be considered natural would be a value of $\Delta_{p_i} \lesssim 30$ [34, 35].

However, a criticism of Δ_{p_i} is that it is unclear what the p_i should be [36]. The soft parameters in many SUSY theories only parametrize the ignorance of the

origin of the soft terms. As a result, it is unknown what correlations may lie between the parameters that are consequently ignored. This can potentially lead to overestimation of the finetuning by factors of up to 10^3 compared to other measures of finetuning [28, 138].

2.1.2 High Scale Higgs Mass Measure Δ_{HS}

Another measure of finetuning comes from expanding

$$m_h^2 \simeq \mu^2 + m_{H_u}^2(m_{weak}) \sim \mu^2 + m_{H_u}^2(m_{GUT}) + \delta m_{H_u}^2 \tag{2.5}$$

and then defining

$$\Delta_{HS} \equiv \delta m_{H_u}^2 / m_h^2. \tag{2.6}$$

It is common to estimate $\delta m_{H_u}^2$ in terms of high scale parameters, but using a single step integration of the RGE:

$$\frac{dm_{H_u}^2}{dt} = \frac{2}{16\pi^2}\left(-\frac{3}{5}g_1^2 M_1^2 - 3g_2^2 M_2^2 + \frac{3}{10}g_1^2 S + 3f_t^2 X_t\right) \tag{2.7}$$

where $t = \log(Q^2)$, Q is the renormalization scale, $X_t = m_{Q_3}^2 + m_{U_3}^2 + m_{H_u}^2 + A_t^2$ and $S = m_{H_u}^2 - m_{H_d}^2 + Tr[\mathbf{m}_Q^2 - \mathbf{m}_L^2 - 2\mathbf{m}_U^2 + \mathbf{m}_D^2 + \mathbf{m}_E^2]$. Setting the gauge couplings, $m_{H_u}^2$, and S to zero, we can integrate to obtain an expression for $\delta m_{H_u}^2$. For the MSSM, we get

$$\delta m_{H_u}^2|_{rad} \sim -\frac{3f_t^2}{8\pi^2}(m_{Q_3}^2 + m_{U_3}^2 + A_t^2 \ln(\Lambda^2/M_{SUSY}^2) \tag{2.8}$$

where the cutoff Λ may be as large as the reduced Planck mass $m_P \simeq 2.4 \times 10^{18}$ GeV [36].

This measure is also not without issue, as $\delta m_{H_u}^2$ is not independent of $m_{H_u}^2(m_{GUT})$, which means the tuning does not occur between independent parameters [36]. Furthermore, requiring a small $\delta m_{H_U}^2$ often leads to $m_{H_U}^2$ not running to small or negative values which leads to an absence of EW symmetry breaking. Finally, this measure can also overestimate the amount of finetuning by factors up to 10^3 as well [138].

2.1.3 Practical Naturalness and the Electroweak Finetuning Measure Δ_{EW}

The prior measures of finetuning fail in that they are not independent of the SUSY model, leading to overestimation of the finetuning of a given model. We now turn to the idea of *practical naturalness*:

> An observable is *practically natural* when all *independent* contributions to the observable are comparable to or less than the observable in question.

This is model independent, allowing for better comparison of finetuning between models, and furthermore reduces the overall magnitude of finetuning.

The previously mentioned LHP can lead to violation of practical naturalness [27, 28]. The weak scale may be related to the weak scale soft SUSY breaking

terms by the following equation:

$$m_Z^2/2 = \frac{m_{H_d}^2 + \Sigma_d^d - (m_{H_u}^2 + \Sigma_u^u)\tan^2\beta}{\tan^2\beta - 1} - \mu^2 \simeq -m_{H_u}^2 - \mu^2 - \Sigma_u^u(\tilde{t}_{1,2}). \quad (2.9)$$

Here, m_{H_u} and m_{H_d} are soft breaking SUSY Higgs mass terms, μ is the SUSY-conserving Higgs/higgsino mass scale and the $\Sigma_{u,d}^{u,d}$ contain an assortment of loop corrections that go as $\Sigma_{u,d}^{u,d} \sim \lambda^2 m_{sparticle}^2/16\pi^2$ where λ is some associated gauge or Yukawa coupling. The $\tan\beta \equiv v_u/v_d$ is the usual ratio of Higgs field vacuum expectation values (vevs). Practical naturalness can then be quantified by the electroweak finetuning measure defined as [29]

$$\Delta_{EW} \equiv max_i|maximal\ term\ on\ RHS\ of\ Eq.\ 2.9|/(m_Z^2/2). \quad (2.10)$$

A value of $\Delta_{EW} < 30$ is typically required for a given model to be considered natural. This requires that all terms of the right-hand-side of Eq. 2.9 to lie within a factor of 4 of m_Z. Δ_{EW} is the most conservative of the finetuning measures and is non-optional.

Low values of Δ_{EW} require that $m_{H_u}^2$ runs barely negative (so it has a natural value $\sim -m_Z^2$ at the weak scale) and that μ, which feeds mass to W, Z, h and higgsinos, is also comparable to m_Z. Thus, a prediction is that higgsinos are light, $\sim 100 - 350$ GeV, and likely to result in a higgsino-like lightest SUSY particle (LSP) in SUSY models. For spectra with small $\mu \sim 100 - 350$ GeV, the $\Sigma_u^u(\tilde{t}_{1,2})$ are frequently the largest contributions to the weak scale since their Yukawa

couplings are large:

$$\Sigma_u^u(\tilde{t}_{1,2}) = \frac{3}{16\pi^2} F(m_{\tilde{t}_{1,2}}) \times \left[f_t^2 - g_Z^2 \mp \frac{f_t^2 A_t^2 - 8 g_Z^2 (\frac{1}{4} - \frac{2}{3} x_W) \Delta_t}{m_{\tilde{t}_2}^2 - m_{\tilde{t}_1}^2} \right] \qquad (2.11)$$

where $\Delta_t = (m_{\tilde{t}_L}^2 - m_{\tilde{t}_R}^2)/2 + m_Z^2 \cos 2\beta (\frac{1}{4} - \frac{2}{3} x_W)$, $g_Z^2 = (g^2 + g'^2)/8$, $x_W \equiv \sin^2 \theta_W$ and $F(m^2) = m^2(\log(m^2/Q^2) - 1)$ with $Q^2 \simeq m_{\tilde{t}_1} m_{\tilde{t}_2}$. Hence, top squarks cannot be too heavy.

The presence of light higgsinos leads to some very different detection strategies for SUSY at LHC compared to earlier predictions with a bino- or wino-like LSP[30]. Dark matter is expected to occur as a mixture of (mainly) SUSY-DFSZ-axion along with a depleted abundance of higgsino-like WIMPs[31, 32, 137].

2.2 Analysis of the Likelihood of Specific SUSY Models

Having established the importance of naturalness for SUSY models, we now turn to study specific models and compare the consequences of the Higgs mass $m_h = 125$ GeV. Requiring this mass leads to a number of consequences; we shall discuss models falling into the following two categories:

- within the MSSM, one can lift $m_h \to 125$ GeV in SUSY models with small trilinear soft terms $A_t \sim 0$ by requiring top-squarks in the $10 - 100$ TeV regime or
- again within the MSSM, one can have TeV-scale top-squarks but with large A-terms[37].

First we will consider models with small A_t before moving onto discussion of models with large A_t.

2.2.1 Gauge Mediated SUSY Breaking (GMSB)

In GMSB, the small A_i terms then require that stop masses lie in the tens of TeV range in order to generate $m_h \sim 123 - 127$ GeV. With such large stop masses, the $\Sigma_u^u(\tilde{t}_{1,2})$ contributions to the weak scale become of order $\sim 10^3 - 10^5$ and consequently the minimal GMSB model is highly finetuned under Δ_{EW} (see Fig. 6 of Ref. [38, 137]).

2.2.2 Gaugino Mediated SUSY Breaking (inoMSB)

To gain $m_h \simeq 125$ GeV [3, 39] in inoMSB, enormous values of $m_{1/2}$ are required which drives Δ_{EW} to very large values: see Fig. 2.3 where we use Isasugra for the inoMSB spectra and FeynHiggs for the corresponding value of m_h. As is expected, in inoMSB with $m_0 = 0$, the lightest stau is LSP, so either R-parity violation or other LSPs (axinos, gravitinos, $\cdots$) would have to be invoked to avoid cosmological constraints on stable charged relics [137].

2.2.3 Gravity Mediated SUSY Breaking

In gravity-mediated SUSY breaking models, one assumes a hidden sector which serves as an arena for SUSY breaking, and a visible sector containing (at least) the usual MSSM fields. All are contained in the supergravity (SUGRA) Lagrangian, which is assumed to be the low energy effective field theory (EFT) of string

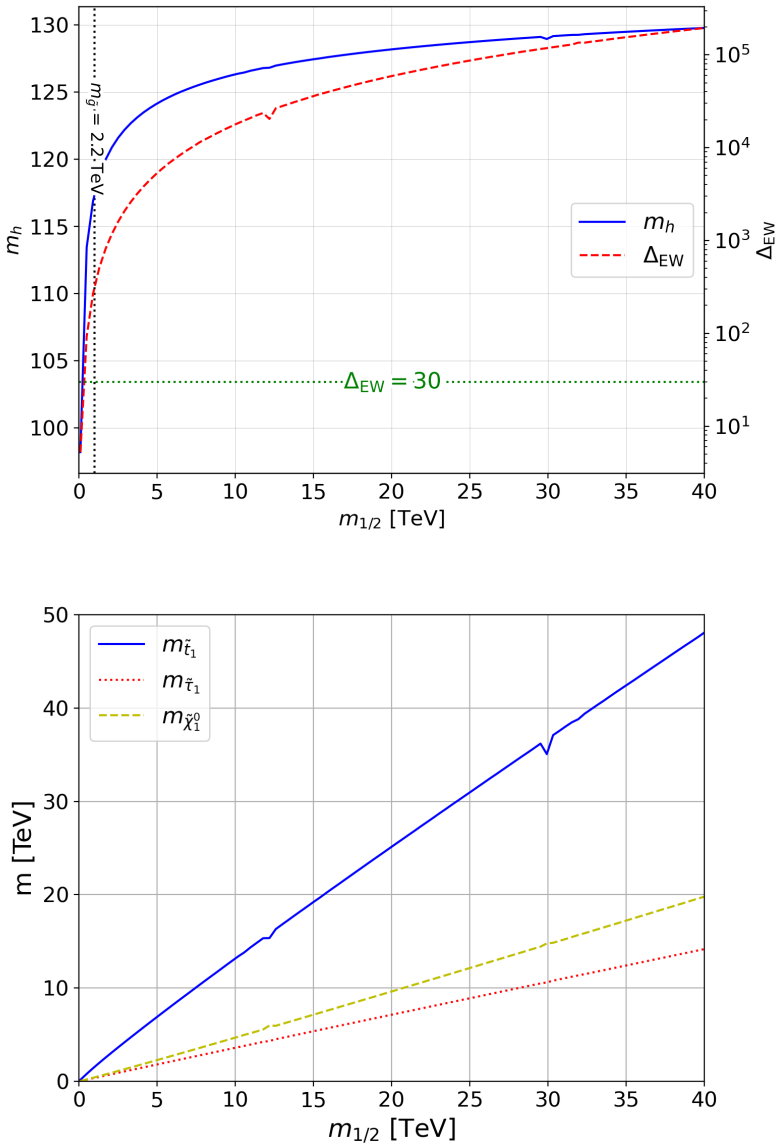


Figure 2.3: Plot of *a)* m_h (left vertical axis, blue curve) and Δ_{EW} (right vertical axis, red curve) vs. $m_{1/2}$ in the inoMSB model for $\tan\beta = 10$ and $\mu > 0$. In frame *b)*, we plot several sparticle masses vs. $m_{1/2}$.

compactification to four dimensions. Under hidden sector SUSY breaking, then weak scale soft SUSY breaking terms emerge from Planck-suppressed SUGRA

operators. Scalar masses arise from terms such as

$$\int d^4\theta c_{ij}\frac{X^\dagger X Q_i^\dagger Q_j}{m_P^2}\rightarrow c_{ij}\frac{F_X^\dagger F_X}{m_P^2}\phi_i^*\phi_j \tag{2.12}$$

where the X fields are hidden sector SUSY breaking fields and the Q are visible sector chiral superfields and the θs are superspace coordinates. When the auxiliary X fields gain a SUSY breaking vev F_X, then scalar soft squared masses $m_{ij}^2\sim c_{ij}\frac{F_X^\dagger F_X}{m_P^2}$ arise and if $F_X\sim(10^{11}\text{ GeV})^2$, then weak scale soft scalar mass terms will ensue. In the above, we leave the indices i,j as arbitrary (so long as $Q_i^\dagger Q_j$ is invariant under the assumed (gauge and possibly other) symmetries to emphasize that nonuniversal scalar masses[40, 41, 42] are the rule and not the exception in SUGRA. In this sense, models like CMSSM/mSUGRA with an assumed ad-hoc scalar mass universality are not likely a realistic expression of gravity-mediation. Also, since the scalar masses arise from $F_X^\dagger F_X$, they are not protected by any hidden sector symmetries which might enforce small (weak scale) values.

Gaugino masses in SUGRA arise via

$$\int d^2\theta\frac{YW^\alpha W_\alpha}{m_P}\rightarrow\frac{F_Y}{m_P}\lambda\lambda \tag{2.13}$$

leading to weak scale gaugino masses when the hidden sector field Y attains a SUSY breaking vev F_Y. It is important to notice here that the SUSY breaking field Y must be a gauge singlet and further that generation of gaugino masses leads to a broken R-symmetry in the Lagrangian since the gauginos carry R-charge $+1$.

Trilinear terms arise as

$$\int d^2\theta \frac{Y H_u Q U^c}{m_P} \to \frac{F_Y}{m_P} H_u \tilde{Q} \tilde{u}_R \tag{2.14}$$

etc. so that trilinear soft terms $a_{ijk} \sim m_{weak}$ also develop. As for gaugino masses, the field Y must be a hidden sector singlet.

The SUSY conserving μ term would be expected to arise with $\mu \sim m_P$ whereas phenomenology requires $\mu \sim m_{weak}$. This is the SUSY μ problem[43]. First, μ must be forbidden by some mechanism/symmetry, and then regenerated at the weak scale. We prefer including the SUSY DFSZ axion solution where the global $U(1)_{PQ}$ arises accidentally and approximately from a discrete R-symmetry such as $\mathbf{Z}_{24}^R$[44, 45, 46]. This approach generates $\mu \sim m_{weak}$ via the Kim-Nilles[47] superpotential operator $W \ni \lambda_\mu S^2 H_u H_d / m_P$ thus solving the strong CP problem while generating both PQ and R-parity symmetries. The discrete R-symmetry is strong enough to solve the axion quality problem as well [45].

Bilinear soft terms come from the operator

$$\int d^4\theta X^\dagger X H_u H_d / m_P^2 \to B_\mu \sim (F_X/m_P)^2 \tag{2.15}$$

and are also of order the weak scale [137].

In the next section we will further explore specific gravity mediation models and how they measure up to LHC data and our chosen naturalness measure. There are two cases we will consider: singlet SUSY breaking fields and charged

SUSY breaking fields.

2.3 Singlet SUSY Breaking Fields

First we consider gravity mediation where SUSY is broken by singlet fields. Such models can be created through the process of retrofitting, which works for both gauge [48] and gravity mediation [49]. As an example of retrofitting in gravity mediation, we assume the Polonyi superpotential[50] with a single gauge singlet hidden sector superfield X:

$$W_{Polonyi} = m^2 m_P (X/m_P + \beta) \tag{2.16}$$

where $m^2 \sim m_{3/2} m_P$ and β is dimensionless and ~ 1. The intermediate scale $m \sim 10^{11}$ GeV is needed to generate $m_{soft} \sim m^2/m_P \sim m_{3/2} \sim m_{weak}$, but is awkward to realize in SUGRA where the only mass parameter is the Planck mass m_P.

In retrofitting[49], we replace $m^2 \to W_\alpha W^\alpha / m_P$ where W_α is a hidden sector gauge superfield transforming under hidden sector group $SU(N)$ with coupling g_H. We can assign an R-charge of $+1$ for the gauge superfields and zero for the X superfield. We expect gaugino condensation when the coupling g_H becomes strong at a scale $\langle \lambda\lambda \rangle \sim \Lambda^3 \sim m_{3/2} m_P^2 \sim m_P^3 \exp(-8\pi^2/g_H^2)$ by dimensional transmutation leading to breaking of an R-symmetry of the hidden gauge fields but not SUSY. But then, as a consequence, SUSY is broken by the auxiliary field F_X of X gaining a vev $F_X \sim m_{3/2} m_P$ and $\langle X \rangle \sim m_P$ via the Polonyi

superpotential[6].

In Fig. 2.4, we show the m_0 vs. $m_{1/2}$ plane of the two-extra-parameter non-universal Higgs model with parameter space given by[23, 8]

$$m_0,\ m_{H_u},\ m_{H_d},\ m_{1/2},\ A_0,\ \tan\beta,\ \mathrm{sign}(\mu) \quad \text{(NUHM2)} \tag{2.17}$$

which should be the expected expression of gravity-mediation models with singlets in the hidden sector[40, 41, 42]. The various scalars in different gauge multiplets have non-universal masses, as expected, although this case (for simplicity) takes the different generations of scalars to be (unrealistically) degenerate. The phenomenology will roughly be the same unless the scalars drift into the multi-TeV region. (The case of decoupled quasi-degenerate first/second generation scalars is shown in Ref. [51]; this latter case offers a landscape quasi-degeneracy/decoupling solution to the SUGRA flavor and CP problems[52].) It is convenient to trade the two soft breaking Higgs masses for the weak scale values of μ and m_A via the scalar potential minimization conditions[23]. The plot Fig. 2.4 is generated with Isasugra interfaced with FeynHiggs.

Since we here adopt hidden sector singlets, we also expect gaugino masses $m_{1/2} \sim m_0$ and large A-terms. In Fig. 2.4, we take $A_0 = -1.6m_0$ and $\tan\beta = 10$ with $\mu = 200$ GeV and $m_A = 2$ TeV. The gray regions show disallowed parameter space due to tachyonic sleptons or inappropriate EWSB. The color-shaded regions correspond to different ranges of Δ_{EW}: orange has $\Delta_{EW} > 30$, yellow $\Delta_{EW} > 50$, and green $\Delta_{EW} > 100$ (unshaded region has $\Delta_{EW} < 30$).

The region below the brown contour is excluded by LHC limits that $m_{\tilde{g}} \gtrsim 2.2$ TeV. (The unshaded regions around the gray areas are an artifact of the graphing software used.) We also show contours of m_h as computed by FeynHiggs interfaced with Isasugra. Assuming a $\sim \pm 2$ GeV theory error on m_h, then the region between 123 GeV$< m_h <$ 127 GeV would be allowed by the LHC Higgs mass measurement. From the plot, we see a broad unshaded region in the lower left with $\Delta_{EW} < 30$, corresponding to a derived weak scale (without tuning) comparable to our measured value $m_{weak}^{OU} \sim m_{W,Z,h} \sim 100$ GeV. A large bulge of allowed parameter space actually stands out beyond LHC gluino mass limits. This higher $m_{1/2}$ natural region is actually favored by rather general considerations of the string landscape, where a power-law draw[53, 54, 55] to large soft terms is expected so long as the derived value of the weak scale lies within the ABDS window[56] $m_Z^{OU}/2 \lesssim m_Z^{PU} \lesssim (2-5)m_Z^{OU}$ (where m_Z^{PU} is the pocket-universe value of m_Z while m_Z^{OU} is the Z mass in our universe). Thus, the allowed high $m_{1/2}$ natural region is actually favored by what Douglas[57] calls *stringy naturalness*[58]. The stringy natural region largely has 123 GeV$< m_h <$ 127 GeV due to the large A-terms generated by the presence of hidden sector SUSY breaking gauge singlets [137].

2.4 Charged SUSY Breaking Fields

Charged SUSY breaking is motivated by early renditions of dynamical SUSY breaking[59] wherein SUSY breaking occurs non-perturbatively in the hidden sector

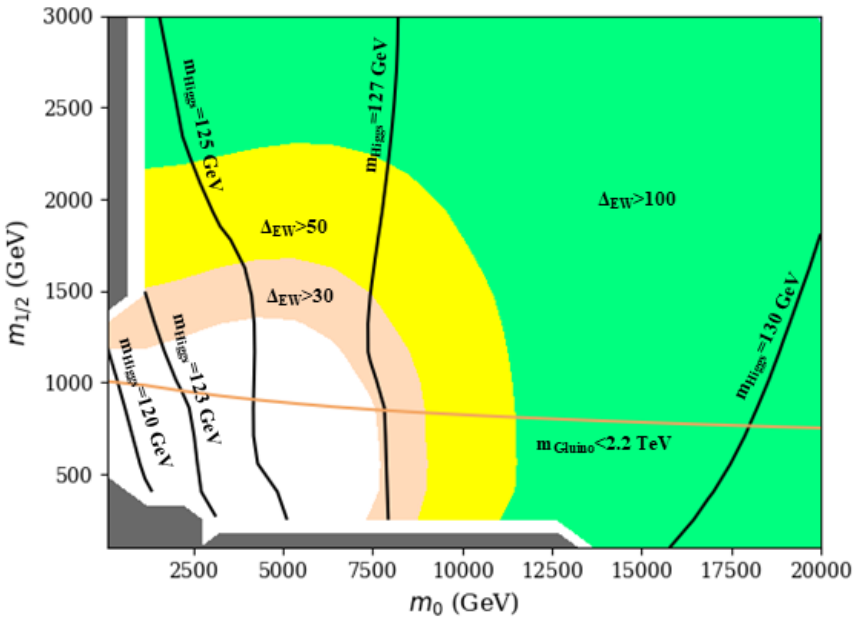


Figure 2.4: Parameter space of the singlet sector gravity-mediation model NUHM2 in the m_0 vs. $m_{1/2}$ plane for $A_0 = -1.6m_0$, $\tan\beta = 10$, $\mu = 200$ GeV and $m_A = 2$ TeV.

perhaps via gaugino condensation[60] $\langle\lambda\lambda\rangle$ where gauginos end up condensing at a scale Λ_{GC} where the hidden sector gauge coupling g_{hidden} becomes strongly interacting. These scales are related by dimensional transmutation to the scale of hidden sector SUSY breaking via $m^2_{hidden} \sim \Lambda^3_{GC}/m_P \sim m^2_P \exp^{-8\pi^2/g^2_{hidden}}$ where g_{hidden} is the asymptotically free hidden gauge sector coupling. In such early models, singlet SUSY breaking fields were scarce or non-existent leading to a gaugino mass problem[61]. This situation motivated the $4-d$ introduction of what became known as anomaly-mediated SUSY breaking[62] (AMSB0).

Charged SUSY breaking[62] led to what became known as PeV-SUSY[63] and then mini-split[64] SUSY; it was emphasized by Wells[65] that a loop-level hierarchy between gauginos and A-terms as compared to scalar soft masses could

ensue. This may have served as an inspiration for split SUSY[66, 67, 68] where the gaugino-to-scalar mass hierarchy was taken to be far larger. Split SUSY predicted the light Higgs to have mass in the range $m_h \sim 140 - 160$ GeV[69] so that once the Higgs was discovered with $m_h \simeq 125$ GeV, the need became apparent to scale back the scalar masses to the 10-100 TeV range which could generate $m_h \sim 125$ GeV even with small A-terms. A drawback in the case of $AMSB$ was that soft slepton masses were derived to be *tachyonic* thus leading to charge-breaking vacua in the scalar potential. Some extra contributions to scalar masses arising from fields propagating in the bulk of spacetime could be postulated to avoid this problem[10].

Charged SUSY breaking (CSB) is well described by the preprogrammed mAMSB model embedded in Isajet. The CSB model has parameter space

$$m_0,\ m_{3/2},\ \tan\beta,\ \mathrm{sign}(\mu) \quad (CSB) \tag{2.18}$$

where the pure AMSB contributions to scalar masses, A-terms and gaugino masses are included. Thus, we expect the loop-suppressed AMSB form for gaugino masses and A-terms but scalar masses can be much larger and are at first approximated by a universal value m_0. The value of B_μ is traded for $\tan\beta$ using the EWSB minimization conditions.

The m_0 vs. $m_{3/2}$ parameter space plane for charged SUSY breaking is shown in Fig. 2.5a) for a fixed value of $\tan\beta = 10$ and $\mu > 0$. The shaded regions are similar to 2.4, with the additional colors blue $\Delta_{EW} > 500$ and purple $\Delta_{EW} > 1000$.

The upper-right disconnected gray regions indicate an instability of the code in calculating the sparticle mass spectra with huge scalar masses. With A_0 small, the lower-left region favored by early phenomenological analyses is then excluded due to too low a value of m_h. From the plot, we see that the m_h-allowed region mainly has $\Delta_{EW} > 1000$, aside from a small sliver just beyond the $m_{\tilde{g}} \sim 2.2$ contour where $\Delta_{EW} \sim 100 - 1000$. Without finetuning, this region would correspond to a derived weak scale in the vicinity of $m_{weak} \gtrsim 2$ TeV, exemplifying the Little Hierarchy Problem.

In Fig. 2.5*b*), we adopt non-universal scalar masses with $m_{H_u} \neq m_{H_d} \neq m_0$ so that μ can be set to a natural value $\mu = 200$ GeV. Here, the naturalness problem is improved, but not eliminated, since Δ_{EW} ranges from $40 - 700$ in the region where $m_h \sim 123 - 127$ GeV. Even with a natural value of μ, the small AMSB A_0-term necessitates unnatural top-squark contributions to the weak scale in order to gain $m_h \simeq 125$ GeV in accord with LHC measurements. This corresponds to a predicted weak scale, without fine-tuning, of $m_Z \sim 400 - 1700$ GeV [137].

From these figures, it may appear that anomaly mediation is not a viable candidate for SUSY breaking based on the current limits set forth by the LHC Run II data. This is not the case, as the above models are not representative of every type of anomaly mediation. In the following chapters, we will explore a different formulation, one that is still viable within the known constraints.

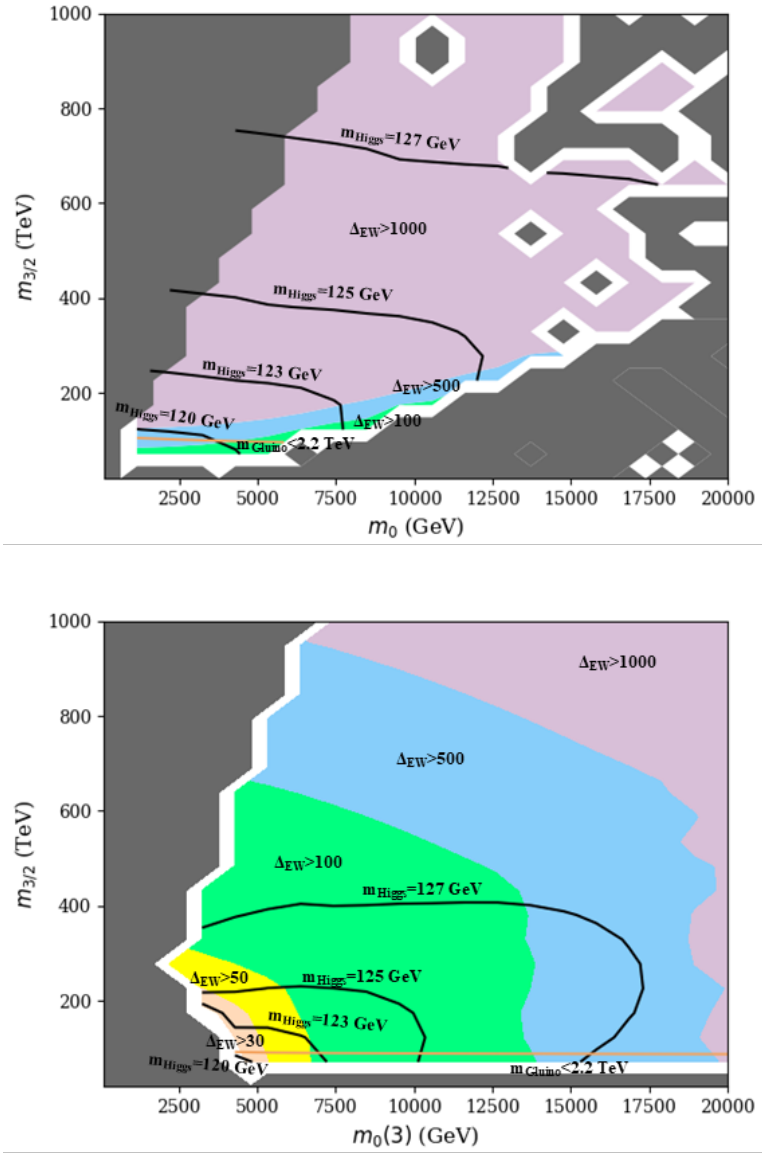


Figure 2.5: Parameter space of charged SUSY breaking (CSB) model with *a*) $\tan\beta = 10$ in the m_0 vs. $m_{3/2}$ plane. In *b*), we show CSB parameter space with non-universal bulk terms such that $\mu = 200$ GeV and $m_A = 2$ TeV but still with A_0 as given by its loop-suppressed AMSB value.

Chapter 3

Analysis of Natural Anomaly Mediated Supersymmetry Breaking

In the previous chapter, we discussed how mAMSB has been ruled out as a result from the following issues:

1. a small value for A_0 means that there is little mixing of the top squarks, thereby making $m_h \simeq 125$ GeV only possible if the stop masses are unnaturally large,
2. the μ parameter is unnaturally large, and
3. the wino LSP may be excluded by current indirect detection dark matter experiments.

Anomaly mediated SUSY breaking is not entirely ruled out, however, as an alternative model presents a promising new avenue to explore.

3.1 Natural anomaly-mediated SUSY breaking (nAMSB)

In Ref. [70], two minor changes to the mAMSB model were suggested to circumvent its undesirable phenomenological properties.[1] First, separate bulk masses for $m_{H_u} \neq m_{H_d} \neq m_0$ were applied to scalar masses which then allowed for a small μ parameter in accord with naturalness (a unified mass m_0 just for matter scalars is highly motivated by the fact that the matter superfields are unified within the

[1]These "changes" were actually suggested as default parameters in the original RS paper Ref. [10].

16-dimensional spinor rep of $SO(10)$). Second, bulk contributions to trilinear soft terms A_0 were advocated which then allowed for large stop mixing which in turn uplifts the Higgs mass $m_h \to\sim 125$ GeV[71] without requiring the stop sector to lie in the unnatural multi-TeV range or beyond. These two adjustments allowed for EW naturalness and for $m_h \sim 125$ GeV. Models with these attributes were denoted as *natural* AMSB (nAMSB):

$$m_0(i),\ m_{H_u},\ m_{H_d},\ m_{3/2},\ A_0,\ \tan\beta \quad (nAMSB') \tag{3.1}$$

where we also allow for possible non-universal bulk contributions to the different generations $i = 1 - 3$. It is convenient to then trade the high scale parameters $m_{H_u}^2$ and $m_{H_d}^2$ for weak scale parameters μ and m_A using the scalar potential minimization conditions[23, 8] leading to

$$m_0(i),\ m_A,\ \mu,\ m_{3/2},\ A_0,\ \tan\beta \quad (nAMSB). \tag{3.2}$$

Like mAMSB, the nAMSB model has winos as the lightest of the gauginos. Unlike mAMSB, the nAMSB model allows for *higgsinos as the lightest EWinos*, in accord with naturalness. By requiring the natural axionic solution to the strong CP problem, one then expects mixed axion plus higgsino-like WIMP dark matter[72, 32], and one can circumvent the constraints on wino-only dark matter[**?**, 15].

3.2 nAMSB from the Landscape

The advent of the string theory landscape[74, 75] led to some major changes in SUSY models with AMSB soft terms. First, it was found that flux compactification[76] of type IIB string models on Calabi-Yao orientifolds led to enormous numbers of string vacuum states (10^{500} is a prominently quoted number[77, 78] although much larger numbers have also been found in F-theory compactifications[79]). Such large numbers of vacuum possibilities allow for Weinberg's[80] anthropic solution to the cosmological constant (CC) problem and "explains" the finetuning of Λ_{CC} to a part in 10^{120}. Then, if the CC is finetuned by anthropics, might one also allow for the little hierarchy $m_{weak} \ll m_{soft}$ to also be finetuned? In split SUSY, electroweak naturalness is eschewed while WIMP dark matter and gauge coupling unification are retained[65, 66, 67]. A possible model framework for split SUSY would then be charged SUSY breaking[68, 63], wherein tree level gaugino masses (and A-terms) are forbidden by some symmetry (perhaps R-symmetry?) while scalar masses are allowed as heavy as one likes. Values of $m_{scalar} \sim 10^9$ GeV were entertained, leading to a signature of long-lived gluinos. The heavy scalars also allowed for a decoupling solution to the SUSY flavor and CP problems[81]. In split SUSY, one expects light Higgs masses in the $m_h \sim 130 - 160$ GeV range[69, 82], in contrast to the 2012 Higgs discovery with $m_h \simeq 125$ GeV. To accommodate the measured Higgs mass, scalar masses were dialed down to the 10^3 TeV range. These *minisplit* models[64, 83] then allowed for $m_h \sim 125$ GeV while still potentially allowing for a decoupling solution to the SUSY flavor and CP problems.

However, only recently has the occurrence frequency of highly finetuned SUSY models been examined in an actual landscape context. In Ref. [84], a toy model of the landscape was developed, and it was shown that EW *natural* models should be more likely than finetuned models to emerge from a generic landscape construction. In retrospect, the reason is rather simple. In Agrawal *et al.*[56] (ABDS), it was found that within a multiverse wherein each pocket universe would have a different value for its weak scale, then only complex nuclei, and hence complex atoms (which seem necessary for life as we know it) would arise if the pocket universe value of the weak scale were within a factor of a few of its measured value in our universe (OU): $0.5m_{weak}^{OU} \lesssim m_{weak}^{PU} \lesssim 5m_{weak}^{OU}$. We call this range of m_{weak}^{PU} the ABDS window. Now in models where all contributions to the weak scale (to the RHS of Eq. 2.9) are natural (in that they lie within the ABDS window), then the remaining parameter selection (typically either $\mu(weak)$ or $m_{H_u}(weak)$) will also have a wide range of possibilities, all lying within the ABDS window, to gain an ultimate value for m_{weak} within the ABDS window. On the other hand, if any contribution to m_{weak} is far beyond m_{weak}, then finetuning is needed and only a tiny portion of parameter space will lead to $m_{weak} \sim 100$ GeV. This scheme was then used in Ref. [85] to compute relative probabilities P_μ for different natural and finetuned SUSY models (and the SM) to emerge from the landscape. For instance, from Ref. [85], it was found that for a radiative natural SUSY model, where all contributions to the weak scale lie within the ABDS window, a relative probability $P_\mu \sim 1.4$ was computed whilst the SM, valid up to the reduced Planck mass m_P, had $P_\mu \sim 10^{-26}$. Also, split SUSY– with scalar masses

at 10^6 TeV– had $P_\mu \sim 10^{-11}$. Other models such as CMSSM[86], PeV-SUSY[63], spread SUSY[87], minisplit[64], high-scale SUSY[88] and G_2MSSM[89] were also examined and found to have tiny values of P_μ. Thus, while the emergence of EW fine-tuned models is logically possible from the landscape, their likelihood is highly suppressed compared to natural models: natural SUSY models are much more plausible as a low energy effective field theory (LE-EFT) realization of the string landscape [15].

3.3 Sparticle and Higgs masses in $nAMSB$ from the landscape

Here, we scan over parameters with a landscape-motivated m_{soft}^1 (linear) draw to large soft terms[53, 90]:

- $m_{3/2}:\ 80-400$ TeV,
- $m_0(1,2):\ 1-20$ TeV,
- $m_0(3):\ 1-10$ TeV,
- $A_0:\ 0-\pm 20$ TeV,
- $m_A:\ 0.25-10$ TeV,
- $\tan\beta:\ 3-60$ (flat scan).

In accord with naturalness, we fix $\mu = 250$ GeV. In lieu of requiring the pocket-universe value of m_Z^{PU} to lie within the ABDS window, we instead invoke $\Delta_{EW} < 30$

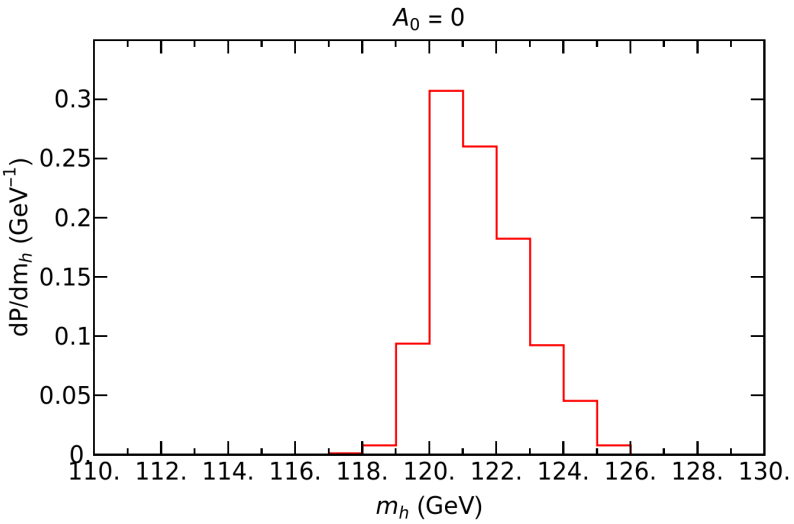


Figure 3.1: Plot of dP/dm_h from an $n = 1$ landscape scan in the nAMSB0 model where $A_0 = 0$.

to avoid finetuning from terms beyond the ABDS window: the finetuned solutions are much more rare compared to non-finetuned (natural) solutions because in the finetuned case the scan parameter space rapidly shrinks to a tiny interval[84, 85]. For the present case, we restrict the landscape to those vacuum solutions which lead to the nAMSB model as the low energy effective field theory, but where the contributions to the soft breaking terms scan over this restricted portion of the multiverse.

Our first results are shown in Fig. 3.1 for the nAMSB0 model where A_0 is fixed at zero. In this case, we see that the probability distribution peaks at $m_h \sim 120$ GeV and falls sharply with increasing m_h. While some probability still exists for $m_h \sim 125$ GeV, we henceforth move beyond nAMSB0 to the nAMSB model with $A_0 \neq 0$ where prospects for generating a Higgs mass m_h in accord with LHC data are much better.

Our first results for nAMSB are shown in Fig. 3.2. In frame *a*), we show the differential probability distribution dP/dm_h vs. m_h, where P is the probability normalized to unity. The red histogram shows the full probability distribution while the blue-dashed histogram shows the same distribution after LHC sparticle mass limits are imposed. We see that dP/dm_h has only small values for $m_h \lesssim 123$ GeV, but then peaks sharply in the range $m_h \sim 125 - 127$ GeV. This is in accord with similar results in models with unified gaugino masses[90] or mirage-mediated gaugino masses[91]: basically, the soft terms $m_0(1,2)$, $m_0(3)$, A_0, m_A and $m_{3/2}$ are selected to be as large as possible subject to the condition that the derived value of m_Z^{PU} lies within the ABDS window. This pulls the stop soft terms $m_0(3)$ large into the ~ 5 TeV range (but not too large) and also the bulk term A_0 to large– nearly maximal– mixing values, but not so large as to lead to CCB minima of the scalar potential (CCB or no-EWSB minima must be vetoed as not leading to a livable universe as we know it). These conditions pull m_h up to the vicinity of ~ 125 GeV.

In frame *b*) the distribution in pseudoscalar Higgs mass m_A, where m_A contributes directly to the weak scale through Eq. 2.9 since for $m_{H_d} \gg m_Z$, then $m_A \simeq m_{H_d}$ (and $m_H \sim m_{H^\pm} \sim m_A$). Here, we see that m_A reaches peak probability around ~ 2.5 TeV, somewhat beyond the reach of HL-LHC[92]. Maximally, m_A can extend up to ~ 6 TeV before overcontributing to the weak scale.

In Fig. 3.3, we show the probability for selected nAMSB model input parameters. In frame *a*), the distribution $dP/dm_{3/2}$ rises to a broad peak between $m_{3/2}: 100-250$ TeV and cuts off sharply around 300 TeV. The upper cutoff on $m_{3/2}$

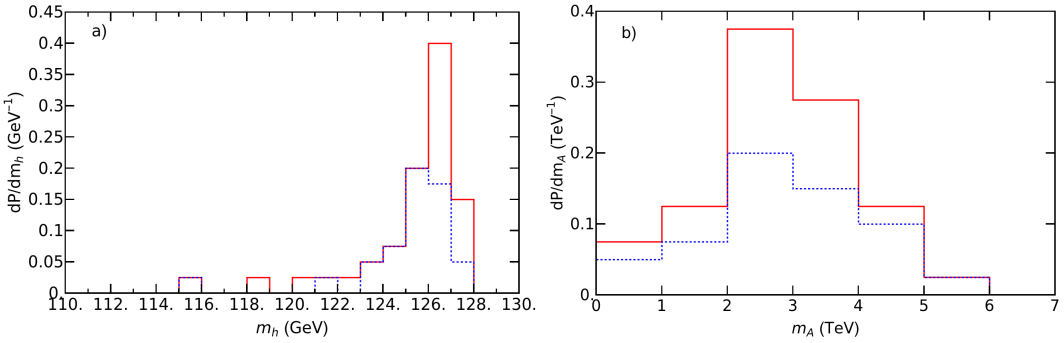


Figure 3.2: Plot of *a*) dP/dm_h and *b*) dP/dm_A, from an $n = 1$ landscape scan in the nAMSB model. The red histogram shows the full probability distribution while the blue-dashed histogram shows the remaining distribution after LHC sparticle mass limits are imposed.

occurs because as $m_{3/2} \to 300$ TeV, then $m_{\tilde{g}}$ is pulled beyond $5-6$ TeV. In this case, the coupled RGEs pull stop masses so high that $\Sigma_u^u(\tilde{t}_{1,2})$ start contributing too much to the weak scale. In frame *b*), we show the distribution in first/second generation sfermion soft mass $m_0(1,2)$. Here, the distribution rises steadily to the scan upper limit since first/second generation sfermion contributions to the weak scale $\Sigma_u^u(\tilde{f}_{1,2})$ are proportional to the corresponding fermion Yukawa coupling. This pull to multi-TeV values of first/second generation squarks and sleptons provides a landscape amelioration of the SUSY flavor and CP problems[52]. We also show as a black-dashed histogram the results from a special run with increased upper scan limit of $m_0(1,2) < 50$ TeV. In this case, the distribution peaks at $m_0(1,2) \sim 15-30$ TeV before getting damped by the anthropic condition that m_Z^{PU} lies within the ABDS window. In frame *c*), we show the distribution in third generation soft term $m_0(3)$. In this case, the distribution peaks at ~ 5 TeV albeit with a distribution extending between $2-10$ TeV. The reason for the upper

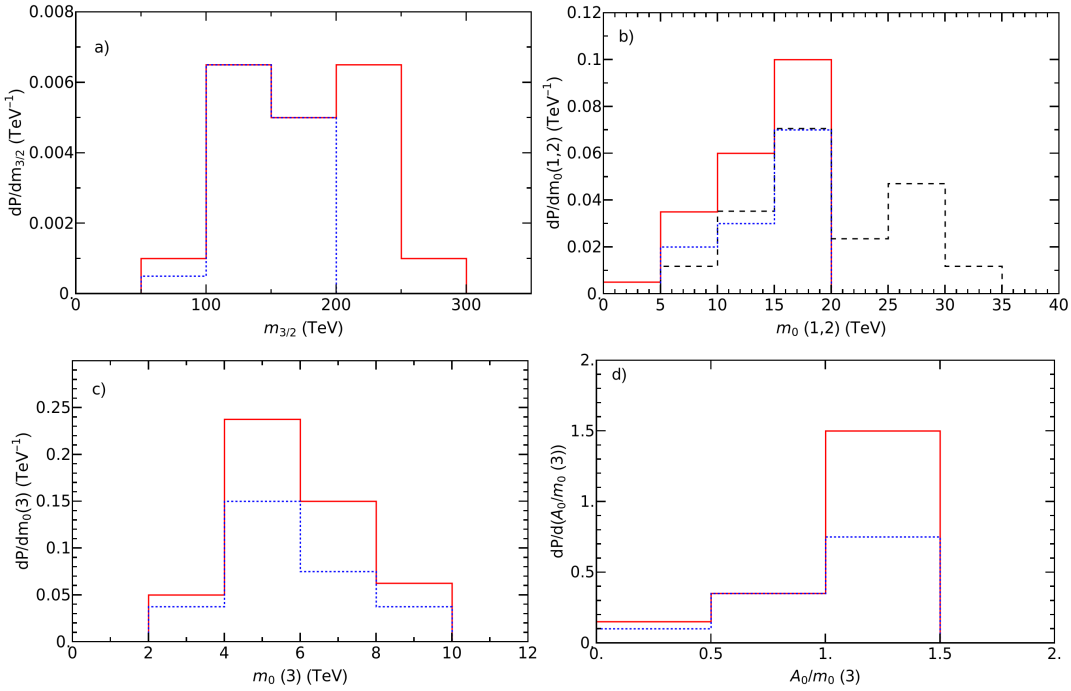


Figure 3.3: Plot of *a*) $dP/dm_{3/2}$, *b*) $dP/dm_0(1,2)$, *c*) $dP/dm_0(3)$ and *d*) $dP/d(A_0/m_0(3))$ from an $n = 1$ landscape scan in the nAMSB model. The red histogram shows the full probability distribution while the blue-dashed histogram shows the remaining distribution after LHC sparticle mass limits are imposed.

cutoff is usually that the $\Sigma_u^u(\tilde{t}_{1,2})$ contribution to the weak scale becomes too large. Finally, in frame *d*), we show the distribution in the ratio $A_0/m_0(3)$. This distribution shows the prediction of large bulk A-terms which actually suppress the contributions of $\Sigma_u^u(\tilde{t}_{1,2})$ to the weak scale[29]. But if A_0 gets too big, then one is pulled into CCB vacua[93] which fail the anthropic criteria.

In Fig. 3.4, we show the $n = +1$ landscape probability distribution predictions for various sparticle masses. In frame *a*), we show the distribution in gluino mass $m_{\tilde{g}}$. The distribution begins around $m_{\tilde{g}} \sim 2$ TeV and peaks at $m_{\tilde{g}} \sim 3 - 4.5$ TeV. This "stringy natural"[58] distribution can explain why it was likely that LHC

would not discover weak scale SUSY via gluino pair production at Run 2, and why gluino pair searches may even elude HL-LHC searches[94]. The light stop mass distribution is shown in frame *b*), and predicts $m_{\tilde{t}_1} \sim 1 - 2.5$ TeV which is mostly within range of HL-LHC[95]. In frame *c*), we show the distribution in $m_{\tilde{\chi}_2^\pm}$ which is approximately the wino mass M_2. Here, the bulk of the probability distribution lies between $M_2 \sim 300 - 700$ GeV, making wino pair production an inviting target for LHC searches. In Fig. 3.4*d*), we show the distribution in mass difference of the two lightest neutralinos: $m_{\tilde{\chi}_2^0} - m_{\tilde{\chi}_1^0}$. This mass gap is relevant for the reaction $pp \to \tilde{\chi}_1^0 \tilde{\chi}_2^0$ where $\tilde{\chi}_2^0 \to f\bar{f}\tilde{\chi}_1^0$ and thus provides a kinematic upper bound for the $m(f\bar{f})$ invariant mass. From the distribution, the mass gap peaks between 10-15 GeV with a tail extending out to 40 GeV (and even beyond) [15].

3.4 *AMSB* benchmark points and model lines

In this section, we compile three AMSB model benchmark points using the Isajet 7.91 code[20] for sparticle and Higgs mass spectra. The 7.91 version includes several fixes which give better convergence in the nAMSB model than previous versions.

3.4.1 *mAMSB* benchmark

In Table 3.1, we list three AMSB model benchmark points from three different AMSB models, but with similar underlying parameters which are convenient for comparison. In Column 2, we list sparticle and Higgs masses for the usual minimal AMSB model[96, 97] where universal bulk scalar contributions m_0^2 were added

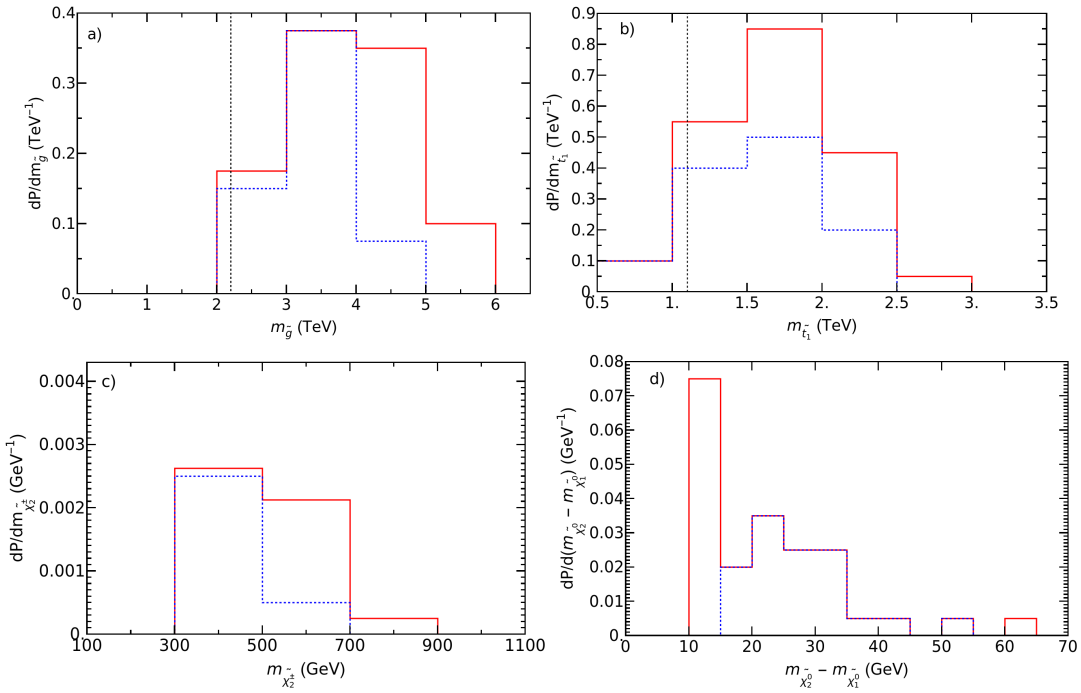


Figure 3.4: Plot of *a)* $dP/dm_{\tilde{g}}$, *b)* $dP/dm_{\tilde{t}_1}$, *c)* $dP/dm_{\tilde{\chi}_2^\pm}$ and *d)* $dP/d(m_{\tilde{\chi}_2^0} - m_{\tilde{\chi}_1^0})$ from an $n = 1$ landscape scan in the nAMSB model. The red histogram shows the full probability distribution while the blue-dashed histogram shows the remaining distribution after LHC sparticle mass limits are imposed.

to all AMSB scalar soft masses but no bulk A_0 terms were included. We take $m_{3/2} = 125$ TeV and $\tan\beta = 10$ with $m_0 = 5$ TeV. The μ term is finetuned to a value $\mu = 1719$ GeV to ensure $m_Z = 91.2$ GeV, so the model will be highly finetuned with $\Delta_{EW} = 711$ (as listed). The gluino mass $m_{\tilde{g}} = 2.73$ TeV so that gluinos are safely beyond LHC Run 2 search limits which require $m_{\tilde{g}} \gtrsim 2.3$ TeV (in simplified models). The light Higgs mass $m_h = 120.3$ GeV: too light compared to its measured value (and so this BM point is ruled out). The LSP is wino-like with mass $m_{\tilde{\chi}_1^0} = 366$ GeV while $\tilde{\chi}_2^0$ is binolike and the $\tilde{\chi}_{3,4}^0$ and $\tilde{\chi}_2^\pm$ are higgsinolike with mass $\sim \mu$. The top-squark is not very mixed with $m_{\tilde{t}_1} = 3.43$ TeV, safely above LHC stop search limits. With a wino-like LSP, the thermally-produced relic abundance $\Omega_{\tilde{\chi}}^{TP}h^2 = 0.009$, underabundant by a factor ~ 13. Thus, non-thermal wino production mechanisms would need to be active to fulfill the relic abundance with pure wino dark matter, which would then be ruled out by indirect WIMP detection experiments, where winos could annihilate strongly in dwarf galaxies, thus yielding high energy gamma rays in violation of limits[73] from Fermi-LAT and HESS. Alternatively, a tiny abundance of wino DM could be allowed if some other particle such as axions constituted the bulk of dark matter[98, 15].

3.4.2 $nAMSB0$ benchmark

Benchmark point nAMSB0 shows the expected sparticle and Higgs mass spectra from the generalized AMSB model inspired by DSB where hidden sector singlets are not allowed. This leads to allowed– but non-universal– scalar masses whilst gaugino masses and A-terms are suppressed and thus assume their loop-suppressed

parameter	mAMSB	nAMSB0	nAMSB
$m_{3/2}$	125000	125000	125000
$\tan\beta$	10	10	10
$m_0(1,2)$	5000	10000	10000
$m_0(3)$	5000	5000	5000
A_0	0	0	6000
μ	1718.8	250	250
m_A	5185.3	2000	2000
$m_{\tilde{g}}$	2728.1	2803.0	2802.4
$m_{\tilde{u}_L}$	5460.8	10211.8	10210.9
$m_{\tilde{u}_R}$	5484.4	10289.0	10312.1
$m_{\tilde{e}_R}$	4965.1	9918.6	9889.4
$m_{\tilde{t}_1}$	3428.4	3165.3	1487.9
$m_{\tilde{t}_2}$	4564.6	4253.6	3657.9
$m_{\tilde{b}_1}$	4545.6	4238.5	3691.4
$m_{\tilde{b}_2}$	5435.8	5239.3	5165.7
$m_{\tilde{\tau}_1}$	4918.6	4789.1	4692.3
$m_{\tilde{\tau}_2}$	4945.1	4253.6	4978.0
$m_{\tilde{\nu}_\tau}$	4945.7	4940.9	4956.6
$m_{\tilde{\chi}_2^\pm}$	1746.6	393.6	387.9
$m_{\tilde{\chi}_1^\pm}$	366.2	241.2	238.1
$m_{\tilde{\chi}_4^0}$	1745.2	1176.6	1174.2
$m_{\tilde{\chi}_3^0}$	1742.4	402.4	395.0
$m_{\tilde{\chi}_2^0}$	1163.0	260.9	260.4
$m_{\tilde{\chi}_1^0}$	366.0	229.4	226.3
m_h	120.3	120.7	125.0
$\Omega^{TP}_{\tilde{\chi}_1^0}h^2$	0.009	0.01	0.01
$BF(b\to s\gamma)\times 10^4$	3.1	3.2	3.3
$BF(B_s\to\mu^+\mu^-)\times 10^9$	3.8	3.8	3.8
$\sigma^{SI}(\tilde{\chi}_1^0,p)$ (pb)	7.5×10^{-11}	1.8×10^{-8}	1.6×10^{-8}
$\sigma^{SD}(\tilde{\chi}_1^0 p)$ (pb)	1.7×10^{-7}	2.2×10^{-4}	2.6×10^{-4}
$\langle\sigma v\rangle\vert_{v\to 0}$ (cm^3/sec)	6.1×10^{-25}	2.4×10^{-25}	2.6×10^{-25}
$\Delta_{\rm EW}$	711	60	15.0

Table 3.1: Input parameters and masses in GeV units for the mAMSB, nAMSB0 and nAMSB natural generalized anomaly mediation SUSY benchmark points with $m_t = 173.2$ GeV using Isajet 7.91.

AMSB form. Thus, for nAMSB0 we adopt the parameter space of nAMSB but with $A_0 = 0$. We adopt a natural value of $\mu = 250$ GeV with $m_A = 2$ TeV and also allow for higher first/second generation scalar masses as expected from the landscape, with $m_0(1,2) = 10$ TeV whilst $m_0(3) = 5$ TeV as in the mAMSB benchmark point.

For nAMSB0, the natural value of $\mu = 250$ GeV implies light higgsinos so that while winos are still the lightest gauginos, the higgsinos are the lightest electroweakinos (EWinos), and thus the expected phenomenology markedly changes from mAMSB. The small value of μ also makes the nAMSB0 model much more natural than mAMSB, where Δ_{EW} has dropped to 60. The dominant contributions to Δ_{EW} come now from $\Sigma_u^u(\tilde{t}_{1,2})$. But the model is still somewhat unnatural since the largest contribution to the RHS of Eq. 2.9 is still ~ 500 GeV, outside the ABDS window[56], and thus in need of finetuning. Another problem is the light Higgs mass $m_h = 120.7$ GeV. Both of these issues arise from the rather small AMSB0 value for the trilinear soft terms [15].

3.4.3 *nAMSB* benchmark

In the fourth column of Table 3.1, we list the nAMSB benchmark point which could arise from the sequestered SUSY breaking scenario of RS[10], where in addition to bulk scalar masses, bulk A-terms are also expected. Here, we use the same parameters as in nAMSB0 except now also allow $A_0 = 6$ TeV. The large trilinear soft term leads to large stop mixing which feeds into the m_h value (which is maximal for stop mixing parameter $x_t \sim \sqrt{6}m_{\tilde{t}}$) so that now the value of m_h

is lifted to 125 GeV in accord with LHC measurements. Also, the large positive A-term leads to cancellations in both of $\Sigma_u^u(\tilde{t}_1)$ and $\Sigma_u^u(\tilde{t}_2)$ leading to increased naturalness where now $\Delta_{EW} = 15$. For the nAMSB0 benchmark, the more-mixed lighter stop mass has dropped to just $m_{\tilde{t}_1} \sim 1.5$ TeV, within striking distance of HL-LHC[95, 15].

3.4.4 Corresponding AMSB model lines

In this subsection, we elevate each of the AMSB benchmark points to AMSB model lines where we keep the auxiliary parameters fixed as before but now allow the fundamental AMSB parameter $m_{3/2}$ to vary. We compute the AMSB model line spectra using Isasugra.

In Fig. 3.5, we first show the naturalness measure Δ_{EW} for each model line. For the mAMSB model line, we see that Δ_{EW} starts at ~ 100 for low $m_{3/2} \sim 50$ TeV, and then steadily increases to $\Delta_{EW} \sim 10^4$ for $m_{3/2} \sim 500$ TeV. As for the mAMSB BM point, the dominant contribution to Δ_{EW} comes from the (finetuned) μ parameter. This model line thus seems highly implausible for all $m_{3/2}$ values based on naturalness. We also show the nAMSB0 model line as the orange curve. Here, Δ_{EW} ranges from $50 - 200$ as $m_{3/2}$ varies over $50 - 500$ TeV. While more natural than mAMSB, it still lies outside the ABDS window which is typified by $\Delta_{EW} \lesssim 30$. The blue curve shows the nAMSB model line. In this case, Δ_{EW} ranges from $\sim 15 - 150$. The line $\Delta_{EW} = 30$ is shown by the dashed red curve. Here, we see the model line starts becoming unnatural for $m_{3/2} \gtrsim 265$ TeV.

In Fig. 3.6, we show the computed value of m_h along the three model lines.

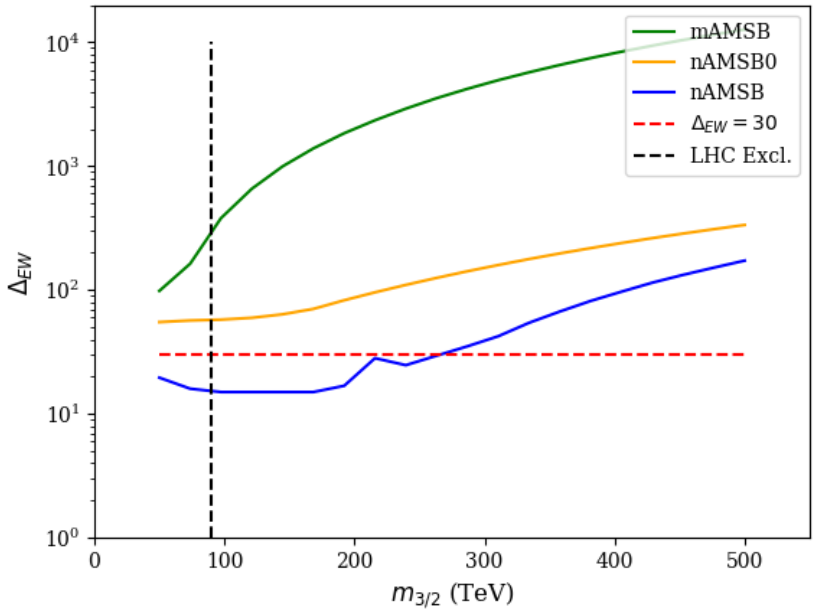


Figure 3.5: Plot of Δ_{EW} vs. $m_{3/2}$ along the AMSB model lines. The horizontal dashed line represents $\Delta_{EW} = 30$ and the region below the dashed line is regarded as natural. The vertical dashed line represents the cutoff to the LHC excluded region for $m_{3/2}$.

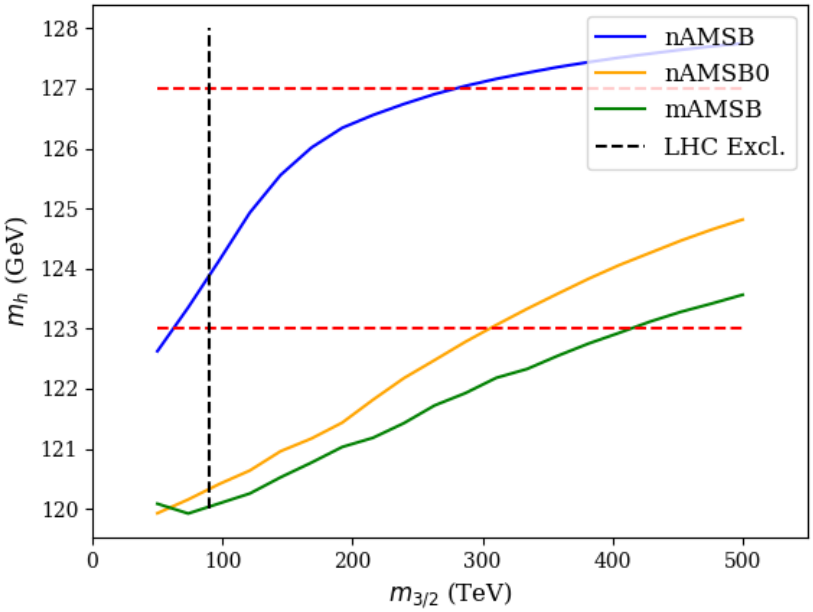


Figure 3.6: Plot of m_h vs. $m_{3/2}$ along the AMSB model lines. The light Higgs mass is constrained by LHC measurements to lie between the dashed lines, given some theory error on the calculation of m_h.

The LHC measured window is between $m_h : 123 - 127$ allowing for a ± 2 GeV theory error in the computed value of m_h. We see that the mAMSB model line enters the allowed region of m_h only for $m_{3/2} \gtrsim 400$ TeV while the nAMSB0 model line enters the allowed m_h range for $m_{3/2} \gtrsim 300$ TeV. Both model lines are highly unnatural for such large $m_{3/2}$ values. However, the nAMSB model line is within the $m_h = 125 \pm 2$ GeV band for $m_{3/2} : 50 - 280$ TeV, consistent with its natural allowed range (thanks to the presence of bulk A_0 terms).

In Fig. 3.7, we show various sparticle masses for the nAMSB model line vs. $m_{3/2}$. The dark and light blue and lavender lines show the various higgsino-like EWinos which are typically of order $m(higgsinos) \sim \mu \sim 250$ GeV. Next heaviest

are the wino-like EWinos $\tilde{\chi}_3^0$ and $\tilde{\chi}_2^\pm$, shown as green and orange curves. These masses vary from $m(winos) : 300 - 2000$ GeV over the range of $m_{3/2}$ shown, and are, as we shall see, subject to present and future LHC EWino searches.

The black curve shows the gluino mass $m_{\tilde{g}} : 1.2 - 10$ TeV. We also show the LHC lower bound $m_{\tilde{g}} \sim 2.3$ TeV from gluino pair searches within the context of simplified models by the black dashed line. The LHC simplified model results should apply well in the case of nAMSB models since the $\tilde{g} - \tilde{\chi}_1^0$ mass gap is aways substantial. The LHC $pp \to \tilde{g}\tilde{g}X$ search limits thus provide a lower bound on allowed nAMSB parameter space with $m_{3/2} \gtrsim 90$ TeV. The blue dashed line denotes the upper limit on $m_{3/2}$ obtained from naturalness constraints. The lighter top squark mass $m_{\tilde{t}_1}$ is also shown, and is beyond the LHC simplified model limit $m_{\tilde{t}_1} \gtrsim 1.1$ TeV for all $m_{3/2}$ values. First/second generation sfermion masses lie around $m_0(1,2)$ value so in this case would be inaccessible to present and future LHC searches. By combining lower limits from LHC gluino pair searches with upper bounds from naturalness, we expect the allowed $m_{3/2}$ values for nAMSB to lie between $m_{3/2} : 90 - 265$ TeV [15].

3.4.5 Exploring nAMSB Parameter Space

We may take our exploration one step further by extending beyond a model line into parameter space. This allows us to determine where in parameter space is left unrestricted by experimental data. In Fig. 3.8 we display the nAMSB parameter space in the A_0 vs. $m_{3/2}$ plane for fixed $m_0(3) = 5$ TeV and $m_0(1,2) = 10$ TeV, with $\tan\beta = 10$ and $m_A = 2$ TeV with *a*) $\mu = 150$ GeV and *b*) $\mu = 250$ GeV (as

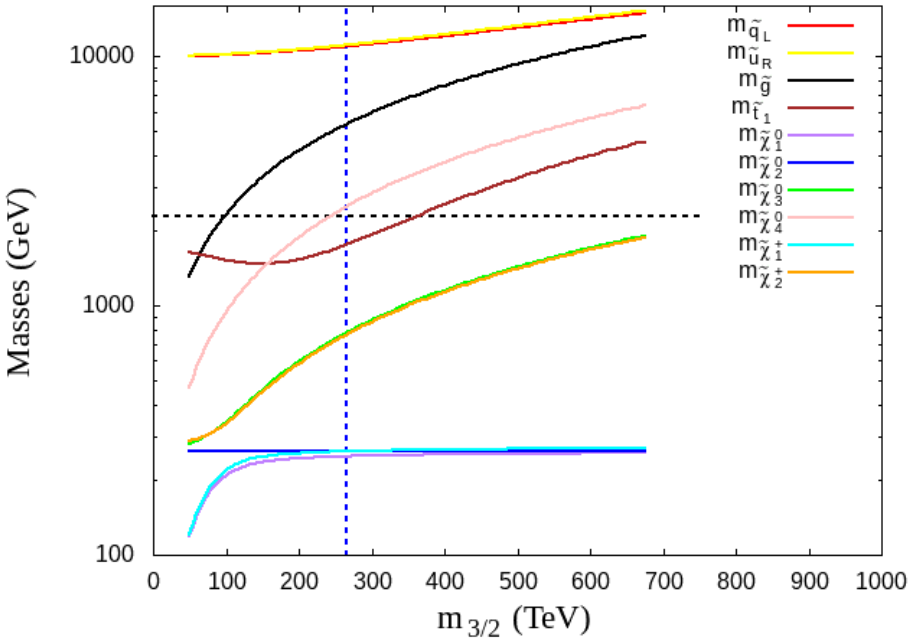


Figure 3.7: Plot of sparticle masses vs. $m_{3/2}$ along the nAMSB model lines. The vertical dashed line represents the upper limit on $m_{3/2}$ imposed by $\Delta_{EW} = 30$ and the horizontal dashed line represents the lower limit of the gluino mass.

before). Here, we find a right-side gray region where large values of A_0 cause $m_{U_3}^2$ to run tachyonic. The bulk of this p-space plane is unnatural with $\Delta_{EW} \gtrsim 50$ except for the region to the right of the naturalness contours. Also, we see that $m_h \sim 125$ GeV mainly on the right-hand-side unless $m_{3/2}$ is very large, in which case the spectra are unnatural. Here it is plain to see the advantage that bulk trilinear terms provide: for $A_0 \sim 0$, then the model is unnatural and yields m_h too light unless $m_{3/2} \gtrsim 300$ TeV. We also show in the plot the orange contours of $m_{\tilde{g}} = 2.2$ TeV (below is excluded) and $m_{\tilde{\chi}_2^+} = 500,\ 600$ and 1000 GeV (between which is excluded by LHC hadronically decaying gaugino pair searches [101]). The remaining non-excluded target p-space lies on the extreme right where $A_0 \sim 5 - 7$ TeV.

The digitized ATLAS exclusion curve is shown in Fig. 3.9 in the $m(wino)$ vs. $m(higgsino)$ plane. Our nAMSB model line with $\mu = 250$ GeV is denoted by the horizontal dashed line. From the plot, we would expect that the range $m(wino) : 625 - 1000$ GeV would be ruled out, corresponding to a range of $m_{3/2} : 200 - 350$ TeV. For model lines with larger or smaller values of μ, the exclusion region changes accordingly in Fig. 3.9.

In Fig. 3.10, we present nAMSB parameter space in the $m_0(3)$ vs. $m_{3/2}$ plane where now we take the $m_0(1,2) = 2m_0(3)$ and bulk trilinear $A_0 = 1.2m_0(3)$. Fig. 3.10 is portrayed for $\tan\beta = 10$ and $m_A = 2$ TeV, with *a*) $\mu = 150$ GeV and *b*) $\mu = 250$ GeV. We use Isajet 7.91 model 13 to compute spectra for the nAMSB model[20]. The left gray region is where sleptons become the LSP. Here, we assume R-parity conservation which is less ad-hoc than it used to be in that both R-parity

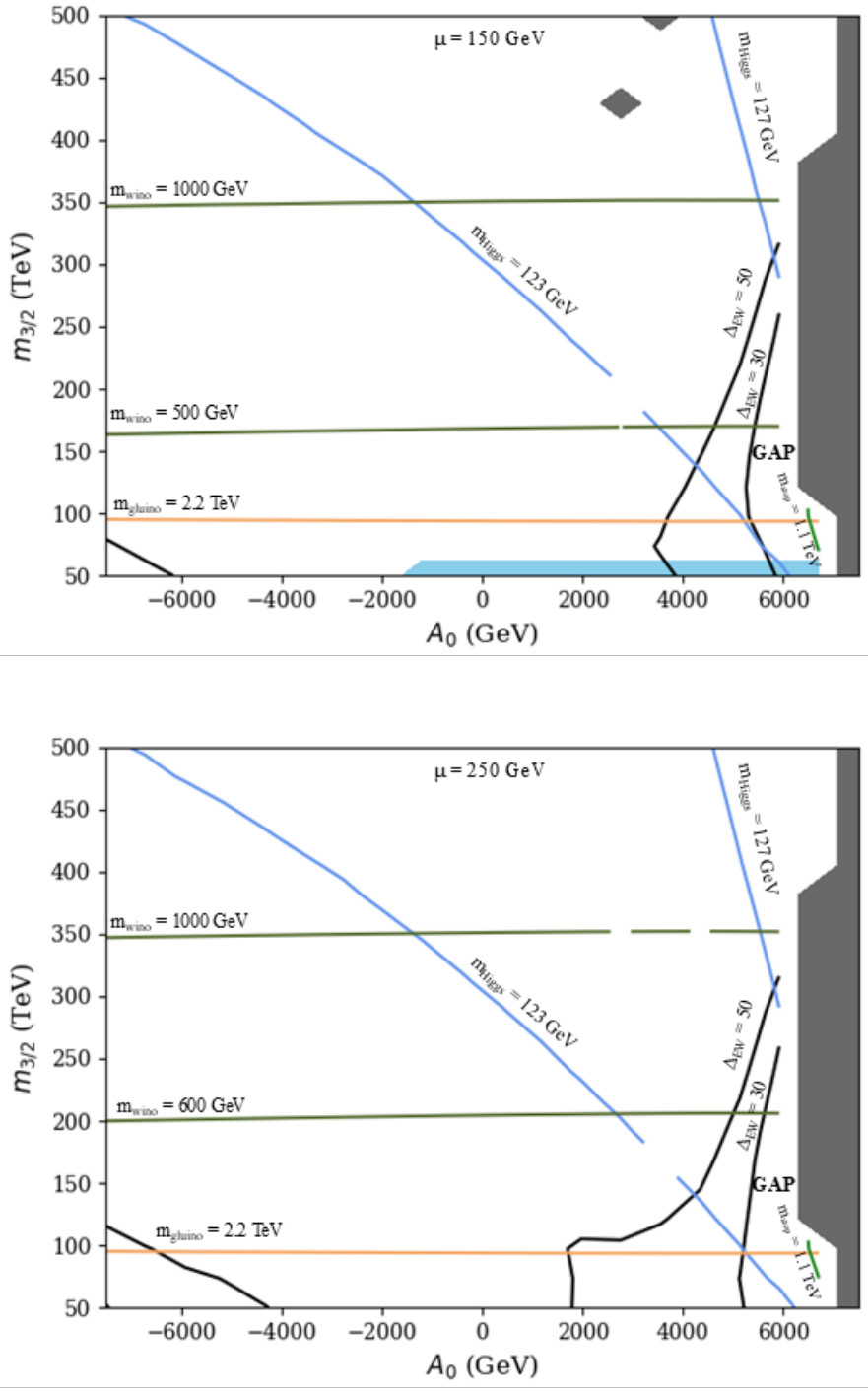


Figure 3.8: Plot of A_0 vs. $m_{3/2}$ parameter space in the nAMSB model for $m_0(3) = 5$ TeV with $m_0(1,2) = 2m_0(3)$ and $\tan\beta = 10$, with $m_A = 2$ TeV and *a*) $\mu = 150$ GeV and *b*) $\mu = 250$ GeV.

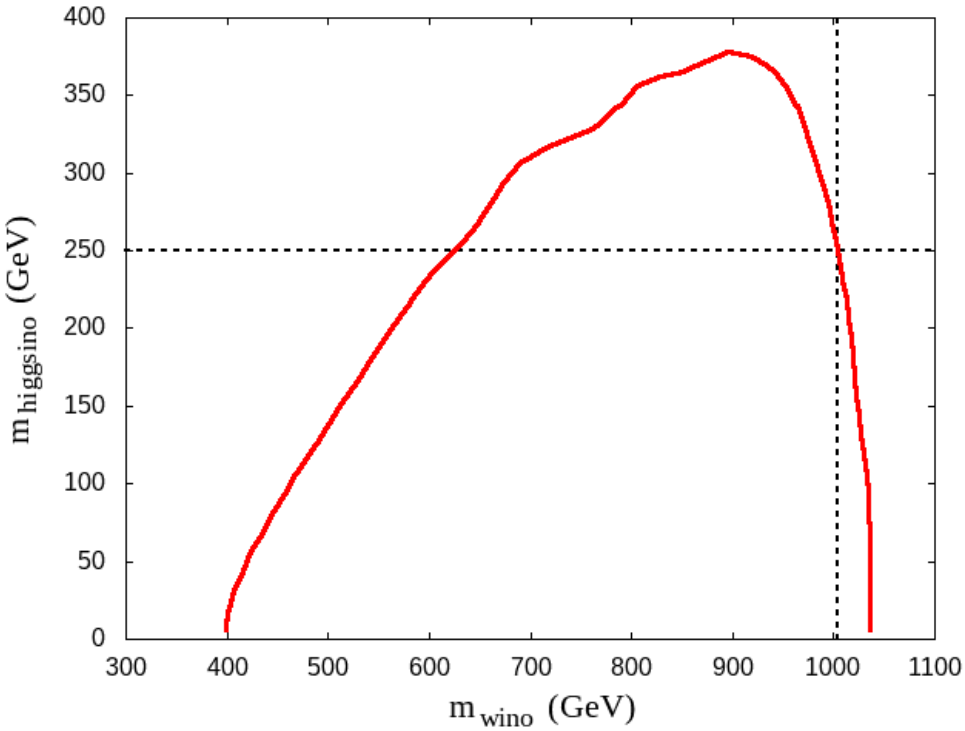


Figure 3.9: Allowed/excluded regions of $m(wino)$ vs. $m(higgsino)$ plane from ATLAS analysis of EWino pair production followed by decay to W, Z, h with decay to boosted dijets. The region below the red contour is excluded by ATLAS searches for boosted, hadronically-decaying winos.

and global $U(1)_{PQ}$ can arise from more fundamental discrete R-symmetries which provide simultaneously solutions both to the SUSY μ problem and also the axion quality problem[45, 46]. Thus, the left gray region is excluded. The lower gray region around $m_0(3) \sim 2000$ GeV is also excluded, this time because stop soft terms run tachyonic leading to charge and/or color breaking (CCB) minima in the scalar potential.

In Fig. 3.10, we also show contours of $m_h = 123$ and 127 GeV. Thus, the region between the $m_h : 123 - 127$ GeV contours is in accord with LHC m_h measurements (due to the large bulk A_0 terms). We also show black contours of electroweak naturalness $\Delta_{EW} = 30$ and 50. The regions below these contours are considered natural since all independent contributions to the weak scale are comparable to the weak scale (no finetuning needed for the LHP). The finetuning increases with $m_{3/2}$ since large $m_{3/2}$ yields a large value of $m_{\tilde{g}}$ and $m_{\tilde{t}_{1,2}}$ which in turn increases the $\Sigma_u^u(\tilde{t}_{1,2})$ contribution to the weak scale. Also, the region with too large $m_0(3)$ is excluded since the large stop sector soft terms lead to too large $\Sigma_u^u(\tilde{t}_{1,2})$ values.

The region of Fig. 3.10 below the orange contour labeled $m_{\tilde{g}} = 2.2$ TeV (for $m_{3/2} \lesssim 90 - 100$ TeV) is excluded by ATLAS/CMS limits on gluino pair production searches[99, 100]. The region between the two green contours labeled $m_{\tilde{\chi}_2^+} = 500,\ 600$ and 1000 GeV is excluded by the ATLAS search for EWinos which decay to W or Z which in turn decay hadronically[101]. This region includes the $\Delta_{EW} = 30$ and 50 contours and so, along with these contours, defines an upper limit to nAMSB parameter space (p-space). The remaining lower-left gap region

is still allowed by naturalness, by the measured value of m_h, by direct/indirect mixed axion/higgsino-like WIMP dark matter searches[73] and by LHC sparticle search limits. This remaining gap provides a target for future LHC upgrade searches for the incarnation of natural SUSY via the nAMSB model [136].

3.4.6 An Alternative $nAMSB$ Model Line

Our goal is to explore the LHC-allowed nAMSB parameter space with $\Delta_{EW} \lesssim 30$ to see if it is completely testable at HL-LHC. To this end, we construct an alternative nAMSB model line that cuts through the bulk of allowed p-space but which varies with $m_{3/2}$ from the lower limit formed by LHC gluino pair searches to the upper limit which is formed by naturalness combined with LHC boosted hadronically-decaying EWino pair searches. Our constructed model line is shown in Fig. 3.10 as the blue diagonal line labeled *Model*. It is parametrized by

$$m_{3/2} = 35 m_0(3) \quad \text{(nAMSB model line)} \tag{3.3}$$

with $m_0(1,2) = 2m_0(3)$, $A_0 = 1.2m_0(3)$ and $\tan\beta = 10$ with $m_A = 2$ TeV and $\mu = 150$ GeV and 250 GeV.

In Fig. 3.11, we plot the value of m_h along the model line with $\mu = 250$ GeV, which extends from $m_{3/2} = 90$ TeV (left-most vertical red-dashed line) to $m_{3/2} \sim 210$ TeV (where LHC gaugino limits set in, denoted by the dashed red line at $m_{3/2} \sim 210$ TeV). From the plot, we see that m_h lies between 123-127 GeV, and so is consistent with the measured value of m_h up to a theory error of ± 2

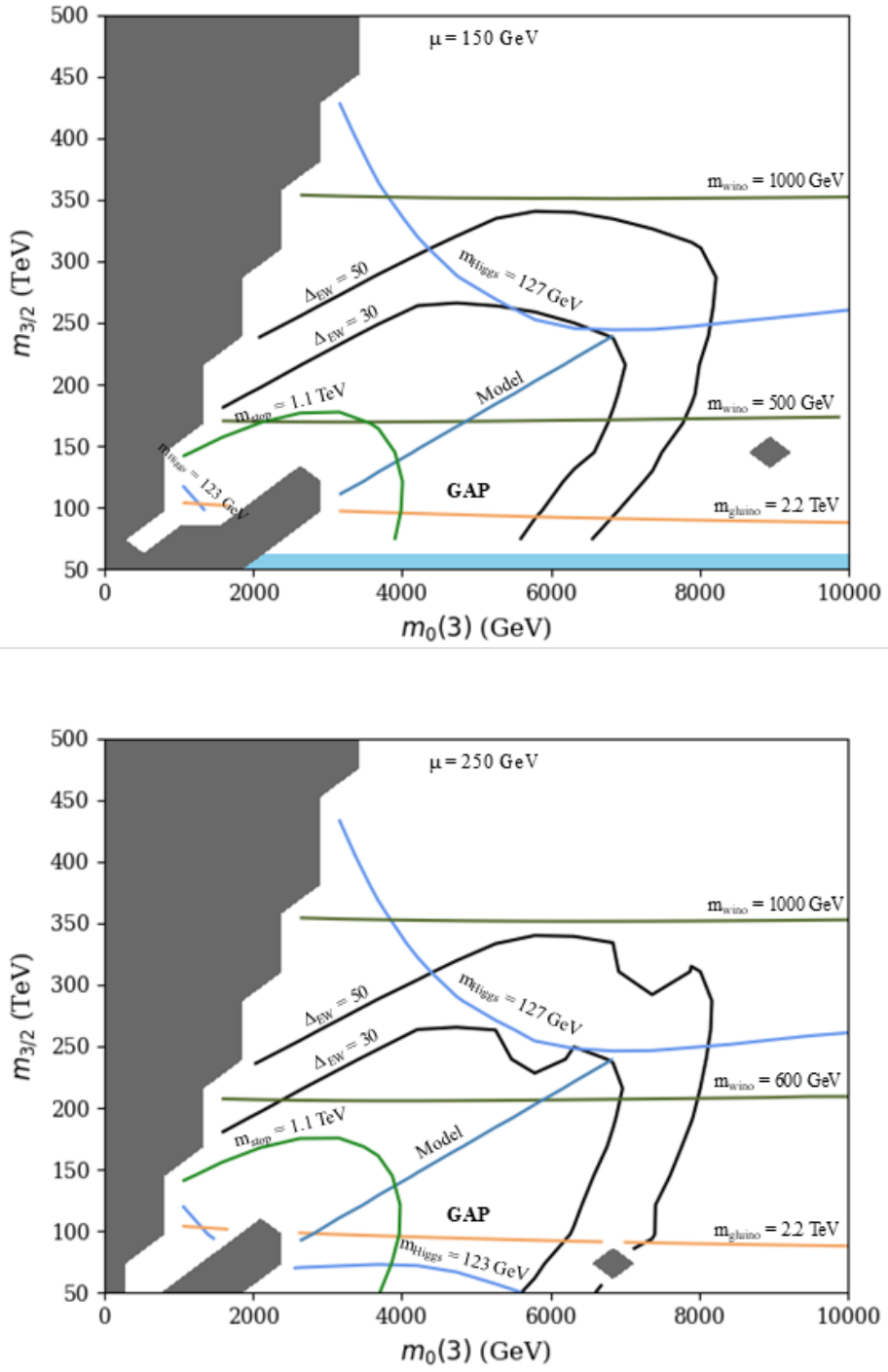


Figure 3.10: Plot of $m_0(3)$ vs. $m_{3/2}$ parameter space in the nAMSB model for $m_0(1,2) = 2m_0(3)$, $A_0 = 1.2m_0(3)$ and $\tan\beta = 10$, with $m_A = 2$ TeV and *a*) $\mu = 150$ GeV and *b*) $\mu = 250$ GeV.

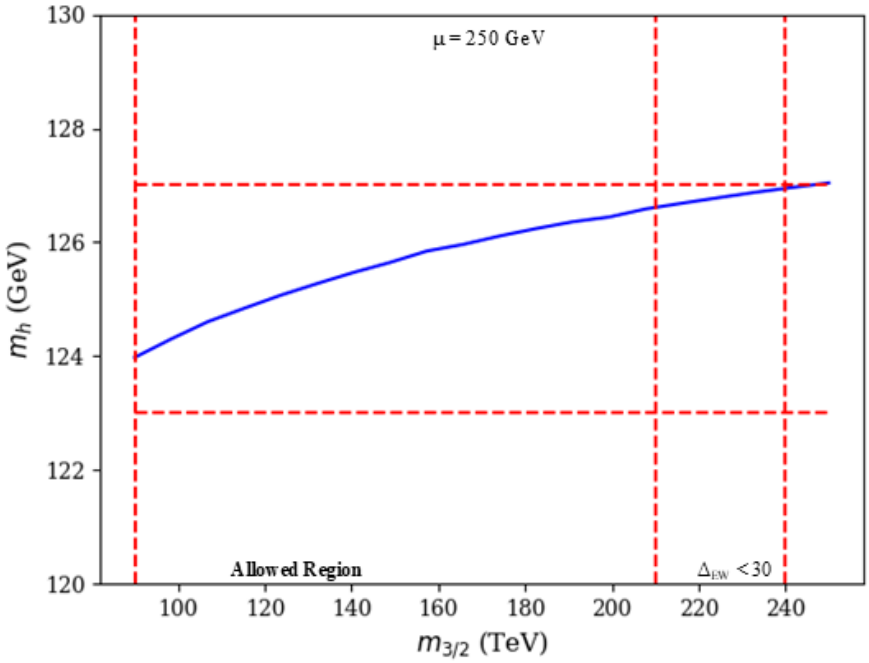


Figure 3.11: Plot of m_h vs. $m_{3/2}$ along the nAMSB model-line for $m_{3/2} = 35m_0(3)$ with $m_0(1,2) = 2m_0(3)$, $A_0 = 1.2m_0(3)$ and $\tan\beta = 10$, with $\mu = 250$ GeV and $m_A = 2$ TeV. The horizontal dashed lines show the upper and lower bounds on m_h. The leftmost vertical line represents where sleptons become the LSP, the middle line shows the value for $m_{3/2}$ where $m_{wino} = 600$ GeV and the rightmost vertical line shows the value of $_{3/2}$ where $\Delta_{EW} = 30$.

GeV.

In Fig. 3.12, we plot the value of Δ_{EW} along the $\mu = 250$ GeV model line. In this case, we find that Δ_{EW} is typically between values of 15-30 along the line until it climbs beyond 30 (the red-dashed line) for $m_{3/2} \gtrsim 240$ TeV.

In Fig. 3.13, we plot various sparticle masses along the nAMSB model line. At the very bottom, the red and purple (nearly overlapping) curves denote the higgsino-like neutralinos $\tilde{\chi}^0_{1,2}$ and their masses are fixed to be very nearly $\sim \mu = 250$ GeV. The next-higher brown curve denotes the neutral wino $m^0_{\tilde{\chi}_3} \sim M_2$

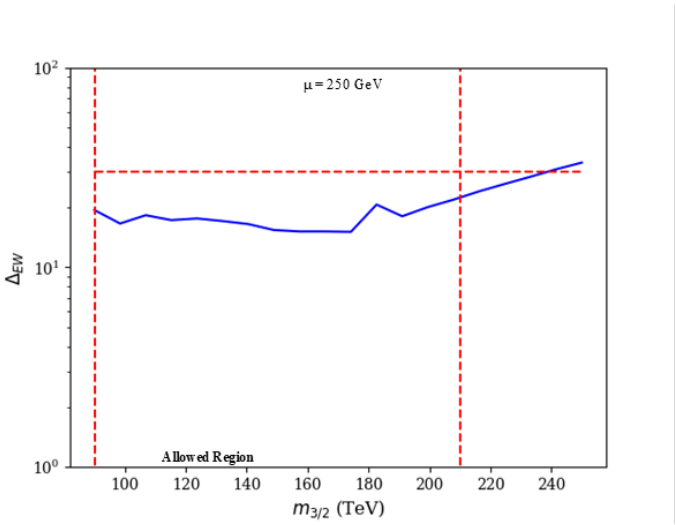


Figure 3.12: Plot of Δ_{EW} vs. $m_{3/2}$ along the nAMSB model-line for $m_{3/2} = 35m_0(3)$, $m_0(1,2) = 2m_0(3)$, $A_0 = 1.2m_0(3)$ and $\tan\beta = 10$, with $\mu = 250$ GeV and $m_A = 2$ TeV. The left vertical line represents where sleptons become the LSP and the right line shows the value for $m_{3/2}$ where $m_{wino} = 600$ GeV. The horizontal dashed line represents $\Delta_{EW} = 30$.

and these masses range between 275-600 GeV in the allowed region. Such light winos provide an inviting target for LHC searches since even higher values are already excluded by the LHC boosted EWino search results. The green curve shows the lighter top-squark mass $m_{\tilde{t}_1}$ which extends over the range $m_{\tilde{t}_1} : 0.6 - 2$ TeV. (The lower part of this range is already excluded by LHC top-squark searches within simplified models[99, 100].) The bino mass $m_{\tilde{\chi}_4^0}$ lies just above $m_{\tilde{t}_1}$ for this model line. Meanwhile, the gluino mass varies from $m_{\tilde{g}} : 2.2 - 4.5$ TeV while first/second generation sfermions lie in the 5-15 TeV range. For our HL-LHC search strategy, we will focus on the relatively light higgsinos and winos along this model line.

With our model lines now established, in the next chapter we will study the

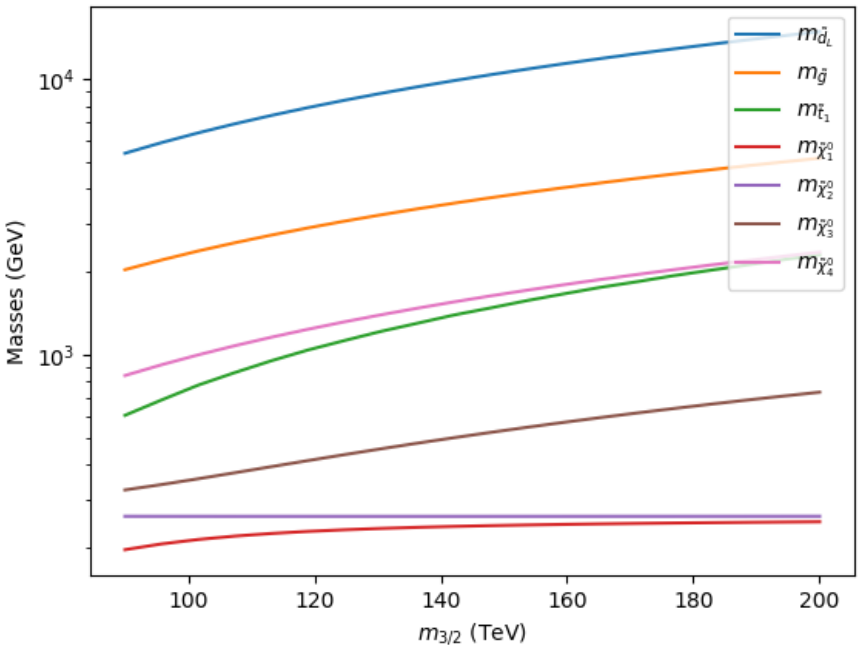


Figure 3.13: Plot of various sparticle masses vs. $m_{3/2}$ along the nAMSB model-line for $m_{3/2} = 35m_0(3)$ with $m_0(1,2) = 2m_0(3)$, $A_0 = 1.2m_0(3)$ and $\tan\beta = 10$, with $\mu = 250$ GeV and $m_A = 2$ TeV.

nAMSB discovery channels at the LHC and LHC-HL detectors [136].

Chapter 4

Detection Channels for Natural Anomaly Mediated SUSY Breaking at the LHC

4.1 LHC production cross sections

In this section, we pivot to prospects for LHC searches for SUSY within the context of the nAMSB model. First, we adopt the computer code PROSPINO[102] to compute the NLO production cross sections for various $pp \to SUSY$ reactions, given input from the Isajet SUSY Les Houches Accord (SLHA) file[103]. Our first results are shown in Fig. 4.1 where we show cross sections for $pp \to \tilde{g}\tilde{g}$, $\tilde{t}_1\tilde{t}_1^*$ and (summed) EWino pair production vs. $m_{3/2}$ along the nAMSB model line. At the top of the plot, we see EWino pair production is dominant and relatively flat vs. $m_{3/2}$ since it is dominated by higgsino pair production and μ is fixed at 250 GeV. The EWino cross section are divided up into summed $\tilde{\chi}_i^0\tilde{\chi}_j^0$, $\tilde{\chi}_i^0\tilde{\chi}_k^\pm$ and $\tilde{\chi}_k^\pm\tilde{\chi}_l^\mp$ production, where $i,j = 1-4$ and $k,l = 1-2$. The summed EWino pair cross sections are all comparable and of order $\sim 10^2$ fb. The $pp \to \tilde{t}_1\tilde{t}_1^*$ cross section is also relatively flat, this time reflecting that $m_{\tilde{t}_1}$ hardly changes with increasing $m_{3/2}$ (from Fig. 3.7). The $pp \to \tilde{g}\tilde{g}$ cross section is falling rapidly with increasing $m_{3/2}$, reflecting that the gluino mass is directly proportional to $m_{3/2}$. From the plot, we thus expect most of the reach of LHC for the nAMSB model will come from EWino pair production rather than from gluino or stop pair production.

There are many subreactions that contribute to the summed EWino pair

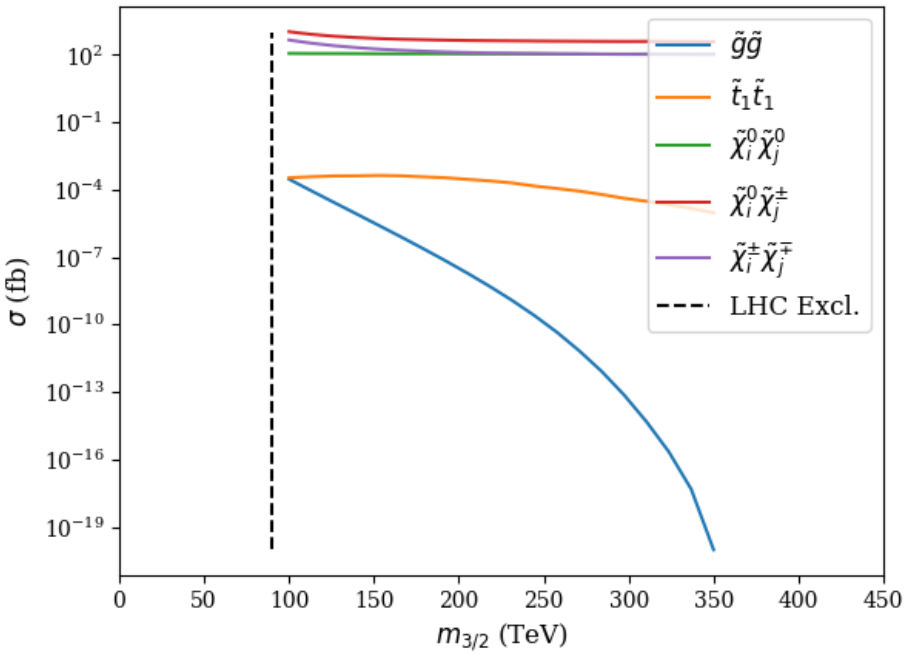


Figure 4.1: Plot of $\sigma(pp \to \tilde{g}\tilde{g},\ \tilde{t}_1\tilde{t}_1^*)$ and EWino pair production vs. $m_{3/2}$ along the nAMSB model line.

production cross sections. Each subreaction leads to different final states and thus different SUSY search strategies. In Fig. 4.2a), we show the several chargino-chargino pair production reactions vs. $m_{3/2}$. The upper blue curve denotes $\tilde{\chi}_1^+\tilde{\chi}_1^-$ where the light charginos are mainly higgsino-like (except for some substantial mixing at low $m_{3/2}$ where the wino soft term $M_2 \sim \mu$). Given the small $m_{\tilde{\chi}_1^+} - m_{\tilde{\chi}_1^0}$ mass gap, where much of the reaction energy goes into the invisible LSP mass and energy, this reaction is likely to be largely invisible at LHC. The orange curve denotes charged wino pair production: $\tilde{\chi}_2^+\tilde{\chi}_2^-$. Given its modest size and the branching fractions from Sec. 4.2, it can be very promising for LHC searches. The third reaction, mixed higgsino-wino $\tilde{\chi}_1^\pm\tilde{\chi}_2^\mp$ production, occurs at much lower rates.

In Fig. 4.2b), we show the ten neutralino pair production reactions $\sigma(pp \to \tilde{\chi}_i^0\tilde{\chi}_j^0)$. By far, the dominant neutralino pair production reaction is $pp \to \tilde{\chi}_1^0\tilde{\chi}_2^0$. This reaction takes place dominantly via s-channel Z^* exchange involving the coupling W_{ij} of Eq. 8.101 of Ref. [6]. The signs of the neutralino mixing elements add constructively in this case leading to a large higgsino pair production reaction that leads to promising LHC signature in the soft opposite-sign dilepton plus jets plus $\not{E}_T$ channel[104, 105] (OSDLJMET). This cross section is flat with increasing $m_{3/2}$ since μ is not a soft term and not expected to directly scan in the landscape, but instead is fixed by whatever solution to the SUSY μ problem attains[43]. The next largest neutralino pair production cross section is $pp \to \tilde{\chi}_2^0\tilde{\chi}_3^0$: wino-higgsino production, which again has a constructive sign interference along with large mixing terms. Other neutralino pair production reactions are subdominant and

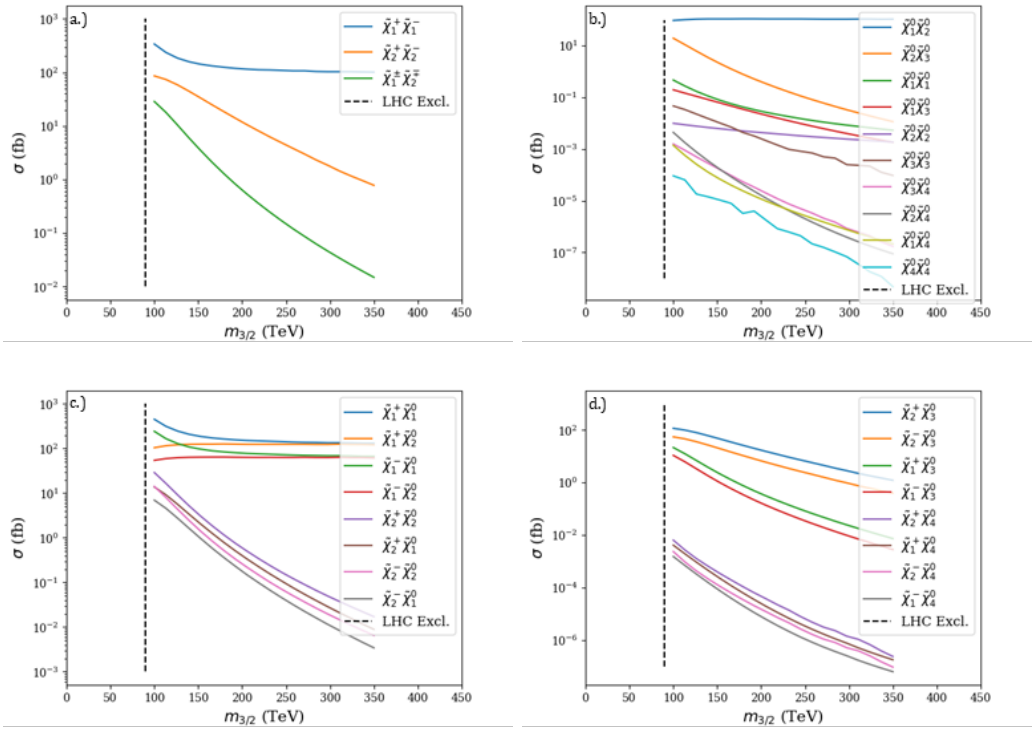


Figure 4.2: Plot of various EWino pair production cross sections vs. $m_{3/2}$ along the nAMSB model line: *a*) chargino pair production, *b*) neutralino pair production, *c*) chargino-$\tilde{\chi}^0_{12}$ pair production and *d*) chargino-$\tilde{\chi}^0_{3,4}$ pair production.

typically decreasing with increasing $m_{3/2}$.

In Fig. 4.2*c*), we show $\tilde{\chi}^0_{1,2}\tilde{\chi}^{\pm}_k$ pair production reactions. The largest, $\tilde{\chi}^0_1\tilde{\chi}^+_1$, may again be largely invisible to LHC searches while the second largest $\tilde{\chi}^0_2\tilde{\chi}^+_1$ can contribute to the OSDLJMET signature mentioned above. The corresponding reactions with negative charginos are comparable to these reactions but somewhat suppressed since they occur mainly via s-channel W^* production and LHC is a pp collider which favors positively charged W bosons. The remaining higgsino-wino production reactions fall with increasing $m_{3/2}$ and are subdominant.

In Fig. 4.2*d*), we show the $\tilde{\chi}^0_{3,4}\tilde{\chi}^{\pm}_k$ production rates. In this case, wino pair production $\tilde{\chi}^0_3\tilde{\chi}^+_2$ is dominant but falling as $m_{3/2}$–and hence M_2– increases in value. The conjugate reaction $\tilde{\chi}^0_3\tilde{\chi}^-_2$ reaction is next largest, followed by $\tilde{\chi}^0_3\tilde{\chi}^{\pm}_1$. The reactions involving bino production $\tilde{\chi}^0_4$ are all subdominant and may not be so relevant for LHC SUSY searches [15].

4.2 Sparticle decay modes

In this section, we wish to comment on some relevant sparticle branching fractions leading to favorable final state search signatures for LHC. It is evident from the preceding Section that EWino pair production is the dominant sparticle production mechanism at LHC14. The reaction $pp \to \tilde{\chi}^0_1\tilde{\chi}^0_2$ (neutral higgsino pair production) is dominant, where $\tilde{\chi}^0_2 \to f\bar{f}\tilde{\chi}^0_1$ and where the f are SM fermions. For the case of nAMSB, the mass gap $m_{\tilde{\chi}^0_2} - m_{\tilde{\chi}^0_1}$ can range up to 50-60 GeV when winos are light, leading to substantial wino-higgsino mixing for lower values

of $m_{3/2} \sim 100$ TeV. The lucrative leptonic branching fraction $\tilde{\chi}_2^0 \to \ell^+\ell^-\tilde{\chi}_1^0$ occurs typically at the 2% level due to competition with other decay modes such as $\tilde{\chi}_2^0 \to \tilde{\chi}_1^\pm f\bar{f}'$.

The other lucrative production mode from the previous section is wino pair production $pp \to \tilde{\chi}_3^0\tilde{\chi}_2^\pm$. To assess the expected final states from this reaction, we plot in Fig. 4.3 the major wino decay branching fractions along the nAMSB model line. In frame *a*), we plot the $BF(\tilde{\chi}_2^+)$ values vs. $m_{3/2}$ while in frame *b*) we plot the $BF(\tilde{\chi}_3^0)$ values. From frame *a*), the region with $m_{3/2} \lesssim 90$ TeV is already excluded by LHC $\tilde{g}\tilde{g}$ searches (albeit in the context of simplified models). Below 90 TeV, there is actually a level-crossing: since μ is fixed at 250 GeV, a low enough value of $m_{3/2}$ leads to $m(wino) < m(higgsino)$ and an *increased* $m_{\tilde{\chi}_2^+} - m_{\tilde{\chi}_1^+}$ mass gap (see Fig. 3.7) so that $\tilde{\chi}_2^+ \to \tilde{\chi}_1^+ h$ is allowed. Then, as $m_{3/2}$ increases, the mass gap drops (due to wino-higgsino degeneracy) and the $\tilde{\chi}_2^+ \to \tilde{\chi}_1^+ h$ mode becomes kinematically closed. As $m_{3/2}$ increases beyond ~ 100 TeV, then $\tilde{\chi}_2^+$ becomes wino-like, and the mass gap enlarges so that the decay $\tilde{\chi}_2^+ \to \tilde{\chi}_1^+ h$ becomes allowed again. As $m_{3/2}$ increases further, then all four decay modes $\tilde{\chi}_2^+ \to \tilde{\chi}_1^0 W^+$, $\tilde{\chi}_2^0 W^+$, $\tilde{\chi}_1^+ Z$ and $\tilde{\chi}_1^+ h$ asymptote to $\sim 25\%$. Thus, we expect the charged wino to decay to higgsino plus W, Z or h in a ratio $\sim 2:1:1$. Since the higgsinos may be quasi-visible (depending on decay mode and mass gap), then we get wino decay to W, Z or h +quasi-visible higgsinos as a final state.

In Fig. 4.3*b*), we show the neutral wino $\tilde{\chi}_3^0$ branching fractions along the nAMSB model line. At low $m_{3/2} \sim 90$ TeV near the LHC-excluded region, the

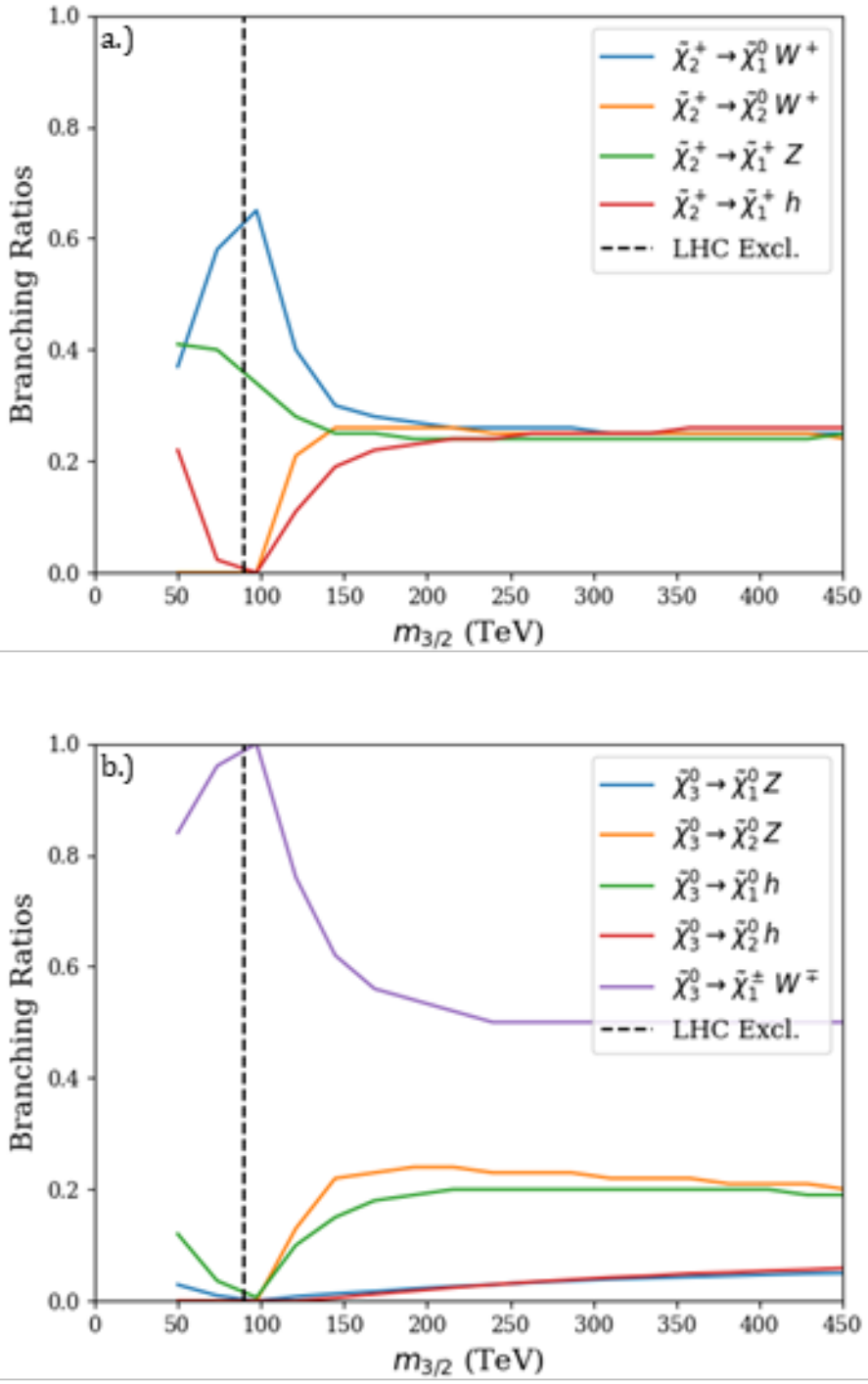


Figure 4.3: Plot of charged and neutral wino branching fractions *a*) BF($\tilde{\chi}_2^+$) and *b*) BF($\tilde{\chi}_3^0$) versus $m_{3/2}$ along the nAMSB model line.

neutral winos decay nearly 100% into $\tilde{\chi}_1^{\mp}W^{\pm}$. As $m_{3/2}$ increases, the wino-higgsino mass gap increases, and decays to $\tilde{\chi}_2^0 Z$ and $\tilde{\chi}_1^0 h$ are allowed and can occur at the $\sim 20\%$ level while decays to $\tilde{\chi}_1^{\mp}W^{\pm}$ asymptote to $\sim 50\%$. The remaining branching fraction goes to mixing-suppressed modes. Thus, for wino pair production, we expect a final state of $VV + MET$, $Vh + MET$ and $hh + MET$ where MET stands for missing transverse energy and V stands for the vector bosons W and Z. The MET may not really be entirely missing since it may include 3-body decay products of the heavier higgsinos.

In Fig. 4.4, we plot the light top squark branching fractions $BF(\tilde{t}_1)$ vs. $m_{3/2}$ along the nAMSB model line. For very low $m_{3/2}$, $\tilde{t}_1 \to b\tilde{\chi}_2^+$ is dominant where the $\tilde{\chi}_2^{\pm}$ is mixed wino-higgsino. But as $m_{3/2}$ increases, $BF(\tilde{t}_1 \to b\tilde{\chi}_1^+)$ becomes dominant and approaches 50%, not unlike natural SUSY models with gaugino mass unification[106]. The $\tilde{t}_1$ in nAMSB (as in NUHM2 models) is dominantly $\sim \tilde{t}_R$ in spite of large stop mixing soft term A_t. Also, at larger $m_{3/2}$ values, $BF(\tilde{t}_1 \to t\tilde{\chi}_{1,2}^0)$ each approach $\sim 25\%$ [15].

4.3 LHC excluded regions

Certain regions of nAMSB model parameter space seem already excluded by existing LHC13 search limits from Run 2 with ~ 139 fb^{-1} of integrated luminosity.

4.3.1 LHC constraint from gluino pair searches

In the case of gluino pair production, for the bulk of LHC-allowed nAMSB parameter space, we expect $\tilde{g} \to t\tilde{t}_1^*$ followed by further $\tilde{t}_1$ cascade decays. The

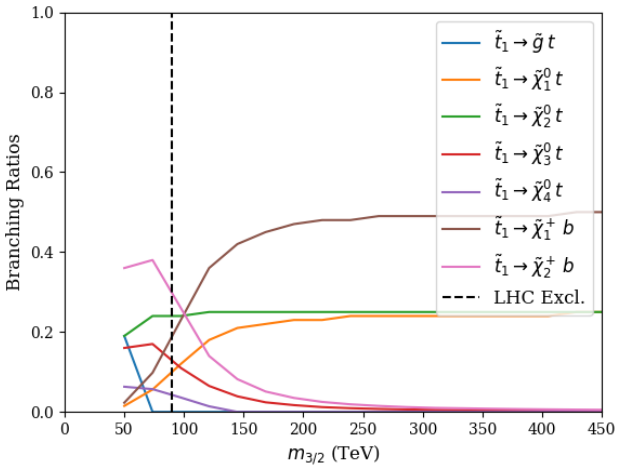


Figure 4.4: Plot of top squark branching fractions BF($\tilde{t}_1$) versus $m_{3/2}$ along the nAMSB model line.

approximate ATLAS and CMS simplified model limits for $\tilde{g}\tilde{g}$ production followed by decay to third generation particles should roughly apply[107, 108, 109], and these imply

$$m_{\tilde{g}} \gtrsim 2.3 \text{ TeV}. \tag{4.1}$$

From Fig. 3.7, this implies that $m_{3/2} \gtrsim 90$ TeV [15].

4.3.2 LHC constraint from EWino pair production followed by decay to boosted dijets

An ATLAS study[101] reports searching for EWino pair production followed by two-body decays to W, Z or h. These heavy SM objects are assumed to decay hadronically to boosted dijet/fat-jet states which are then identified. A similar study by CMS was also made[110], but with smaller parameter space exclusion regions. The simplified model limits presented in Fig. 14c) of Ref. [101] should

roughly apply to our case for wino-pair production $pp \to \tilde{\chi}_2^{\pm}\tilde{\chi}_3^0$ as shown in Fig. 4.2*d*) followed by decays to vector bosons and Higgs bosons as shown in Fig. **??**.

4.3.3 LHC constraints from SModelS/CheckMATE2 analysis

To test for further limits on nAMSB parameter space, we employ two recent recasting softwares: `SModelS`[111, 112, 113] and `CheckMATE2` (CM2)[114, 115] to study the impact of the current searches on nAMSB parameter space. `SModelS` is a popular tool for interpreting simplified-model results from the LHC. It decomposes Beyond the Standard Model (BSM) collider signatures presenting a Z_2-like symmetry into Simplified Model Spectrum (SMS) topologies and compares the BSM predictions for the LHC in a model independent framework with the relevant experimental constraints. The main variable for comparison of a BSM theory to the LHC experimental searches is the r-ratio which is defined as the ratio of the expected $\sigma \times BR$ for a specific final state to the corresponding upper limit on the $\sigma \times BR \times \epsilon$ (where ϵ is the acceptance efficiency provided by the experimental paper). `CheckMATE2` is a reinterpretation software for interpreting LHC results for all BSM models. It is based on recasting the full experimental analyses using events after full Monte Carlo simulation, hadronization and detector smearing of the final state objects and implementing the cuts as in the experimental analyses. It provides the r value defined as the ratio of the expected number of events from the signal, after implementing all cuts, to the 95%CL upper limit from the experimental result. In both cases, for a BSM model to be allowed by current constraints, one requires $r < 1$.

The wino-higgsino mass gap, quantified by $\Delta m_{31} = m_{\widetilde{\chi}_3^0} - m_{\widetilde{\chi}_1^0}$, increases with $m_{3/2}$ as seen in Fig. 4.5. Fig. 4.6 shows the variation of the highest r value obtained from `SModelS` and `CheckMATE2` for the $\sqrt{s} = 13$ TeV results from LHC. The highest r-value defined as the ratio of the signal over the 95%CL upper limit from the signal region is plotted against $m_{3/2}$. The red dotted lines denote the constraints from the ATLAS search of boosted hadronically decaying bosons + $\not{E}_T$[101] while the black dotted line denote the bound from the gluino searches implying $m_{3/2} \geq 90$ TeV as discussed in Section 4.3.2 and 4.3.1 respectively.

For the constraints from the `CheckMATE2` CMS results (blue), we observe the tightest constraints arise from the multi-lepton (2/3) $+\not{E}_T$ searches[116] for $m_{3/2} \sim 150$ TeV with r-value ~ 0.15 and it falls off on either side of the peak. This is due to other searches gaining more importance such as searches for $\geq 4\ell + \not{E}_T$ for larger mass-gaps between the wino-like and higgsino-like neutralino. From the `CheckMATE2` ATLAS result (green), the r-value decreases with increasing $m_{3/2}$ from $r = 0.25$ arising from the hadronic searches of squarks and gluinos [117].

From `SModelS` (red), the most stringent constraint occurs at $m_{3/2} < 100$ TeV from searches of three leptons $+\not{E}_T$[118]. For $m_{3/2} = 100 - 250$ TeV range, the most stringent constraints arise from the boosted hadronically decaying diboson $+\not{E}_T$ searches the multi-lepton searches involving two or three leptons$+\not{E}_T$[119, 118] are the most sensitive searches near the peak at $m_{3/2} \sim 225$ TeV. For higher $m_{3/2} = 250 - 400$ TeV, the dominant constraints arise from the multi-lepton searches and sub dominant constraints arise from the boosted hadronically decaying dibosons $+\not{E}_T$. As $m_{3/2}$ increases, the multijet $+\not{E}_T$[120] searches start constraining the

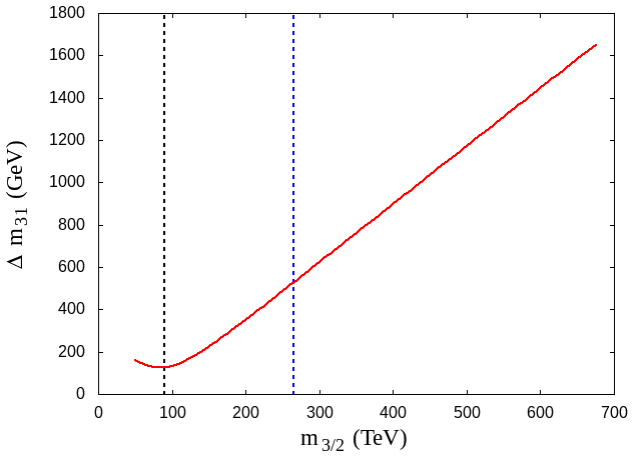


Figure 4.5: Variation of $\Delta m_{31} = m_{\widetilde{\chi}_3^0} - m_{\widetilde{\chi}_1^0}$ vs. $m_{3/2}$. The region left of the black-dashed curve is excluded by LHC13 gluino pair searches and the region to the right of the blue-dashed line is unnatural with $\Delta_{EW} \gtrsim 30$.

parameter space dominantly. However, the r-value always remains less than 1: thus, the remaining allowed range of $m_{3/2} \sim 90 - 200$ TeV appears to be presently allowed [15].

4.3.4 LHC-allowed nAMSB parameter space

Our final allowed nAMSB model line parameter space is shown in Fig. 4.7. The left gray shaded region is excluded by LHC gluino search limits while the central gray shaded region is excluded by the ATLAS limits on EWino pair production followed by decay to two boosted dijet final states. The naturalness limit is denoted by the vertical dashed line within the central excluded band: the region to the right is unnatural, and thus highly unlikely (but not impossible) to emerge from the landscape. The unshaded region extends from $m_{3/2}$: $90 - 200$ TeV and is thus the presently allowed parameter space. For convenience, we display

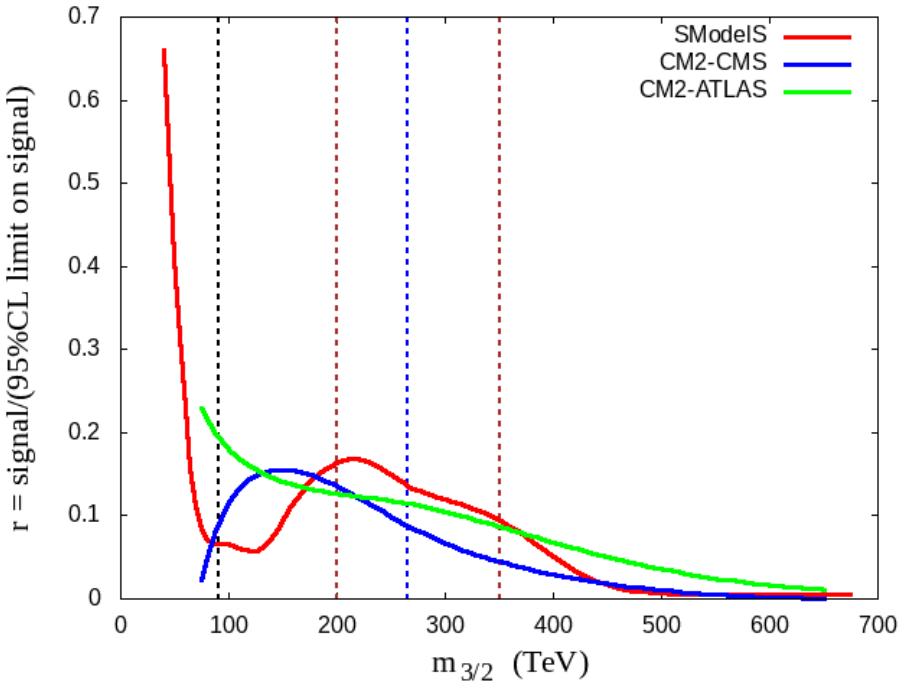


Figure 4.6: Plot of r from `SModelS` and `CheckMate2` vs. $m_{3/2}$ along the nAMSB model line.

again the sparticle masses along our nAMSB model line. The remaining SUSY particle spectrum for $m_{3/2} \sim 90 - 200$ TeV should provide a target for future LHC searches seeking to discover or to rule out natural AMSB [15].

4.4 nAMSB discovery channels for HL-LHC

We next examine the reach of HL-LHC ($\sqrt{s} = 14$ TeV with 3000 fb^{-1}) for the alternative model line constructed in the previous chapter to optimize free parameter space. First, we consider wino pair production in the nAMSB model. To proceed, we generate a SUSY Les Houches Accord (SLHA) file[103] for each of our nAMSB SUSY model line points using Isajet 7.91[20] and feed this into Madgraph[121]/Pythia8[122] which is used for both signal and background (BG)

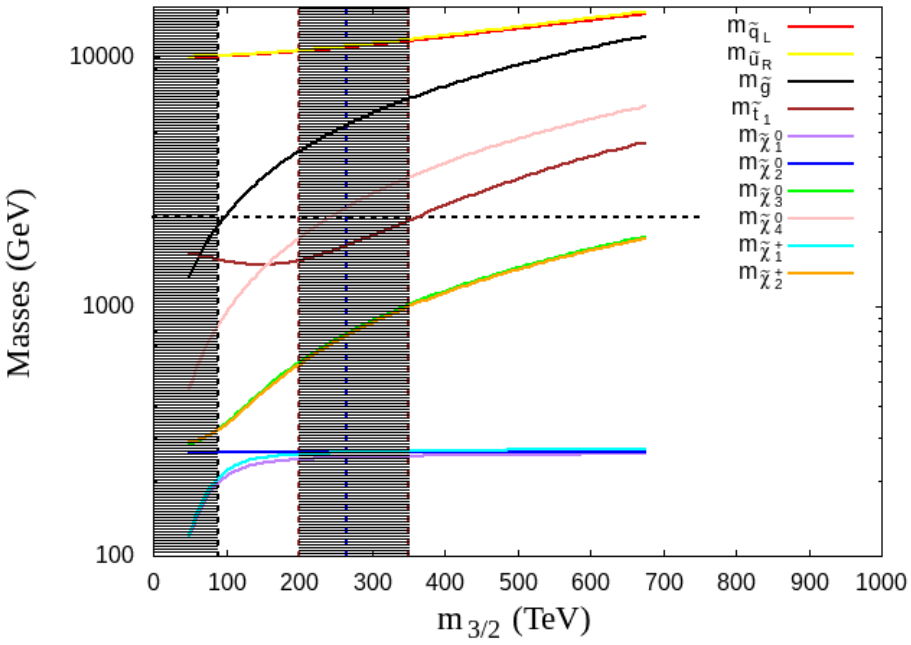


Figure 4.7: Allowed/excluded regions of our nAMSB model-line along with various sparticle masses. The vertical dashed line represents the upper limit on $m_{3/2}$ imposed by $\Delta_{EW} = 30$ and the horizontal dashed line represents the lower limit of the gluino mass.

processes. The $pp \to \tilde{\chi}_2^\pm \tilde{\chi}_3^0 X$ cross section is normalized to the Prospino NLO[102]. For the $2 \to 3$ BG processes, we also use Madgraph[121] coupled to Pythia. We adopt the toy detector simulation Delphes[123] using the default ATLAS card.

In Delphes, we identify the following entities.

- Jets are reconstructed using the anti-k_T algorithm with $p_T(j) > 20$ GeV within a cone of $\Delta R = 0.4$. Such clusters are labelled as jets when $p_T(j) > 40$ GeV with pseudorapidity $|\eta(j)| < 3.0$.

- Leptons with $p_T > 10$ GeV are reconstructed in a cone of $\Delta R = 0.2$. The maximum hadronic energy allowed in the cone is 10% of the leptonic p_T. Thus, leptons are identified when $p_T(\ell) > 10$ GeV and $|\eta(\ell)| < 2.5$.

4.4.1 Same-sign dileptons from wino pair production

Here we examine wino pair production $pp \to \tilde{\chi}_2^\pm \tilde{\chi}_3^0 X$ along our nAMSB model line at LHC14 where the relevant decay modes are $\tilde{\chi}_2^\pm \to \tilde{\chi}_{1,2}^0 W^\pm$ and $\tilde{\chi}_3^0 \to \tilde{\chi}_1^\pm W^\mp$. In this configuration, we expect a final state containing same-sign dibosons $W^\pm W^\pm + \not{E}_T$ about 50% of the time leading to a (relatively) jet-free same-sign dilepton $+\not{E}_T$ signature for which SM backgrounds are typically quite low. The production cross-section for this channel at $\sqrt{s} = 14$ TeV LHC for two values of $\mu = 150, 250$ GeV are shown in Fig. 4.8. This signal channel- proposed in Ref. [124] and expanded upon in Ref. [125]– is endemic to SUSY models with light higgsinos although so far there are no dedicated experimental analyses. Here, we will adopt the signal cuts of Ref. [125]: The original cuts from Ref. [124] are

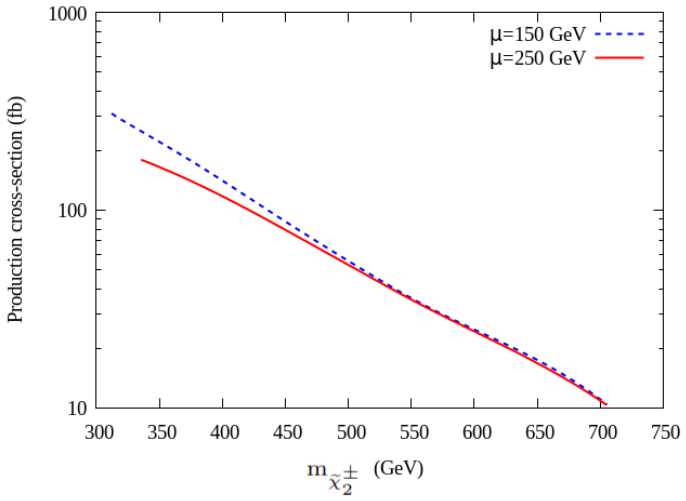


Figure 4.8: The production cross section from wino pair production $\widetilde{\chi}_2^{\pm}\widetilde{\chi}_3^0$ along the nAMSB model line with $\mu = 150$ and 250 GeV.

labelled as cut set **C1** which require:

- the presence of exactly two isolated same-sign leptons with $p_T(\ell_1) > 20$ GeV and $p_T(\ell_2) > 10$ GeV, where ℓ_1 (ℓ_2) is the higher (lower) p_T lepton,
- veto events with identified b-jets,
- $\not{E}_T > 200$ GeV and
- $min(m_T(\ell_1,\not{E}_T), m_T(\ell_2,\not{E}_T)) > 175$ GeV.

After inspecting distributions for signal/background events, Ref. [125] augmented these with **C2** cuts:

- $n(jets) \leq 1$ and
- $\not{E}_T > 250$ GeV.

SM Bkg	Cross-section (after cuts) (ab)
$t\bar{t}$	0.0
$t\bar{t}t\bar{t}$	0.0125
$t\bar{t}W$	0.52
$t\bar{t}Z$	0.88
$WWjj$	2.21
WWW	2.21
WWZ	1.358
WZZ	1.426
ZZ	0.0
WZ	0.0
Total SM background	8.62

Table 4.1: The SM background cross-sections after cut **C2** for the same-sign dilepton $+\not{E}_T$ signal at $\sqrt{s} = 14$ TeV.

The backgrounds coming from $t\bar{t}$, WZ, $t\bar{t}W$, $t\bar{t}Z$, $t\bar{t}t\bar{t}$, WWW, $WWjj$ WWZ, WZZ and ZZ were computed and tabulated in Table II of Ref. [125]. The total background after cuts **C1** and **C2** (with all BG total cross sections scaled to their NLO results) was ~ 8.62 ab with the largest coming from WWW and $WWjj$ production at 2.21 ab as seen in Table 4.1.

The signal cross section after cuts **C2** is shown vs. $m_{\tilde{\chi}_2^+}$ along the nAMSB model line, for *a*) $\mu = 150$ and *b*) 250 GeV in Fig. 4.9. In Fig. 4.9*a*), we denote the total SM background by the solid red horizontal line at 8.6 ab while the HL-LHC 3000 fb^{-1} 5σ line is horizontal red-dotted as is the 95%CL line. The left-most vertical line denotes the parameter space limit from LHC gluino pair searches where $m_{\tilde{g}} > 2.2$ TeV is required. The red-dotted vertical line at $m_{\tilde{\chi}_2^\pm} = 500,\ 600$ GeV denotes the upper limit on p-space from the ATLAS boosted hadronic jet search from wino pair production[101]. Beyond the right-most vertical red-dotted line is where the naturalness measure Δ_{EW} exceeds 30. From frame *a*), we see that for $\mu = 150$ GeV almost the entire presently-allowed p-space gap should be accessible to HL-LHC via the SSdB signal channel, well above the 5σ discovery

limit (the exception being a tiny slice with low $m_{3/2}$ where decay products are rather soft and don't exceed our rather hard cuts; this small slice may be filled by updated gluino pair search results).

In Fig. 4.9b), we plot the SSdB signal rates for the same model line parameters except that $\mu = 250$ GeV. In the $\mu = 250$ GeV case, we see that the bulk of presently-allowed p-space can be seen by HL-LHC at the 5σ level, except for the region with $m_{\tilde{\chi}_2^\pm} \lesssim 360$ GeV. For this lower range of wino mass values, the wino decays into real Ws are still open, but the wino decay products are much softer, and a softer $\not{E}_T$ cut may be necessary to pick out the lower mass wino pair events. In any case, the signal is only slightly below our projected 5σ level, and well above the 95%CL exclusion level [136].

4.4.2 Hard isolated trileptons from wino pair production

In this Subsection, we focus on wino pair production $pp \to \tilde{\chi}_2^\pm \tilde{\chi}_3^0$ followed by decays $\tilde{\chi}_2^\pm \to W^\pm \tilde{\chi}_{1,2}^0$ and $\tilde{\chi}_3^0 \to Z^0 \tilde{\chi}_{1,2}^0$. When both W and Z decay leptonically, then we expect the clean trilepton $+\not{E}_T$ final state topology[126, 127].

We evaluate the signal and SM background using Madgraph/Pythia/Delphes as before. After examining signal and background distributions, we the implement the following cuts

- The final state contains three identified isolated leptons with $p_T(\ell_1) > 20$ GeV, $p_T(\ell_2) > 15$ GeV and $p_T(\ell_3) > 10$ GeV, where ℓ_1 is the highest p_T lepton, and so forth.

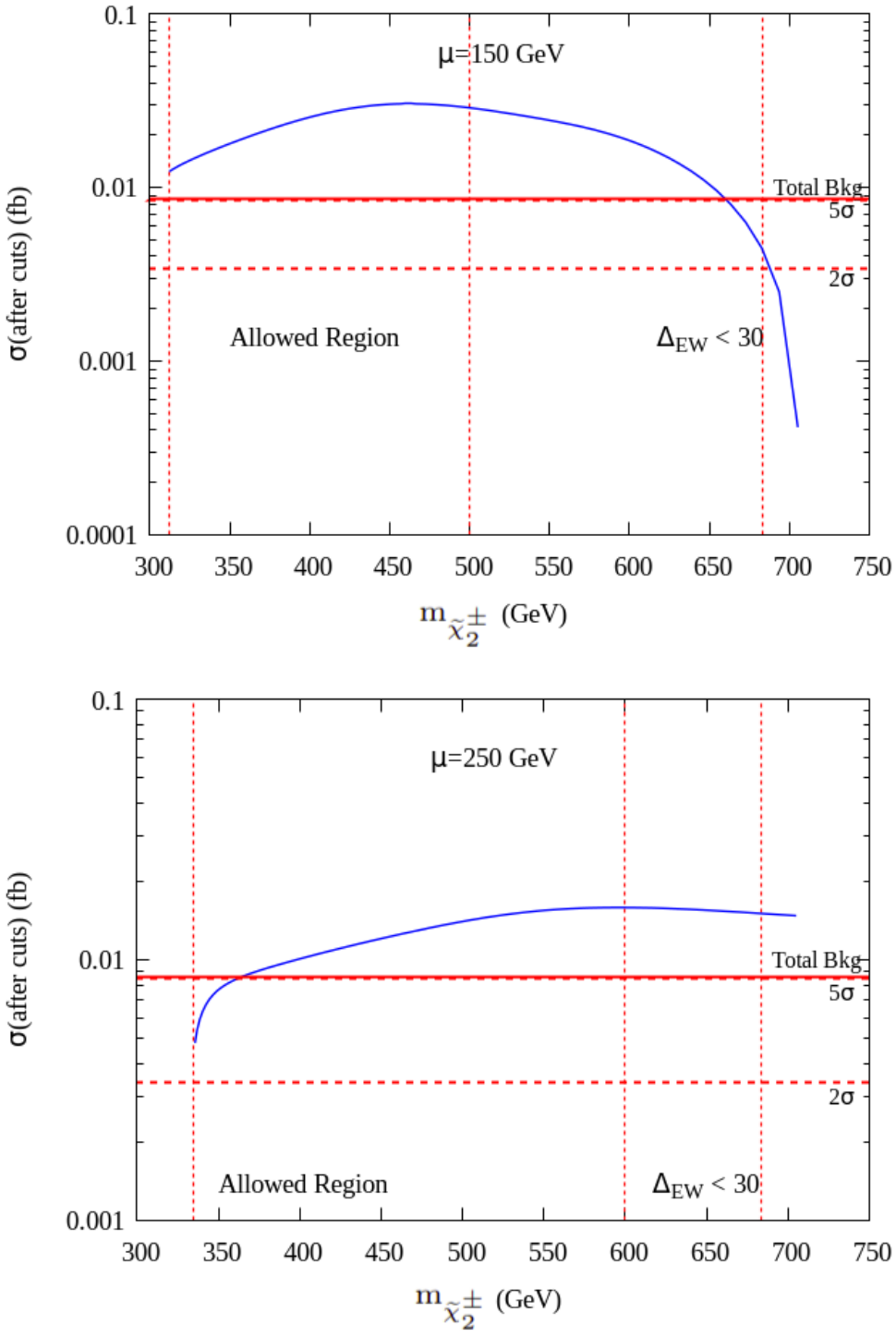


Figure 4.9: Cross section after cuts for the SSdB signature from wino pair production along the nAMSB model line for *a*) $\mu = 150$ GeV and *b*) $\mu = 250$ GeV. We also show the remaining total background rate.

- b-jet veto: $n_{b-jet} = 0$ and γ veto: $n_\gamma = 0$.
- $\not{E}_T > 100$ GeV.
- Effective mass $m_{eff} > 200$ GeV (where m_{eff} is the scalar sum of the p_Ts of the three leptons plus the $\not{E}_T$).
- Transverse mass $m_T(\ell_i, \not{E}_T) > 120$ GeV for each isolated lepton $i = 1 - 3$.
- Jet veto: $n_j = 0$.

The various SM cross sections (normalized to their NLO values, and where available, up to NNLO+NNLL) after these cuts are listed in Table 4.4.2. The dominant backgrounds are summarized as below:

- $t\bar{t}$ - NNLO + NNLL [128]
- WZ, ZZ, - NLO [132]
- $t\bar{t}Z, t\bar{t}W$- NLO (QCD + EW)[129]
- WWZ, WWW, ZZZ - NLO [133]
- tZj - NLO QCD+EW [131]
- tW - NNLO [130]

In Fig. 4.10*a*), we show a plot of the cross section after cuts along the nAMSB3 model line for $\mu = 150$ GeV as a function of $m_{\tilde{\chi}_2^\pm}$, along with the total remaining SM background. We also show the 5σ and $95\% CL$ reach of LHC14 for 3000 fb^{-1} of integrated luminosity. In this case, the wino pair production clean 3ℓ signal

SM background	Cross-section after cuts (ab)
$t\bar{t}$	2.92
WZ	0.712
ZZ	0.45
ttZ	2.25
ttW	0.32
WWZ	5.12
WWW	0.035
ZZZ	0.0047
tZj	0.158
tW	0
Total Background	11.97

Table 4.2: Cross section after cuts in ab for the dominant SM backgrounds to the hard 3ℓ signal at LHC14.

exceeds the 5σ level for $m_{\tilde{\chi}_2^\pm} \sim 300 - 620$ GeV, which is the entire allowed gap. A signal in this channel would provide strong confirmation of any signal already present in the SSdB channel.

In Fig. 4.10b), we show the hard 3ℓ signal along the nAMSB model line but with $\mu = 250$ GeV. In this case, the signal exceeds the 5σ level for the more limited range of $m_{\tilde{\chi}_2^\pm} \sim 450 - 600$ GeV. Thus, the lower portion of the gap is more difficult to access due to the softer wino decay products, since the wino decay to real W bosons is just barely open. Nonetheless, the signal exceeds the 95%CL range except for the very lowest values of $m_{\tilde{\chi}_2^\pm} \lesssim 350$ GeV [136].

4.4.3 Soft OS dileptons from higgsino pair production

Next we turn to nAMSB signals from higgsino pair production. The most lucrative reaction in this case comes from[134]

$$pp \to \tilde{\chi}_1^0 \tilde{\chi}_2^0 \quad \text{with} \quad \tilde{\chi}_2^0 \to \tilde{\chi}_1^0 \ell \bar{\ell}. \tag{4.2}$$

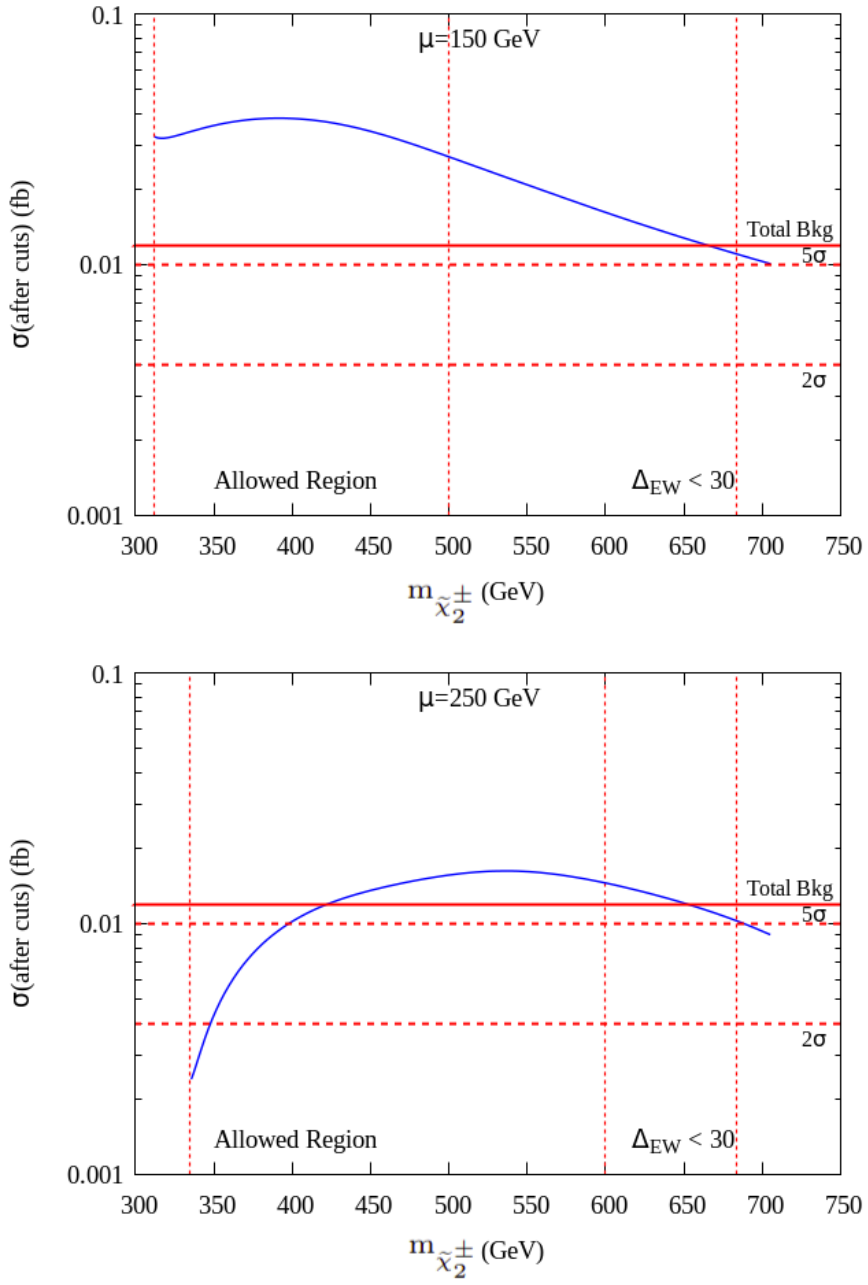


Figure 4.10: Cross section after cuts for the hard 3ℓ signature from wino pair production along the nAMSB model line with *a*) $\mu = 150$ GeV and *b*) $\mu = 250$ GeV. We also show the remaining total background rate. The central vertical dotted line corresponds to the LHC-allowed upper limit on p-space.

The visible decay products are very soft since the mass gap $m_{\tilde{\chi}_2^0} - m_{\tilde{\chi}_1^0}$ tends to be in the 5-50 GeV range, and most of the $\tilde{\chi}_2^0$ decay energy release goes into making the $\tilde{\chi}_1^0$ rest mass. The final state lepton energy can be boosted to higher values, and events can be triggered upon, by requiring a hard ISR jet emission[104, 105]. This is then the soft OS dilepton plus jet plus MET signature (OSDLJMET). Five selection cuts plus a ditau reconstruction cut requiring $m_{\tau\tau}^2 < 0$ to reject backgrounds such as Zj production (followed by $Z \to \tau\bar{\tau}$) were required in Ref. [105]. In Ref. [1], more efficient angular cuts were developed which reduce the ditau backgrounds to tiny levels. The original cut set **C1** augmented by new angular cuts to reject $Zj \to \tau\bar{\tau}j$ plus further cuts to reject $t\bar{t}$ and WW backgrounds were labelled set **C3** in Ref. [1, 135]. After cut-set **C3**, signal and SM BG were plotted against opposite-sign dilepton invariant mass $m(\ell\bar{\ell})$ where signal should accrue for $m(\ell\bar{\ell}) < m_{\tilde{\chi}_2^0} - m_{\tilde{\chi}_1^0}$ whilst for higher invariant masses data should be in accord with SM expectations.

In the present work, we evaluate signal along the nAMSB model lines for $\mu = 150$ GeV and 250 GeV using cuts **C3** along with the dilepton invariant mass edge cut and compare to SM backgrounds as evaluated in Ref's [1, 135]. Our results are shown in Fig. 4.11*a*) and *b*) for $\mu = 150$ and 250 GeV, respectively. From Fig. 4.11*a*) for $\mu = 150$ GeV, we see the blue signal curve lies well above the 5σ BG level for LHC14 with 3 ab^{-1} over the whole gap region. However, in frame *b*) for $\mu = 250$ GeV, the higgsino pair production signal is below the 5σ level for the entire allowed range of $m_{3/2}$ although it is above the 95%CL level for $m_{3/2} \sim 125 - 210$ TeV.

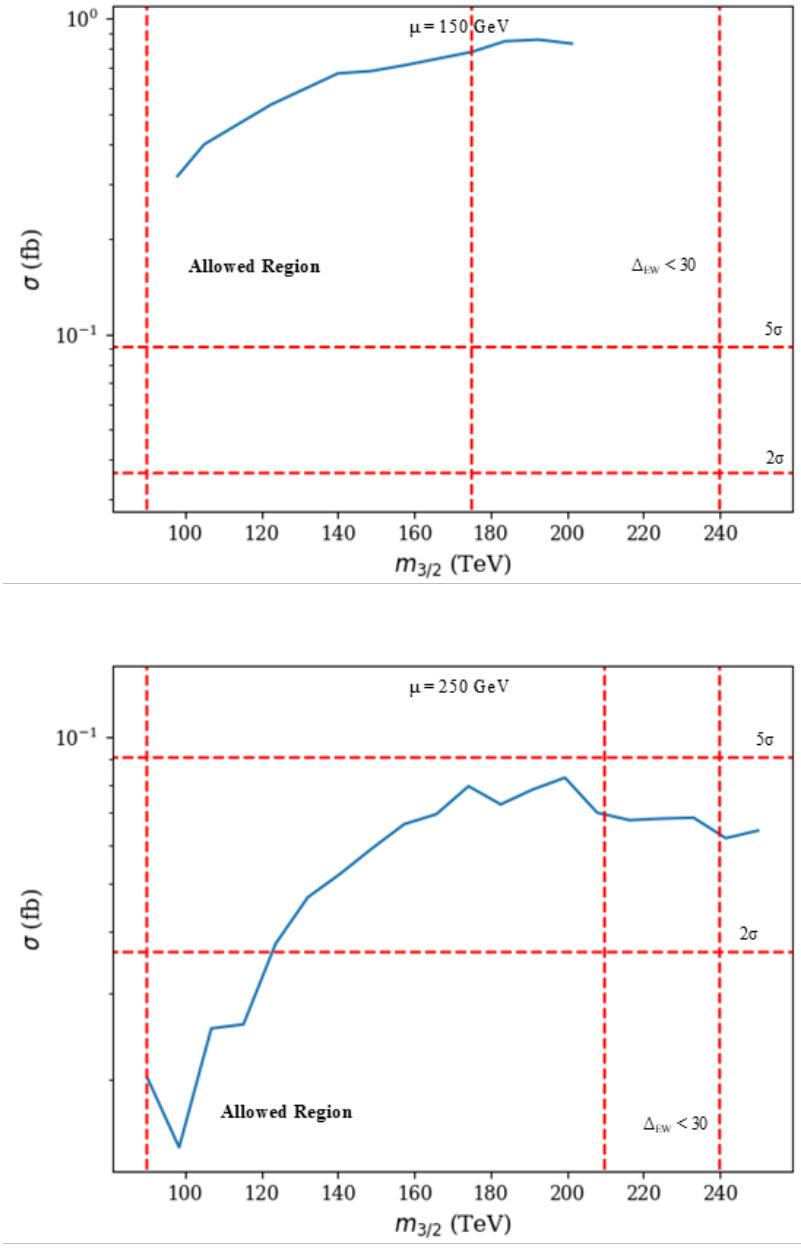


Figure 4.11: Cross section after cuts for the soft opposite-sign dilepton plus jet plus $\not{E}_T$ events from higgsino pair production along the nAMSB model line with *a*) $\mu = 150$ GeV and *b*) $\mu = 250$ GeV. We also show the 5σ and 95%CL lines for HL-LHC with 3 ab^{-1} of integrated luminosity.

In Fig. 4.12 we show in frame *a*) the cross section for the OSDJMET signal after cuts **C3** of Ref. [1] and with $m(\ell\bar{\ell}) < m_{\tilde{\chi}_2^0} - m_{\tilde{\chi}_1^0}$. As μ increases, while M_2 is fixed in this plot, the light higgsinos become increasingly mixed and the mass gap $m_{\tilde{\chi}_2^0} - m_{\tilde{\chi}_1^0}$ also increases so that the BG increases as well. But for 3 ab^{-1} of integrated luminosity, the number of signal events remain above 30 even for the maximal value of $\mu \sim 350$ GeV. In frame *b*), we show the n-σ level for the OSDJMET signal after cuts for LHC14 with 3 ab^{-1} of integrated luminosity. Here we show that the OSDJMET signal is above the 5σ discovery level out to $\mu \sim 225$ GeV and it lies above the 95%CL exclusion level for $\mu \lesssim 280$ GeV. For higher μ values, a signal in the OSDJMET channel would be difficult to ascertain [136].

4.4.4 Top-squark pair production

For light top-squarks, along the nAMSB model lines we have the $\tilde{t}_1 \to t\tilde{\chi}_{1,2}^0$ and $b\tilde{\chi}_1^+$ decay modes open, as is usual in natural models with gaugino mass unification, such as NUHM3. The difference between nAMSB and NUHM3 is that for nAMSB, the decay modes $\tilde{t}_1 \to b\tilde{\chi}_2^+$ and $\tilde{t}_1 \to t\tilde{\chi}_3^0$ may also be open at the 5-10% level, leading to some differences from expectations for NUHM3. The reach of HL-LHC for light top squarks $pp \to \tilde{t}_1\tilde{t}_1^* X$ was computed in Ref. [95] and the 5σ reach was found to extend to $m_{\tilde{t}_1} \lesssim 1.7$ TeV and the 95%CL reach to $m_{\tilde{t}_1} \lesssim 2$ TeV. We do not expect the results for the reach along the nAMSB model line to differ much from the NUHM3 model projections [136].

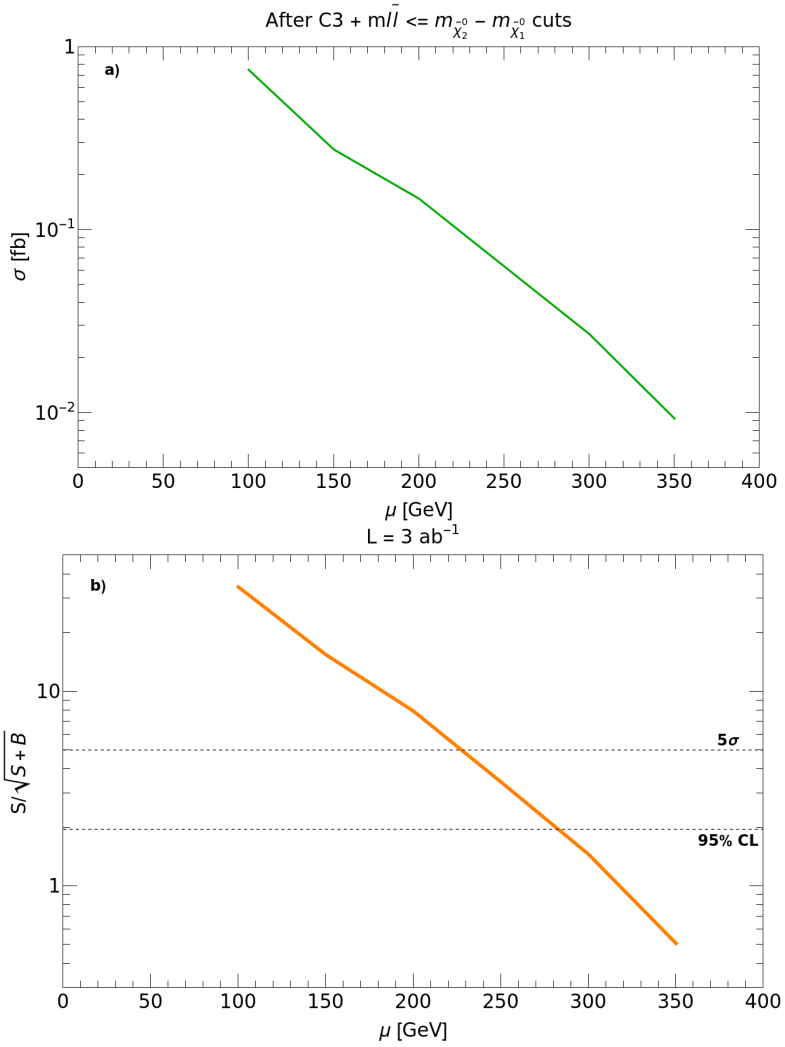


Figure 4.12: Cross section after cuts for the soft opposite-sign dilepton plus jet plus $\not{E}_T$ events from higgsino pair production along the nAMSB model line vs. μ but with with $m_{3/2} = 150$ TeV, $m_0(3) = m_{3/2}/35$, $m_0(1,2) = 2m_0(3)$, $A_0 = 1.2m_0(3)$, $m_A = 2$ TeV and $\tan\beta = 10$. In *a*), we show remaining signal cross section after cuts **C3** of Ref. [1] but with $m(\ell\bar{\ell}) < m_{\tilde{\chi}_2^0} - m_{\tilde{\chi}_1^0}$, and in frame *b*), we show the n-σ value after cuts at LHC14 with 3 ab^{-1} of integrated luminosity.

Chapter 5

Conclusions

We now conclude this dissertation and review the information we have discussed thus far. The minimal supersymmetric model was formulated primarily to counter the big hierarchy problem by assigning each particle a superpartner to cancel large divergences during renormalization, but it also provides an elegant way to merge general relativity and quantum field theory as well as offering up potential dark matter candidates. Extending SUSY to supergravity theories leads to the theory becoming nonrenormalizable, but this is merely an indication that SUGRA is a low energy effective field theory for a greater theory. Furthermore, we know that SUSY and SUGRA must be broken theories, similar to electroweak symmetry breaking, but we do not know exactly how it is broken. This has lead to many different theories to be proposed, and thus arose a need to analyze and compare the different theories and their likelihoods.

The first method to test various SUSY models is a measure of how fine tuned the model is, since if a given model is too finely tuned it is unnatural. There are several different fine tuning measures, but many are model dependent and tend to overestimate finetuning. Practical naturalness, which depends only on independent parameters, is measured by Δ_{EW} and thus is the chosen fine tuning measure for this paper.

Experimental data is another important factor in studying any model of physics, including SUSY. With the discovery of the Higgs boson, its mass m_h is a

well measured quantity which, in tandem with Δ_{EW} and additional experimental data, can inform us about whether or not various models are viable. Models with small A_i terms struggle to reach a large enough m_h without adding unnatural contributions from the top squarks (GMSB) or by an unnaturally large gaugino mass $m_{1/2}$ (inoMSB). Models with larger A_i, such as supergravity models (where large trilinear soft terms are the expected norm) as embodied by the NUHMi models, fare much better. As an example, NUHM2 has a large region of its parameter space that both satisfies criteria set forth by experimental data and remains natural by Δ_{EW}. AMSB models have mixed results. These models are a subset of gravity mediated SUSY breaking where the loop suppressed soft terms are able to become dominant as a result of the tree-level contributions being suppressed by sequestering. Minimal AMSB lacks a large A_0 and henceforth its available parameter space is entirely unnatural; however, it is not the only AMSB model. Natural AMSB does away with the universality of mAMSB and separates its scalar bulk masses. It also allows for the possibility of a larger A_0.

At this point, we turned to the string landscape to further inform us about nAMSB. General arguments suggest a power law draw to soft terms on the landscape which is tempered by the anthropic requirements of a weak scale rather close to one measured in our universe. Furthermore, prior studies had shown that models that are more natural are also far more probable in the string landscape. Knowing this, we scanned the landscape over different nAMSB parameters to find the most probable ranges. Firstly, $A_0 = 0$ once again yielded too low a higgs mass, whereas higher values lead to nAMSB having the largest probabilities centering

around $m_h \simeq 125$ GeV. Further scans showed larger probabilities for $m_0(3) = 5$ TeV, $m_A = 2$ TeV, and $A_0/m_0(3)$ in the range of 1 to 1.5.

The landscape scans informed further studies of nAMSB. The most probable ranges were used to create a target benchmark point that compared different AMSB models and showed that nAMSB models with larger A_0 are more natural. Extending the benchmark point to a model line reaffirmed this and showed that nAMSB has the most points within the correct m_h range as well as the most points below $\Delta_{EW} = 30$. Further extended analysis in parameter space showed a large gap not yet excluded by experimental data. This informed the range of values we studied in order to find the best detection channels at the HL-LHC.

Utilizing PROSPINO, cross sections for light stop pair production, gluino pair production, and different EWino pair production were generated over the second model line. The results showed that EWino production had the largest total contribution, with wino pair production from $pp \to \tilde{\chi}_2^+\tilde{\chi}_2^-, \tilde{\chi}_3^0\tilde{\chi}_2^\pm$ and higgsino pair production from $pp \to \tilde{\chi}_1^0\tilde{\chi}_2^0, \tilde{\chi}_2^0\tilde{\chi}_1^\pm$. Analyzing the branching ratios provided by SLHA files for the model line showed that the most likely decays for the positively charged wino $\tilde{\chi}_2^+$ are $\tilde{\chi}_1^0 W^+$, $\tilde{\chi}_2^0 W+$, $\tilde{\chi}_1^+ Z$, and $\tilde{\chi}_1^+ h$ with analogous decays for the negatively charged wino. Meanwhile for the neutral wino $\tilde{\chi}_3^0$ are $\tilde{\chi}_1^\mp W^\pm$, $\tilde{\chi}_2^0 Z$, and $\tilde{\chi}_1^0 h$. These results lead to the most likely discovery channels at the HL-LHC being $VV + MET$, $Vh + MET$, and $hh + MET$. For the higgsino production, $\tilde{\chi}_2^0$ will most likely decay to $f\overline{f}\tilde{\chi}_1^0$ with the leptonic channel $\ell\overline{\ell}\tilde{\chi}_1^0$ leading to a soft OSDLJMET discovery channel. Finally, the light stop $\tilde{t}_1$ is most likely to decay to $b\tilde{\chi}_2^+$ at lower $m_{3/2}$ and to $b\tilde{\chi}_1^+$ at larger $m_{3/2}$.

After determining the possible discovery channels at the HL-LHC, we then simulated both the signal and background by using SLHA files generated by Isajet as input parameters for Madgraph, whose results were fed into Pythia8 for hadronization and subsequently Delphes with the default ATLAS card for detector simulation. Different cuts were then applied to the data using Root. For the wino pair production channels, the same sign diboson signal has almost all of p-space at or above 5σ. The hard trilepton signal also has a high amount of p-space above 5σ, but it decreases as μ increases. The soft OSDLJMET signal is similar; at $\mu = 150$ GeV, the entire model line is above 5σ, but at $\mu = 250$ GeV, the model line is below 5σ but still above a 95% confidence level. However, further exploration shows that the model line is above 5σ up until $\mu = 225$ GeV. Finally, the light stop pair production signal is expected to have similar results to NUHM3. Thus, there are still multiple avenues open for the discovery of supersymmetry. The possibilities presented here are just an example of different tracks that may be explored in the pursuit of a complete physics theory.

To summarize, we were able to show that, compared to older models, nAMSB is more natural and has an open region in parameter space that falls within the boundaries laid out by previous experimental data. Furthermore, with the use of simulation software, we were able to deduce the best channels for detections at the LHC and show that the majority of these signals are 5σ away from the background. Because the LHC has collected approximately 320 fb^{-1} of integrated luminosity thus far and anticipates 3000 fb $^{-1}$ from the HL-LHC, one can compute the expected event rate by multiplying the respective integrated luminosity values

by the cross sections shown in the signal graphs. This means that with the upcoming experimental data, we will be able to determine the validity of the nAMSB model.

References

[1] H. Baer, V. Barger, D. Sengupta, and X. Tata, Phys. Rev. D **105**, 095017 (2022).

[2] M. E. Peskin and D. V. Schroeder, *An Introduction to quantum field theory* (Addison-Wesley, Reading, USA, 1995).

[3] G. Aad *et al.*, Phys. Lett. B **716**, 1 (2012).

[4] S. Chatrchyan *et al.*, Phys. Lett. B **716**, 30 (2012).

[5] Y. Fukuda *et al.*, Phys. Rev. Lett. **81**, 1562 (1998).

[6] H. Baer and X. Tata, *Weak scale supersymmetry: From superfields to scattering events* (Cambridge University Press, ADDRESS, 2006).

[7] A. Brignole, L. E. Ibanez, and C. Munoz, Adv. Ser. Direct. High Energy Phys. **21**, 244 (2010).

[8] H. Baer, A. Mustafayev, S. Profumo, A. Belyaev, and X. Tata, JHEP **07**, 065 (2005).

[9] V. Kaplunovsky and J. Louis, Nucl. Phys. B **422**, 57 (1994).

[10] L. Randall and R. Sundrum, Nucl. Phys. B **557**, 79 (1999).

[11] M. Kawasaki, K. Kohri, T. Moroi, and A. Yotsuyanagi, Phys. Rev. D **78**, 065011 (2008).

[12] J. Pradler and F. D. Steffen, Phys. Rev. D **75**, 023509 (2007).

[13] T. Moroi and L. Randall, Nucl. Phys. B **570**, 455 (2000).

[14] K. J. Bae, H. Baer, V. Barger, and R. W. Deal, JHEP **02**, 138 (2022).

[15] H. Baer, V. Barger, J. Bolich, J. Dutta, and D. Sengupta, Phys. Rev. D **109**, 035011 (2024).

[16] M. Dine, A. E. Nelson, Y. Nir, and Y. Shirman, Phys. Rev. D **53**, 2658 (1996).

[17] D. E. Kaplan, G. D. Kribs, and M. Schmaltz, Phys. Rev. D **62**, 035010 (2000).

[18] Z. Chacko, M. A. Luty, A. E. Nelson, and E. Ponton, JHEP **01**, 003 (2000).

[19] M. Schmaltz and W. Skiba, Phys. Rev. D **62**, 095005 (2000).

[20] F. E. Paige, S. D. Protopopescu, H. Baer, and X. Tata, (2003).

[21] H. Baer, C.-H. Chen, R. B. Munroe, F. E. Paige, and X. Tata, Phys. Rev. D **51**, 1046 (1995).

[22] S. Heinemeyer, W. Hollik, and G. Weiglein, Comput. Phys. Commun. **124**, 76 (2000).

[23] J. R. Ellis, K. A. Olive, and Y. Santoso, Phys. Lett. B **539**, 107 (2002).

[24] M. A. Bisset, Other thesis, 1995.

[25] D. M. Pierce, J. A. Bagger, K. T. Matchev, and R.-j. Zhang, Nucl. Phys. B **491**, 3 (1997).

[26] M. Carena and H. E. Haber, Prog. Part. Nucl. Phys. **50**, 63 (2003).

[27] H. Baer, V. Barger, and M. Savoy, Phys. Rev. D **93**, 035016 (2016).

[28] H. Baer, V. Barger, D. Martinez, and S. Salam, Phys. Rev. D **108**, 035050 (2023).

[29] H. Baer, V. Barger, P. Huang, A. Mustafayev, and X. Tata, Phys. Rev. Lett. **109**, 161802 (2012).

[30] H. Baer, V. Barger, S. Salam, D. Sengupta, and K. Sinha, Eur. Phys. J. ST **229**, 3085 (2020).

[31] K. J. Bae, H. Baer, and E. J. Chun, Phys. Rev. D **89**, 031701 (2014).

[32] K. J. Bae, H. Baer, and E. J. Chun, JCAP **12**, 028 (2013).

[33] J. R. Ellis, K. Enqvist, D. V. Nanopoulos, and F. Zwirner, Mod. Phys. Lett. A **1**, 57 (1986).

[34] R. Barbieri and G. F. Giudice, Nucl. Phys. B **306**, 63 (1988).

[35] S. Dimopoulos and G. F. Giudice, Phys. Lett. B **357**, 573 (1995).

[36] H. Baer, V. Barger, and D. Mickelson, Phys. Rev. D **88**, 095013 (2013).

[37] H. Baer, V. Barger, and A. Mustafayev, Phys. Rev. D **85**, 075010 (2012).

[38] H. Baer, V. Barger, D. Mickelson, and M. Padeffke-Kirkland, Phys. Rev. D **89**, 115019 (2014).

[39] S. Chatrchyan *et al.*, Phys. Lett. B **710**, 26 (2012).

[40] S. K. Soni and H. A. Weldon, Phys. Lett. B **126**, 215 (1983).

[41] V. S. Kaplunovsky and J. Louis, Phys. Lett. B **306**, 269 (1993).

[42] A. Brignole, L. E. Ibanez, and C. Munoz, Nucl. Phys. B **422**, 125 (1994), [Erratum: Nucl.Phys.B 436, 747–748 (1995)].

[43] K. J. Bae, H. Baer, V. Barger, and D. Sengupta, Phys. Rev. D **99**, 115027 (2019).

[44] H. M. Lee, S. Raby, M. Ratz, G. G. Ross, R. Schieren, K. Schmidt-Hoberg, and P. K. S. Vaudrevange, Nucl. Phys. B **850**, 1 (2011).

[45] H. Baer, V. Barger, and D. Sengupta, Phys. Lett. B **790**, 58 (2019).

[46] P. N. Bhattiprolu and S. P. Martin, Phys. Rev. D **104**, 055014 (2021).

[47] J. E. Kim and H. P. Nilles, Phys. Lett. B **138**, 150 (1984).

[48] M. Dine, J. L. Feng, and E. Silverstein, Phys. Rev. D **74**, 095012 (2006).

[49] M. Bose and M. Dine, JHEP **03**, 057 (2013).

[50] J. Polonyi, Generalization of the Massive Scalar Multiplet Coupling to the Supergravity, 1977.

[51] H. Baer, V. Barger, and K. Zhang, (2024).

[52] H. Baer, V. Barger, and D. Sengupta, Phys. Rev. Res. **1**, 033179 (2019).

[53] M. R. Douglas, Statistical analysis of the supersymmetry breaking scale, 2004.

[54] L. Susskind, in *From Fields to Strings: Circumnavigating Theoretical Physics: A Conference in Tribute to Ian Kogan* (PUBLISHER, ADDRESS, 2004), pp. 1745–1749.

[55] N. Arkani-Hamed, S. Dimopoulos, and S. Kachru, Predictive Landscapes and New Physics at a TeV, 2005.

[56] V. Agrawal, S. M. Barr, J. F. Donoghue, and D. Seckel, Phys. Rev. D **57**, 5480 (1998).

[57] M. R. Douglas, Comptes Rendus Physique **5**, 965 (2004).

[58] H. Baer, V. Barger, and S. Salam, Phys. Rev. Research. **1**, 023001 (2019).

[59] E. Witten, Nucl. Phys. B **188**, 513 (1981).

[60] S. Ferrara, L. Girardello, and H. P. Nilles, Phys. Lett. B **125**, 457 (1983).

[61] I. Affleck, M. Dine, and N. Seiberg, Nucl. Phys. B **256**, 557 (1985).

[62] G. F. Giudice, M. A. Luty, H. Murayama, and R. Rattazzi, JHEP **12**, 027 (1998).

[63] J. D. Wells, Phys. Rev. D **71**, 015013 (2005).

[64] A. Arvanitaki, N. Craig, S. Dimopoulos, and G. Villadoro, JHEP **02**, 126 (2013).

[65] J. D. Wells, in *11th International Conference on Supersymmetry and the Unification of Fundamental Interactions* (PUBLISHER, ADDRESS, 2003).

[66] N. Arkani-Hamed and S. Dimopoulos, JHEP **06**, 073 (2005).

[67] G. F. Giudice and A. Romanino, Nucl. Phys. B **699**, 65 (2004), [Erratum: Nucl.Phys.B 706, 487–487 (2005)].

[68] N. Arkani-Hamed, S. Dimopoulos, G. F. Giudice, and A. Romanino, Nucl. Phys. B **709**, 3 (2005).

[69] G. F. Giudice and A. Strumia, Nucl. Phys. B **858**, 63 (2012).

[70] H. Baer, V. Barger, and D. Sengupta, Phys. Rev. D **98**, 015039 (2018).

[71] P. Slavich *et al.*, Eur. Phys. J. C **81**, 450 (2021).

[72] H. Baer, A. Lessa, S. Rajagopalan, and W. Sreethawong, JCAP **06**, 031 (2011).

[73] H. Baer, V. Barger, and H. Serce, Phys. Rev. D **94**, 115019 (2016).

[74] R. Bousso and J. Polchinski, JHEP **06**, 006 (2000).

[75] L. Susskind, 247 (2003).

[76] M. R. Douglas and S. Kachru, Rev. Mod. Phys. **79**, 733 (2007).

[77] M. R. Douglas, JHEP **05**, 046 (2003).

[78] S. Ashok and M. R. Douglas, JHEP **01**, 060 (2004).

[79] W. Taylor and Y.-N. Wang, JHEP **12**, 164 (2015).

[80] S. Weinberg, Phys. Rev. Lett. **59**, 2607 (1987).

[81] M. Dine, R. G. Leigh, and A. Kagan, Phys. Rev. D **48**, 4269 (1993).

[82] E. Bagnaschi, G. F. Giudice, P. Slavich, and A. Strumia, JHEP **09**, 092 (2014).

[83] N. Arkani-Hamed, A. Gupta, D. E. Kaplan, N. Weiner, and T. Zorawski, (2012).

[84] H. Baer, V. Barger, D. Martinez, and S. Salam, JHEP **03**, 186 (2022).

[85] H. Baer, V. Barger, D. Martinez, and S. Salam, JHEP **09**, 125 (2022).

[86] G. L. Kane, C. F. Kolda, L. Roszkowski, and J. D. Wells, Phys. Rev. D **49**, 6173 (1994).

[87] L. J. Hall and Y. Nomura, JHEP **01**, 082 (2012).

[88] V. Barger, J. Jiang, P. Langacker, and T. Li, Nucl. Phys. B **726**, 149 (2005).

[89] B. S. Acharya, K. Bobkov, G. L. Kane, J. Shao, and P. Kumar, Phys. Rev. D **78**, 065038 (2008).

[90] H. Baer, V. Barger, H. Serce, and K. Sinha, JHEP **03**, 002 (2018).

[91] H. Baer, V. Barger, and D. Sengupta, Phys. Rev. Res. **2**, 013346 (2020).

[92] H. Baer, V. Barger, X. Tata, and K. Zhang, Symmetry **14**, 2061 (2022).

[93] H. Baer, V. Barger, M. Savoy, and H. Serce, Phys. Lett. B **758**, 113 (2016).

[94] H. Baer, V. Barger, J. S. Gainer, P. Huang, M. Savoy, D. Sengupta, and X. Tata, Eur. Phys. J. C **77**, 499 (2017).

[95] H. Baer, V. Barger, J. Dutta, D. Sengupta, and K. Zhang, (2023).

[96] T. Gherghetta, G. F. Giudice, and J. D. Wells, Nucl. Phys. B **559**, 27 (1999).

[97] J. L. Feng and T. Moroi, Phys. Rev. D **61**, 095004 (2000).

[98] K. J. Bae, H. Baer, A. Lessa, and H. Serce, Front. in Phys. **3**, 49 (2015).

[99] A. Canepa, Rev. Phys. **4**, 100033 (2019).

[100] G. Aad *et al.*, Phys. Rept. **1116**, 261 (2025).

[101] G. Aad *et al.*, Phys. Rev. D **104**, 112010 (2021).

[102] W. Beenakker, R. Hopker, and M. Spira, PROSPINO: A Program for the production of supersymmetric particles in next-to-leading order QCD, 1996.

[103] P. Z. Skands *et al.*, JHEP **07**, 036 (2004).

[104] Z. Han, G. D. Kribs, A. Martin, and A. Menon, Phys. Rev. D **89**, 075007 (2014).

[105] H. Baer, A. Mustafayev, and X. Tata, Phys. Rev. D **90**, 115007 (2014).

[106] H. Baer, V. Barger, N. Nagata, and M. Savoy, Phys. Rev. D **95**, 055012 (2017), [Addendum: Phys.Rev.D 103, 059902 (2021)].

[107] G. Aad *et al.*, Eur. Phys. J. C **83**, 561 (2023).

[108] T. C. Collaboration *et al.*, JHEP **10**, 244 (2019).

[109] A. M. Sirunyan *et al.*, Eur. Phys. J. C **80**, 3 (2020).

[110] A. Tumasyan *et al.*, Phys. Lett. B **842**, 137460 (2023).

[111] S. Kraml, S. Kulkarni, U. Laa, A. Lessa, W. Magerl, D. Proschofsky-Spindler, and W. Waltenberger, Eur. Phys. J. C **74**, 2868 (2014).

[112] F. Ambrogi *et al.*, Comput. Phys. Commun. **251**, 106848 (2020).

[113] G. Alguero, J. Heisig, C. K. Khosa, S. Kraml, S. Kulkarni, A. Lessa, H. Reyes-González, W. Waltenberger, and A. Wongel, JHEP **08**, 068 (2022).

[114] M. Drees, H. Dreiner, D. Schmeier, J. Tattersall, and J. S. Kim, Comput. Phys. Commun. **187**, 227 (2015).

[115] D. Dercks, N. Desai, J. S. Kim, K. Rolbiecki, J. Tattersall, and T. Weber, Comput. Phys. Commun. **221**, 383 (2017).

[116] A. M. Sirunyan *et al.*, JHEP **03**, 166 (2018).

[117] Search for squarks and gluinos in final states with jets and missing transverse momentum using 139 fb^{-1} of $\sqrt{s}$ =13 TeV pp collision data with the ATLAS detector, 2019.

[118] G. Aad *et al.*, Eur. Phys. J. C **81**, 1118 (2021).

[119] A. Tumasyan *et al.*, JHEP **04**, 091 (2022).

[120] M. Aaboud *et al.*, Phys. Rev. D **97**, 112001 (2018).

[121] J. Alwall, M. Herquet, F. Maltoni, O. Mattelaer, and T. Stelzer, JHEP **06**, 128 (2011).

[122] T. Sjostrand, S. Mrenna, and P. Z. Skands, JHEP **05**, 026 (2006).

[123] J. de Favereau, C. Delaere, P. Demin, A. Giammanco, V. Lemaître, A. Mertens, and M. Selvaggi, JHEP **02**, 057 (2014).

[124] H. Baer, V. Barger, P. Huang, D. Mickelson, A. Mustafayev, W. Sreethawong, and X. Tata, Phys. Rev. Lett. **110**, 151801 (2013).

[125] H. Baer, V. Barger, J. S. Gainer, M. Savoy, D. Sengupta, and X. Tata, Phys. Rev. D **97**, 035012 (2018).

[126] H. Baer and X. Tata, Phys. Lett. B **155**, 278 (1985).

[127] H. Baer, C.-h. Chen, F. Paige, and X. Tata, Phys. Rev. D **50**, 4508 (1994).

[128] M. Czakon and A. Mitov, Comput. Phys. Commun. **185**, 2930 (2014).

[129] D. de Florian *et al.*, **2/2017**, (2016).

[130] N. Kidonakis, PoS **DIS2015**, 170 (2015).

[131] D. Pagani, I. Tsinikos, and E. Vryonidou, JHEP **08**, 082 (2020).

[132] J. M. Campbell, R. K. Ellis, and C. Williams, JHEP **07**, 018 (2011).

[133] J. Alwall, R. Frederix, S. Frixione, V. Hirschi, F. Maltoni, O. Mattelaer, H. S. Shao, T. Stelzer, P. Torrielli, and M. Zaro, JHEP **07**, 079 (2014).

[134] H. Baer, V. Barger, and P. Huang, JHEP **11**, 031 (2011).

[135] H. Baer, V. Barger, D. Sengupta, and X. Tata, in *Snowmass 2021* (PUBLISHER, ADDRESS, 2022).

[136] H. Baer, V. Barger, J. Bolich, J. Dutta, and D. Sengupta, Phys. Rev. D **111**, 015002 (2025).

[137] H. Baer, V. Barger, J. Bolich, and K. Zhang, Phys. Rev. D **111**, 095019 (2025).

[138] H. Baer, V. Barger, J. Bolich, J. Dutta, D. Martinez, S. Salam, D. Sengupta, and K. Zhang, Rev. Mod. Phys. **97**, 045001 (2025).